

2007

## Thermal switching to improve time-averaged efficiency of thermoelectric energy harvesting

Robin Gwen McCarty  
*University of Dayton*

Follow this and additional works at: [https://ecommons.udayton.edu/graduate\\_theses](https://ecommons.udayton.edu/graduate_theses)

---

### Recommended Citation

McCarty, Robin Gwen, "Thermal switching to improve time-averaged efficiency of thermoelectric energy harvesting" (2007). *Graduate Theses and Dissertations*. 4268.  
[https://ecommons.udayton.edu/graduate\\_theses/4268](https://ecommons.udayton.edu/graduate_theses/4268)

This Dissertation is brought to you for free and open access by the Theses and Dissertations at eCommons. It has been accepted for inclusion in Graduate Theses and Dissertations by an authorized administrator of eCommons. For more information, please contact [mschlange1@udayton.edu](mailto:mschlange1@udayton.edu), [ecommons@udayton.edu](mailto:ecommons@udayton.edu).

**Thermal Switching to Improve Time-Averaged  
Efficiency of Thermoelectric Energy Harvesting**

Dissertation

Submitted to

The School of Engineering of the  
**UNIVERSITY OF DAYTON**

in Partial Fulfillment of the Requirements for

The Degree

Doctorate of Philosophy in Mechanical Engineering

by

**Robin Gwen McCarty**

**UNIVERSITY OF DAYTON**

Dayton, Ohio

August, 2007

Thermal Switching to Improve Time-Averaged Efficiency of Thermoelectric Energy Harvesting

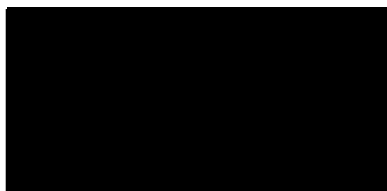
APPROVED BY:



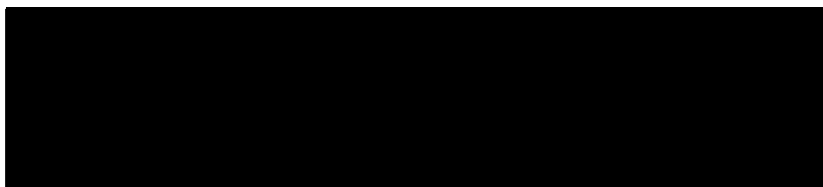
Kevin Hallinan, Ph.D.  
Advisory Committee Chairman  
Chair, Mechanical and Aerospace  
Engineering Department



Brian Sanders, Ph.D.  
Committee Member  
Adjunct Professor, Mechanical and  
Aerospace Engineering Department



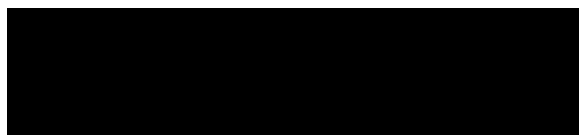
Khalid Lafdi, Ph.D.  
Committee Member  
University of Dayton Research Institute



Major Paul Kladitis, Ph.D.  
Committee Member  
Edwards Air Force Base



Malcolm W. Daniels, Ph.D.  
Associate Dean  
School of Engineering



Joseph E. Saliba, Ph.D., P.E.  
Dean, School of Engineering

## ABSTRACT

### Thermal Switching to Improve Time-Averaged Efficiency of Thermoelectric Energy Harvesting

Name: McCarty, Robin Gwen

University of Dayton, 2007

Advisor: Kevin P. Hallinan, Ph.D.

Recent improvements in thermoelectric (TE) materials have expanded the potential to use this technology for the generation of electricity from waste heat in a variety of applications. The performance of a TE generator improves when the temperature difference across the generator is maximized. A "thermal switch," located between the heat source and the TE device, is posed to modulate the heat flow through the TE device permitting heat to flow from the source to the TE device only when the source temperature is near maximum, yielding a higher time-averaged temperature drop across the TE, and therefore a higher efficiency.

A numerical model is used to evaluate the benefits of a thermal switch in series with a TE generator for both time-varying and constant heat inputs. The results demonstrate that modulating the heat flow through the TE device and maintaining the source temperature near a constant maximum value improves the time-averaged efficiency of the TE device. For ideal conditions, improved efficiencies of more than five times are realized, though for more realistic conditions, efficiencies are improved up to 35%.

Using an experimental set-up with a variable thermal resistance air gap serving as a thermal switch, the time-averaged power output to power input ratio improved up to 15% and 30% respectively for constant and variable heat input in certain design space conditions. The experimental results, as supported by model predictions, suggest that the thermal capacitance of the heat source must be greater than the thermal capacitance of the TE device in order for thermal switching to improve the time-averaged power output to power input ratios of waste heat recovery systems.

A micro heat pipe design for an integrated thermal switch is proposed based on a steady-state model of the energy harvesting system. After fabrication, the micro heat pipe is characterized for thermal resistance performance as a function of source temperature. After testing two fluids at various fill ratios, the micro heat pipe conceptually performs as a thermal switch for both constant and variable heat sources.

## **Acknowledgements**

I must first thank my husband and family for supporting this professional endeavor. Their love and encouragement made this possible.

Kevin Hallinan and Brian Sanders were instrumental in the success of this project and my personal development as a researcher over the past three year.

I'd also like to thank Jack Holliday, Dylan Monaghan, Doug Wolf, and Larry Sqrow for their technical advice on the experimental side of this project.

## Contents

### Chapter

<b>1</b>	<b>Introduction</b>	<b>1</b>
1.1	Motivation . . . . .	1
1.2	Thermal Management and Control . . . . .	1
1.3	Energy Harvesting and Waste Heat Recovery . . . . .	3
1.4	Thermal Switches in Surveillance Aircraft Applications . . . . .	4
<b>2</b>	<b>Background</b>	<b>10</b>
2.1	TE Device . . . . .	10
2.1.1	Thermoelectric Effect . . . . .	11
2.1.2	Transient Effects . . . . .	13
2.1.3	TE Device Materials . . . . .	16
2.2	Thermal Switch Designs . . . . .	18
2.3	Heat Pipes . . . . .	23
2.4	Background Summary . . . . .	23
<b>3</b>	<b>Conceptual Analysis of Energy Harvesting with Thermal Switching</b>	<b>25</b>
3.1	RC Equivalent Model . . . . .	25
3.2	Analytical Finite Difference Model . . . . .	34
3.2.1	Ideal Cases . . . . .	37

3.2.2	Realistic Cases . . . . .	49
3.3	Conceptual Analysis Conclusions . . . . .	50
4	Feasibility Experiment for Thermal Switch Augmentation of Energy Harvesting	51
4.1	Experimental Set-up and Procedure . . . . .	51
4.2	Experimental Results . . . . .	54
4.2.1	Constant Heat Input . . . . .	54
4.2.2	Variable Heat Input . . . . .	58
4.3	Capacitance Effects . . . . .	58
4.4	Comparison Between Analytical Model and Variable Air-Gap Experiment .	61
4.5	Projected Results for State of the Art TE Device . . . . .	63
5	Thermal Switch Designs Exploration	64
5.1	Horizontal Micro-Electrical-Mechanical System . . . . .	65
5.2	Vertical Micro-Electrical-Mechanical System . . . . .	70
5.3	Wax-Filled Wells . . . . .	75
5.4	Micro Heat Pipes . . . . .	80
5.5	Design Comparison . . . . .	87
6	Micro Heat Pipe Fabrication and Characterization	88
6.1	Fabrication . . . . .	88
6.2	Assembly . . . . .	89
6.3	Experimental Procedure . . . . .	94
6.3.1	Thermal Switch Resistance Measurement . . . . .	94
6.4	Results . . . . .	98
6.4.1	Baseline . . . . .	98
6.4.2	Thermal Switch Filled with Propanol . . . . .	99



6.4.3 Thermal Switch Filled with Decane . . . . .	104
<b>7 Conclusions and Recommendations</b>	<b>108</b>
7.1 Thermal Switching Enhancement of Energy Harvesting . . . . .	108
7.2 Recommendations . . . . .	109
 <b>Appendix</b>	
<b>A Publications</b>	<b>112</b>
A.1 Peer-Reviewed Journal Publications . . . . .	112
A.2 Peer-Reviewed Conference Publications . . . . .	112
<b>B Variable Air-Gap Experimental Results, Constant Heat Input</b>	<b>114</b>
<b>C Variable Air-Gap Experimental Results, Variable Heat Input</b>	<b>123</b>
 <b>Bibliography</b>	 <b>133</b>

## Figures

### Figure

1.1	Illustration of representative unmanned surveillance aircraft. . . . .	5
1.2	Schematic of energy harvesting system with TE device and thermal switch.	6
1.3	Illustration of representative energy harvesting system without a thermal switch. . . . .	7
1.4	Illustration of representative energy harvesting system with a thermal switch.	8
2.1	Schematic of TE device. . . . .	11
2.2	Schematic of a TE device p-n junction. . . . .	12
2.3	Energy diagram of a TE device p-n junction. . . . .	14
2.4	MEMS TE device and integrated thermal switch [71]. . . . .	18
2.5	Louver design for emissivity-based thermal switch [84]. . . . .	19
2.6	Shutter design for emissivity-based thermal switch [84]. . . . .	20
2.7	Schematic of emissivity-based thermal switch [86]. . . . .	21
2.8	Photograph of liquid-mercury micro-droplet thermal potentiometer [87]. . .	21
2.9	Schematic of traditional heat pipe. . . . .	22
3.1	RC Equivalent Model of Energy Harvesting System with a Thermal Switch .	26
3.2	Simplified RC Equivalent Model of Energy Harvesting System with a Thermal Switch . . . . .	30

3.3	Simplified RC Equivalent Model of Energy Harvesting System with a Thermal Switch for $t < 0$ . . . . .	31
3.4	Simplified RC Equivalent Model of Energy Harvesting System with a Thermal Switch for $t > 0$ . . . . .	32
3.5	Finite difference model schematic. . . . .	35
3.6	Finite difference model for one resistor and one capacitor. . . . .	36
3.7	Overall TE Generator Efficiency for Case 1 with and without source temperature control, $\beta = 0.85 \text{ W}$ , $\omega = 0.005 \text{ Hz}$ , $R_{p,off} = 100\text{K/W}$ , $C_{sink} = 0.1\text{J/K}$ , and $\Delta T_s = 2^\circ\text{C}$ . . . . .	42
3.8	Source temperature for Case 1 with and without source temperature control, $\beta = 0.85 \text{ W}$ , $\omega = 0.005 \text{ Hz}$ , $R_{p,off} = 100\text{K/W}$ , $C_{sink} = 0.1\text{J/K}$ , and $\Delta T_s = 2^\circ\text{C}$ . . . . .	42
3.9	Source and hold and cold side of the TE temperaure histories for Case 1 with active control once system reached steady state, $\beta = 0.85 \text{ W}$ , $\omega = 0.005 \text{ Hz}$ , $R_{p,off} = 100\text{K/W}$ , $C_{sink} = 0.1\text{J/K}$ , and $\Delta T_s = 2^\circ\text{C}$ . . . . .	44
3.10	Source and hold and cold side of the TE temperaure histories for Case 1 without active control once system reached steady state, $\beta = 0.85 \text{ W}$ , $\omega = 0.005 \text{ Hz}$ , $R_{p,off} = 100\text{K/W}$ , $C_{sink} = 0.1\text{J/K}$ , and $\Delta T_s = 2^\circ\text{C}$ . . . . .	44
3.11	Source and heat flow transients for Case 1 with active control once system reached steady state, $\beta = 0.85 \text{ W}$ , $\omega = 0.005 \text{ Hz}$ , $R_{p,off} = 100\text{K/W}$ , $C_{sink} = 0.1\text{J/K}$ , and $\Delta T_s = 2^\circ\text{C}$ . . . . .	45
4.1	Variable air-gap experimental set-up schematic . . . . .	52
4.2	Power output ratio improvements for constant heat input and $C_s = 38.5, 100$ , and $300 \text{ J/K}$ as a function of $\Delta T_s$ . . . . .	55
4.3	Source temperature and TE output power with $C_s = 100\text{J/K}$ , and $\Delta T_s = 10^\circ$ . . . . .	56
4.4	Source temperature and TE output power with $C_s = 100\text{J/K}$ , and $\Delta T_s = 25^\circ$ . . . . .	56

4.5	Finite difference model and experimental power output ratio improvements as a function of thermal capacitance ratio . . . . .	60
4.6	Finite difference results for constant heat input for $Q_{in} = 32.7W$ , $C_s = 300J/K$ , and $T_{s,max} = 160^\circ C$ . . . . .	62
4.7	Experimental results for constant heat input for $Q_{in} = 32.7W$ , $C_s = 300J/K$ , and $T_{s,max} = 160^\circ C$ . . . . .	62
5.1	Front view of horizontal MEMS bimaterial beam. . . . .	65
5.2	Plot of ambient temperature versus deflection of the tip of the residual stress thermal switch. . . . .	67
5.3	Photograph of fabricated horizontal MEMS bimaterial beam design. . . . .	71
5.4	Front view of vertical MEMS bimaterial beam. . . . .	71
5.5	Schematic of wax well thermal switch. . . . .	75
5.6	Simplified 1-D conduction boundary condition . . . . .	76
5.7	Schematic of micro heat pipe array. . . . .	80
5.8	Illustration of micro heat pipe with design variables. . . . .	81
5.9	Saturation pressure and temperature for 1-Propanol [132]. . . . .	82
6.1	MEMS fabrication process for micro heat pipe array. . . . .	88
6.2	Drawing for final design of micro heat pipe array. . . . .	90
6.3	Photograph of final design of micro heat pipe array. . . . .	91
6.4	Schematic for experimental set-up for thermal switch temperature charac- terization. . . . .	92
6.5	Section A, schematic for experimental set-up for filling the micro heat pipe. . . . .	93
6.6	Effective thermal resistance of copper heat spreader accounting for thermo- couple holes. . . . .	96

6.7	Plot of thermal resistance of thermal switch with propanol as a function of source temperature with a liquid volume fraction of 1. . . . .	100
6.8	Plot of source temperature with a thermal switch with propanol with a liquid volume fraction of 1 at heat input of 10 W. . . . .	100
6.9	Plot of thermal resistance of thermal switch with propanol as a function of source temperature with a liquid volume fraction of 1 at heat input of 10 W. . . . .	102
6.10	Plot of thermal resistance of thermal switch as a function of source temperature with a liquid volume fraction of 0.3 of propanol. . . . .	102
6.11	Plot of thermal resistance of thermal switch as a function of source temperature with a liquid volume fraction of 0.1 of propanol. . . . .	103
6.12	Saturation pressure and temperature for Decane [139]. . . . .	105
6.13	Plot of thermal resistance of thermal switch as a function of source temperature with a liquid volume fraction of 0.1 of decane. . . . .	105
6.14	Plot of thermal resistance of thermal switch as a function of source temperature with a liquid volume fraction of 0.2 of decane. . . . .	107
6.15	Plot of thermal resistance of thermal switch as a function of source temperature with a liquid volume fraction of 0.05 of decane. . . . .	107
7.1	Illustration of macro-scale heat pipe design for a thermal switch. . . . .	111
B.1	Source temperature and TE output power with $C_s = 38.5\text{J/K}$ , and $\Delta T_s = 20^\circ\text{C}$ . . . . .	114
B.2	Source temperature and TE output power with $C_s = 38.5\text{J/K}$ , and $\Delta T_s = 15^\circ\text{C}$ . . . . .	115
B.3	Source temperature and TE output power with $C_s = 38.5\text{J/K}$ , and $\Delta T_s = 10^\circ\text{C}$ . . . . .	116
B.4	Source temperature and TE output power with $C_s = 100\text{J/K}$ , and $\Delta T_s = 20^\circ\text{C}$ . . . . .	117
B.5	Source temperature and TE output power with $C_s = 100\text{J/K}$ , and $\Delta T_s = 15^\circ\text{C}$ . . . . .	118
B.6	Source temperature and TE output power with $C_s = 100\text{J/K}$ , and $\Delta T_s = 10^\circ\text{C}$ . . . . .	119
B.7	Source temperature and TE output power with $C_s = 300\text{J/K}$ , and $\Delta T_s = 20^\circ\text{C}$ . . . . .	120

B.8	Source temperature and TE output power with $C_s = 300\text{J/K}$ , and $\Delta T_s = 15^\circ\text{C}$ .	121
B.9	Source temperature and TE output power with $C_s = 300\text{J/K}$ , and $\Delta T_s = 10^\circ\text{C}$ .	122
C.1	Source temperature and TE output power with $C_s = 100\text{J/K}$ , $\Delta T_s = 30^\circ\text{C}$ , and $f = 0.000278\text{Hz}$ .	124
C.2	Source temperature and TE output power with $C_s = 100\text{J/K}$ , $\Delta T_s = 20^\circ\text{C}$ , and $f = 0.000278\text{Hz}$ .	125
C.3	Source temperature and TE output power with $C_s = 100\text{J/K}$ , $\Delta T_s = 10^\circ\text{C}$ , and $f = 0.000278\text{Hz}$ .	126
C.4	Source temperature and TE output power with $C_s = 100\text{J/K}$ , $\Delta T_s = 30^\circ\text{C}$ , and $f = 0.00333\text{Hz}$ .	127
C.5	Source temperature and TE output power with $C_s = 100\text{J/K}$ , $\Delta T_s = 20^\circ\text{C}$ , and $f = 0.00333\text{Hz}$ .	128
C.6	Source temperature and TE output power with $C_s = 100\text{J/K}$ , $\Delta T_s = 10^\circ\text{C}$ , and $f = 0.00333\text{Hz}$ .	129
C.7	Source temperature and TE output power with $C_s = 100\text{J/K}$ , $\Delta T_s = 30^\circ\text{C}$ , and $f = 0.000556\text{Hz}$ .	130
C.8	Source temperature and TE output power with $C_s = 100\text{J/K}$ , $\Delta T_s = 20^\circ\text{C}$ , and $f = 0.000556\text{Hz}$ .	131
C.9	Source temperature and TE output power with $C_s = 100\text{J/K}$ , $\Delta T_s = 10^\circ\text{C}$ , and $f = 0.000556\text{Hz}$ .	132

## Tables

### Table

2.1	Common materials for TE device fabrication. . . . .	16
3.1	Physical and spatial variables that remain fixed for all numerical cases studied	28
3.2	Physical and spatial variables that remain fixed for all numerical cases studied	38
3.3	Numerical cases evaluating effects of lower set-point temperature for variable heat flow input, $Q_{in} = \beta + \beta \sin \omega t$ . . . . .	39
3.4	Numerical cases evaluating effects of thermal switch high to low resistance ratio for variable heat flow input, $Q_{in} = \beta + \beta \sin \omega t$ . . . . .	40
3.5	Numerical cases evaluating effects of sink thermal capacitance and resistance for variable heat flow input, $Q_{in} = \beta + \beta \sin \omega t$ . . . . .	40
3.6	Numerical cases evaluating effects of frequency of heat input for variable heat flow input, $Q_{in} = \beta + \beta \sin \omega t$ . . . . .	40
3.7	Numerical cases evaluating constant heat flow input. . . . .	41
3.8	Numerical cases evaluating constant heat flow input. . . . .	46
3.9	Numerical cases evaluating constant heat flow input. . . . .	47
3.10	Physical and spatial variables for ZT sensitivity study for constant and cyclic heat input . . . . .	48
3.11	Summary of overall energy recovery power ratio with and without control for variable heat input and varying ZT values . . . . .	48

3.12 Summary of overall energy recovery power ratio with and without control for constant heat input and varying ZT values . . . . .	48
3.13 Physical and spatial variables that remain fixed for all constant heat input simulated cases studied for realistic conditions . . . . .	49
3.14 Summary of simulated and experimental power output ratio improvements for constant heat input. . . . .	50
4.1 Physical and spatial variables that remain fixed for all constant heat input experimental cases studied. . . . .	55
4.2 Summary of the optimal experimental power output ratio improvements for constant heat input and variable source capacitance . . . . .	57
4.3 Physical and spatial variables that remain fixed for all variable heat input experimental cases studied. . . . .	59
4.4 Summary of the optimal experimental power output ratio improvements for variable heat input and variable source capacitance . . . . .	59
5.1 Physical parameters for MEMS horizontal residual stress beams. . . . .	67
5.2 Physical parameters for MEMS vertical residual stress beams. . . . .	72
5.3 Physical parameters for wax wells. . . . .	79
5.4 Physical dimensions for micro heat pipe. . . . .	81
5.5 Properties for Silicon and SU8. . . . .	81
5.6 Physical parameters for evaporator section in micro heat pipe. . . . .	83
5.7 Physical parameters for condenser section in micro heat pipe. . . . .	85
5.8 Thermal switch design comparison. . . . .	87
6.1 Experimental uncertainty associated with heat flow, source temperature, and thermal resistance of thermal switch. . . . .	98



## 6.2 Physical and spatial variables that remain fixed for all numerical cases studied 99

## **Chapter 1**

### **Introduction**

#### **1.1 Motivation**

Energy conservation is increasingly important in the minds of Americans and societies across the world. With global warming, oil shortages predicted, and energy crises looming in the future, many world citizens are demanding change; change in how industry does business, how the government handles environmental issues, and how each individual uses energy [1]. To this end, this dissertation intends to investigate a new energy harvesting technique for waste heat recovery for an aircraft. However, there are implications of this study to other energy harvesting applications.

#### **1.2 Thermal Management and Control**

As technology demands a decrease in size and mass of aircraft and satellites, there is an associated demand for new thermal management systems. For example, relative to space applications, future micro-spacecraft are expected to be less than 0.5 m in size, requiring less than 50 W of power, most of which is dissipated as heat in a very small package [2, 3, 4, 5, 6]. Ultimately, this decrease in payload size and performance of aircraft can be limited by thermal management issues.

Relative to aircraft, the thermal challenges are associated primarily with high heat flux thermal management issues such as dissipating high heat fluxes, heat transport scale-

up issues, directed energy pulse power peaks, and maintaining temperature gradients of less than  $\pm 2$  °C. The overall specific power required is restricted by a lack of high flux thermal management solutions [7]. New methods of heat dissipation are needed to disperse at least 100 W/cm<sup>2</sup> in future micro-spacecraft and aircraft [8]. Reaching this goal will require new ways of thinking and new technologies.

Traditional thermal control hardware for aerospace applications can be categorized as passive or active systems. An active system is needed when passive thermal control is unable to deal with environmental extremes. Thermal surface finishes, mechanical mounting, multiple layer insulation (MLI), use of phase change materials (PCMs), and pumped fluid loops are examples of passive thermal control. Thermal surface finishes or coatings can be used to minimize solar energy that is absorbed. Some components are mounted such that the heat from electrical components is transferred by conduction to the aircraft structure [9]. Multilayer insulation is used to prevent heat loss and/or excessive heating from the external environment. PCMs and heat sinks are passive, very reliable, and help to provide some control over the equipment temperatures through increased thermal capacitance. They are usually used for thermal control of electronic components with short-duty-cycle. Pumped fluid loops provide efficient transfer of large amounts of thermal energy by means of forced liquid convective cooling.

Some examples of active thermal control devices for low gravity include: heaters; louvers; radiators; and thermoelectric coolers. Heaters, thermostats, and solid state controllers are active devices that are used when passive methods do not achieve desired temperature control. Louvers are active elements that provide variable radiation from surfaces. These are most often used to reject heat to space by radiators. Thermoelectric coolers are active devices that can be used for local cooling. They are simple, reliable, and compact, but have problems with structural integrity, thermal stresses and low coefficient of performance or efficiency [10, 11].

Some possible solutions for high heat flux cooling requirements with limited payload capacity are: spray cooling; microchannel and subcooled boiling; loop heat pipes; capillary pumped loops; energy storage phase change material; and spray cooling arrays [12, 13]. These solutions have resulted in a 10 to 100 times improvement in heat dissipation rates to heat fluxes approaching  $600 \text{ W/cm}^2$ . Because modern aircraft utilize more electricity, the need for thermal management for remote loads instead of the central hydraulic system has also increased. One solution is to use the fuel as a heat sink, but this can lead to an unacceptable increase in fuel temperature that could cause the fuel to chemically decompose [14]. Forced convection of a single phase liquid or gas is convenient, but systems utilizing multi-phase fluid could achieve more effective heat transfer with less volume [15].

### **1.3 Energy Harvesting and Waste Heat Recovery**

Energy harvesting is the science of recovering waste energy and converting it into usable electrical energy. There are many sources of energy that can be scavenged including light, electromagnetic energy, vibrational energy, electrostatic energy, and heat [16].

Energy harvesting in thermal applications involves conversion of waste heat to primarily electrical energy by using thermoelectric (TE) devices. The recent focus on environmental concerns has renewed interest in TE power generation [17]. TE devices can produce electrical energy when a temperature gradient is placed across the device. The technical details of how TE devices work are discussed in the next chapter.

TE devices have been used in a variety of energy harvesting applications including the automotive, steel, and chemical industries [18, 19, 20]. TE power generation applications are categorized as either low power or high power generation. An example of a low power generation application is associated with the harvesting of ambient heat for remote devices traditionally powered with batteries. TE devices can produce low grade power for

remote sensors for control, safety, and surveillance and without the maintenance of batteries [21, 22, 16, 23]. These applications are becoming more attractive because of progress in microsystem fabrication [24, 25].

High power energy harvesting applications include solar TE generation and waste heat generation [26, 27]. Solar thermal collectors have very low efficiencies but when combined with TE devices, the waste heat is converted into usable electricity increasing the overall efficiency to 40%. Other waste heat applications include power generation for diesel and gas turbine cogeneration used in manufacturing sectors such as "chemical product, food processing, oil refining, palm oil mills petrochemical, pulp and paper rice mills, sugar mills, and textiles" [28]. The efficiencies of these systems range from 10% to 40% and can generate up to 100 MW of net power [28, 19].

Waste heat recovery applications can also reduce the waste heat that must be rejected by the system, thereby reducing the high heat flux removal demands at least slightly. The reduction in magnitude of the high heat flux removal system reduces the overall exergy destruction of the entire aircraft thermal management system by reducing the heat needing to be rejected and the mass related with the cooling systems [29].

#### **1.4 Thermal Switches in Surveillance Aircraft Applications**

The application of interest to this research is a unmanned surveillance aircraft designed to loiter for several days between fueling while observing the environment as illustrated in Fig. 1.1. The aircraft wingspan is to include integrated radar arrays which dissipate approximately 30-50 W/cm<sup>3</sup> of waste heat. A heat sink subsystem and energy harvesting subsystem are intended to be integrated into the aircraft skin. The energy harvesting subsystem is to be comprised of TE devices. A TE device can convert a temperature drop across the device into electrical energy by utilizing the Seebeck effect. The TE device is

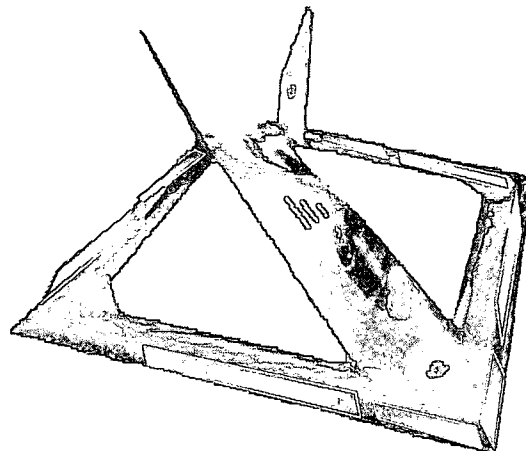


Figure 1.1: Illustration of representative unmanned surveillance aircraft.

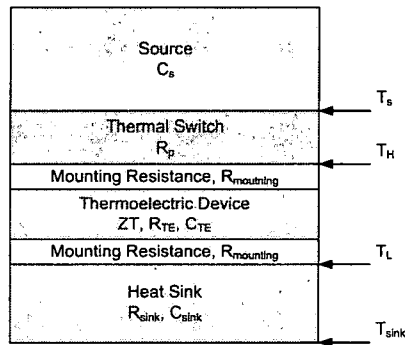


Figure 1.2: Schematic of energy harvesting system with TE device and thermal switch.

placed in between the radar elements (the heat source) and the aircraft skin (the heat sink). The larger the temperature drop across the TE device, the higher the efficiency of the waste heat recovery system. Due to variations in the source and sink temperatures associated with flying at different altitudes, as well as manufacturing variance of the radar systems, the efficiency across this device could be less than optimal, e.g., the radar arrays may be operating at less than maximal temperature. To provide a solution for waste heat removal from the radar array, the concept of a thermal switch is introduced. The thermal switch is a device that can either passively or actively change thermal resistance. If a thermal switch is placed between the heat source and TE device, it can be used to maintain a near constant source temperature at near the maximum source temperature allowed by varying the thermal resistance of the switch, thereby maximizing the temperature difference across the TE device when heat is permitted to flow through the device. The time-averaged efficiency of the energy harvesting system ideally can be higher than the same system without the switch if certain conditions exist.

The waste heat recovery system with thermal switch source temperature modulation, shown schematically in Fig. 1.2 is proposed to harvest waste heat from a constant or variable heat source using TE devices. In this figure, each layer has defined thermal

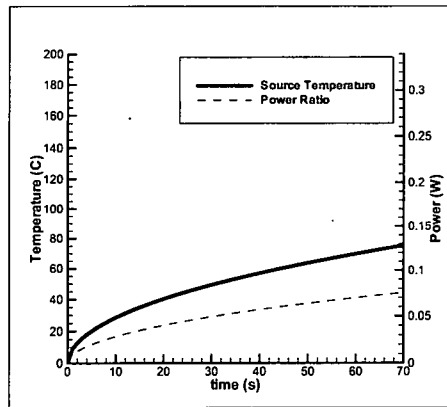


Figure 1.3: Illustration of representative energy harvesting system without a thermal switch.

resistances and capacitances. Note the mounting resistance layers on either side of the TE device. These layers are used to model the thermal resistance of the ceramic plates and epoxy applied to both surfaces of the TE device and the contact resistance.

As an illustration of a typical energy harvesting system with no thermal switching, Fig. 1.3 shows source temperatures and power dissipation plotted as a function of time starting from ambient conditions. Also noted is the maximum allowable source temperature of 160°C. In practice, this system must be designed for worst case heat input scenarios due to variations in source heat output, sink temperature, thermal resistance, and manufacturing. This conservative design can force the system to operate at least at times well below the maximum temperature of the source, therefore reducing the temperature drop across the TE device and thus lowering the efficiency of the energy harvesting system.

In order to compensate for these variations, the representative waste heat recovery system shown in Fig. 1.4 is proposed to maximize the thermoelectric energy recovery from the system through the addition of a thermal switch, located between the source and the TE device. Again, in this illustration of a typical energy harvesting system, source temperature and power into the TE device are plotted as a function of time. The ideal thermal switch



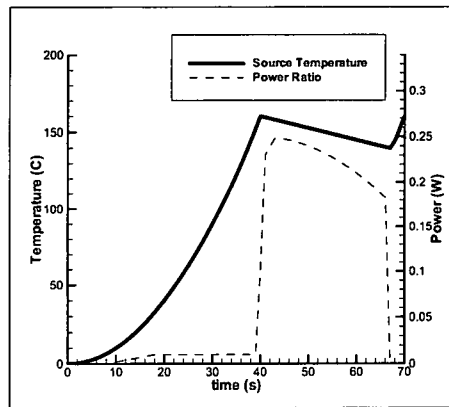


Figure 1.4: Illustration of representative energy harvesting system with a thermal switch.

has a controllable thermal resistance. As shown in the representative plot, when the heat input is near maximum, the thermal resistance of the thermal switch is set to a minimum to prevent the source from exceeding its maximum temperature. In this state the heat flows freely into the TE device, maximizing the temperature drop across the TE device and the efficiency of the energy harvesting system. When the heat input is off-peak, the thermal resistance is increased to dominate the thermal resistances in the system, forcing energy storage in the heat source, thus causing an increase in source temperature. In this state very little heat ideally flows through the TE device. Once the source temperature reaches the maximum operating temperature, the thermal resistance of the switch is once again minimized. This sequence of events repeats to allow greater work to be extracted from the system by restricting heat to flow through the TE device only during maximum source temperature and therefore maximum temperature drop across the TE device. This control results in greater time-averaged power output to power input ratios where the power output is the energy harvested by the TE device and the power input is the heat dissipation from the source.

This novel research proves the benefit of a thermal switch for use in union with TE

devices as a robust waste heat recovery system for aircraft use, and more generally for any use. Two analytical approaches are investigated to evaluate the potential of source temperature modulation on TE power output. The first approach is based on a simple RC-equivalent model and is useful in identifying the parameters controlling the TE efficiency for the integrated system. The second approach is a finite difference approach with source temperature feedback. The results from this approach supports the feasibility of source temperature modulation for enhanced energy recovery. At this point, a variable air gap experiment, used to vary the thermal resistance between source and the TE device, is employed to verify the benefits of a thermal switch for energy recovery. With verifications, a more practical thermal switch design is posed, analyzed, developed, and tested. Numerous journal articles and conference publications were produced from this research and is outlined in Appendix A.

## **Chapter 2**

### **Background**

The development of an energy harvesting system for the surveillance aircraft application at hand requires a base of knowledge in a variety of technical areas. One of these areas include TE devices, materials used to manufacture TE devices, and understanding the transient behavior of these devices. A second area of interest is thermal switches and existing designs and applications. The final technical area includes heat pipes and phase change heat transfer. Though much work has been done in each individual technical area, the combination of TE devices and thermal switches to optimize harvesting energy is a new concept. With an appropriate background in these technical areas, a solution for our energy harvesting application can be explored.

#### **2.1 TE Device**

Thermoelectric devices are solid-state devices that can either produce electrical energy when a temperature gradient is placed across the device or used in the opposite manner by producing a temperature difference when provided electrical energy. The Peltier effect occurs when electrical current flows through dissimilar conductors resulting in a temperature gradient across the system, which is shown in Fig. 2.1. The Seebeck effect is the opposite of the Peltier effect, as it results in electrical current that is driven by a temperature gradient across the system. This allows the TE device to be used in waste heat recovery or

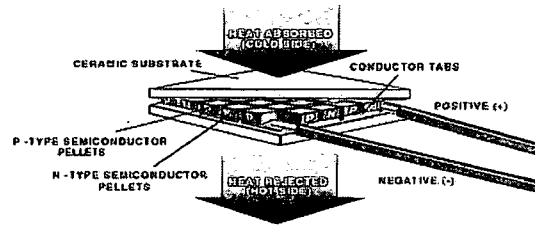


Figure 2.1: Schematic of TE device.

energy harvesting [30]. The efficiency of a TE device operating in steady or quasi-steady conditions for energy recovery is described by equation 2.1 [31, 32, 33].

$$\eta = \frac{T_{TE,H} - T_{TE,L}}{T_{TE,L}} \left( \frac{\sqrt{1 + ZT} - 1}{\sqrt{1 + ZT} + \frac{T_{TE,L}}{T_{TE,H}}} \right) \quad (2.1)$$

where  $T_H$  represents the temperature on the hot side of the TE device,  $T_L$  is the temperature on the cold side of the device,  $ZT$  is the figure of merit of the thermoelectric material. The  $ZT$  value is determined by material characteristics and is typically 1, at the material level (excluding packaging), but state of the art devices are capable of producing TE devices with  $ZT$  values up to 5 [34]. TE devices have been used in many traditional aircraft thermal control applications as heat pumps to provide local cooling. They have a reputation for being very simple, reliable, and compact. However, problems exist with their structural integrity, thermal stresses, and low coefficient of performance (COP) or efficiency [11].

### 2.1.1 Thermoelectric Effect

The thermal to electrical energy conversion process of a TE device can be better understood at the p-n junction level. A TE device used for power generation utilizes many p-n junctions in series with a load resistor as seen in Fig. 2.2. When the p-type material is joined with the n-type material, their electrical potentials align,  $\Delta E_f$ , as shown in Fig. 2.3, and the temperatures at this junction are equal. This occurs due to the diffusion of

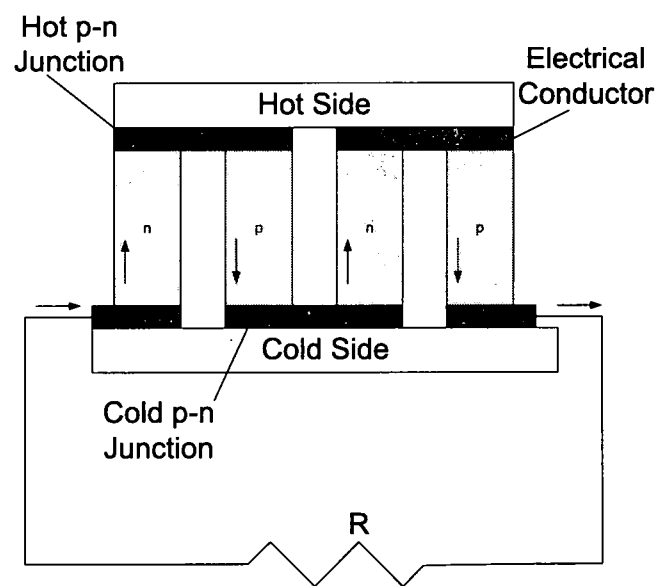


Figure 2.2: Schematic of a TE device p-n junction.

electrons from the n-type material into the p-type material and the diffusion of holes from the p-type material into the n-type material. This results in positively charged immobile ions in the n-type material and negatively charged ions in the p-type material. At the p-n junction interface, there now exists an electrostatic potential barrier,  $\Delta E$ . At the hot p-n junction the potential,  $\Delta E_H$  is smaller than the electrical potential at the cold junction  $\Delta E_L$ , thus causing the holes and electrons to drive towards the cold p-n junction. The hot p-n junction is depleted and the temperature starts to change. Now the holes and electrons from the cold junction drive towards the hot junction to compensate. Therefore the net effect is electrical current flow [35].

The thermoelectric effect or the ability of a material to convert a temperature difference into electric power is driven by the Seebeck coefficient, given by equation 2.2,

$$S = -\frac{d\Phi}{dx} / \frac{dT}{dx} \quad (2.2)$$

where  $\Phi$  is the electrochemical potential, and  $dT/dx$  is the temperature gradient across the material [35]. The ZT value of a TE device can also be written as a function of the Seebeck coefficient,

$$ZT = \frac{S^2 T}{\rho k} \quad (2.3)$$

where  $\rho$  is the resistivity,  $k$  is the thermal conductivity, and  $T$  is the average temperature of the TE material [36].

### 2.1.2 Transient Effects

Transient behavior of the thermal-electrical energy conversion processes in TE devices for use as power generators has been a well studied topic [37, 38, 39, 40, 41, 42, 43, 44]. As a cooler, the TE device instantly adsorbs electrical energy at the p-n junctions

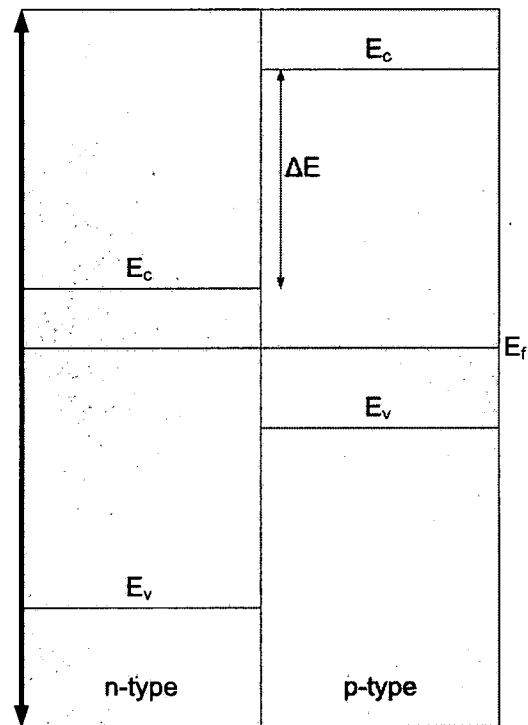


Figure 2.3: Energy diagram of a TE device p-n junction.

when current is applied. Simultaneously, Joule heating results, but this thermal energy diffuses towards the p-n junction at a much slower rate than the electron flow. As a result, the Seebeck effect and the effective ZT value are enhanced, and therefore the TE device performance is temporarily improved until the Joule heating effects reach steady-state. When the TE device operates as a generator, Joule heating diffusion begins at the p-n junction when a temperature difference is applied across the device. Electrical energy adsorption commences almost instantaneously, thus temporarily degrading the Seebeck effect, effective ZT value, and the TE device performance until Joule heating reaches steady-state.

One previous study of a TE refrigerator showed that micro-second current pulses could enhance the Seebeck effect and therefore cooler performance [45]. For a typical bismuth telluride TE device, the transient effects occur for very small time durations relative to the conceived switching time. The characteristic timescale for the dynamic response of a typical bismuth telluride TE device,  $\tau_{TE}$ , can be estimated using equation 2.4, and is seen to be just a fraction of a second [43]. For emerging and next generation TE technologies with substantially reduced mass, much lower time scales are realized.

$$\tau_{TE} = \frac{cmI}{kA} = \frac{c\rho l^2}{k} = \frac{(16 \text{ J/kgK})(7730 \text{ kg/m}^3)(0.002 \text{ m})^2}{3 \text{ W/mK}} = 0.16 \text{ s} \quad (2.4)$$

where  $c$  is the specific heat,  $m$  is the mass,  $l$  is the length,  $A$  is the cross-sectional area, and  $\rho$  is the density of the thermoelectric material.

In contrast, the nominal time scale for the rest of the energy harvesting system for the surveillance aircraft application,  $\tau_{system}$ , and many others, as shown in equation 2.5, can be estimated from the controlling system thermal resistance and capacitance due respectively to the TE device and the radar heat source, equal to 100 K/W and 1 J/K. Thus, the time constant for the TE generator is less, by at least three orders of magnitude, than that associated with the remainder of the system considered. As a consequence, the relatively slow changes in source and sink temperature are quickly accommodated by



Table 2.1: Common materials for TE device fabrication.

p-Type	n-Type
$\text{Bi}_2\text{Te}_3$	$\text{Bi}_2\text{Te}_3$
$\text{PbTe}$	$\text{PbTe}$
$\text{Zn}_4\text{Sb}_3$	$\text{CoSb}_3$
$\text{SnTe}$	$\text{La}_2\text{Te}_3$
TAGs	$\text{SiGe}$
$\text{CeFe}_4\text{Sb}_{12}$	$\text{La}_2\text{Te}_3$
$\text{SiGe}$	
$(\text{PbSn})\text{Te}$	
$\text{Sb}_2\text{Te}_3$	

the TE device. The TE generator can then be appropriately analyzed as if operating in quasi-steady-state.

$$\tau_{\text{system}} \approx R_{\text{TE}} C_s = (100 \text{ W/mK})(1 \text{ J/kg}) = 100 \text{ s} \quad (2.5)$$

Although previous research has utilized thermal switches to create transient effects to temporarily enhance the performance of TE coolers, the use of thermal switches to maximize the source temperature to enhance power generated is a novel concept.

### 2.1.3 TE Device Materials

Currently available TE devices are usually made of heavily doped semiconductors or semimetals with large carrier concentrations, a large band gap, high electron transport, and low thermal conductivity. The common materials used TE device fabrication are outlined in Table 2.1 [46, 31, 32, 33, 47, 48, 49, 50].

One commercially available TE device using bismuth telluride ( $\text{Bi}_2\text{Te}_3$ ) states power generation over  $0.33 \text{ W/cm}^2$  for a  $200^\circ\text{C}$  temperature difference [51, 52]. Yet another commercially available bismuth telluride TE devices claims power densities greater than  $2 \text{ W/cm}^2$  for a temperature difference of  $300^\circ\text{C}$  [53]. Another commercially available TE

device utilizes thin-film technology to provide a possible cost effective power generation solution for bismuth telluride TE devices. Though only a modest amount of power is generated, the modules are small and compact with an area of  $1.12 \text{ mm}^2$  [54, 55, 56].

Recently, breakthrough developments have been reported in thermoelectric materials. Many of the breakthroughs are due to employing size effects found in nanostructured materials [57, 58, 59, 60, 61, 62]. For example, Dresselhaus et al. have demonstrated improvement in the ZT figure of merit as dimensionality is reduced from bulk to two-dimensional quantum wells to one-dimensional quantum wires to zero-dimensional nanowire superlattices [63]. In 2001, Venkatasubramanian used nanoscale superlattice materials, based on the concept of phonon blocking electron transmission, to demonstrate ZT values of 2.4 at ambient temperature, with exceptionally high power densities and  $1/40000^{\text{th}}$  of the active material mass as compared to bulk thermoelectric technology [64, 65]. Finally, P. M. Martin of the Pacific Northwest National Laboratory described progress in the scale up of thermoelectric quantum well thermoelectrics. ZT values approaching 5 were reported [66]. Thus in a mere half-decade, ZT values have increased from 1 to 5. Such advances have practical importance. Through a U.S. Department of Energy (DOE) grant, BSST is leading the development of an efficient and practical thermoelectric system that will improve automotive fuel economy by converting waste heat in automobile engine exhaust into electrical power. Bell of BSST has shown that surpassing the threshold ZT of 2 in a cost effective manner can enable significant usage of TE energy harvesting in the automotive industry [67]. Recently, John Fairbanks of the U.S. Department of Energy noted that further improvements in ZT to approximately 10 could make TE power conversion competitive with the internal combustion engine [68]. Finally, Elder et al. of BMW recently stated that for automotive applications, TE utilization is possible if the module cost is brought down to approximately 0.10 \$/W and a ZT-value above 3 can be achieved over a broad temperature range [69]. Relative to aircraft energy harvesting from

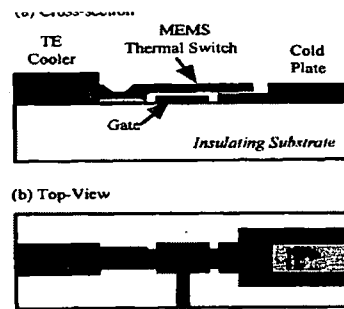


Figure 2.4: MEMS TE device and integrated thermal switch [71].

power electronics, Hallinan et al. showed that TE technology is already at a state where positive system level impact can be realized for electronic cooling applications [29, 70].

## 2.2 Thermal Switch Designs

One way to control temperature in a thermal system is to use thermal switches with variable thermal resistance to affect temperature control. Several thermal switch designs are in existence for a variety of applications. One example is the gas-gap switch for cryocoolers, which utilizes a gas-vapor-solid mixture. When a gas forms because temperatures are higher than saturation temperature, it provides fairly good heat transfer between the metal fins of the switch. When temperatures are below saturation temperature, a liquid or solid begins to form, and the heat transfer rate decreases due to low vapor pressure. With this type of a switch, the authors were able to achieve a cool-down time 21% less than the system without a thermal switch [72, 73, 74, 75, 76, 77]. Another example is active radiator tiles (ARTs) that use electrostatic actuation between two plates enclosing a vacuum. The exterior surface of this switch has a high emissivity external layer. The vacuum cavity is sandwiched by low-emissivity layers. Actuation causes the plates to contact, and permits heat to flow through easily. When the plates are separated, the leakage heat transfer is substantially less. Designers want good radiative heat flow in the ON state and

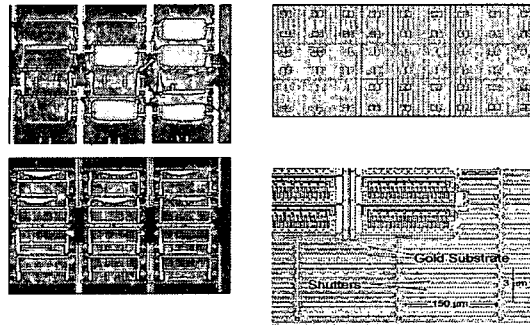


Figure 2.5: Louver design for emissivity-based thermal switch [84].

good thermal isolation between the two layers in the OFF state [78]. This device can be categorized as a variable emittance device.

Many of the emerging technologies are rooted in micro- and nano-scale technologies, including micro-electrical-mechanical systems (MEMS). Using MEMS technology, a TE device has been integrated directly with a very high frequency thermal switch to create a MEMS TE cooler [79, 80, 81, 82]. It has been shown that pulsed performance of TE devices can exceed the TE steady state performance by taking advantage of the thermoelectric transient effects. The TE device is pulsed and a cooling action takes place while the thermal switch is closed. Before the Joule and/or the Fourier heat can flow towards the cold reservoir, the switch is closed. This device, shown in Fig. 2.4, resulted in an increased cooling effect of about  $10^{\circ}\text{C}$  [71, 83].

MEMS thermal switches are also used for satellite thermal control. Two types of variable emissivity thermal switches have been developed; a MEMS louver and a MEMS shutter. The micro louver design, used on many satellites such as Hubble, Magellan, Viking, and Voyager, consists of blades that can open to change the effective emissivity by exposing the radiator lying underneath and is shown in Fig. 2.5. They can be relatively large and sensitive to the sun's position. Shown in Fig. 2.6, the shutter design does not provide as large of change in emissivity, but offers mechanical robustness [84].

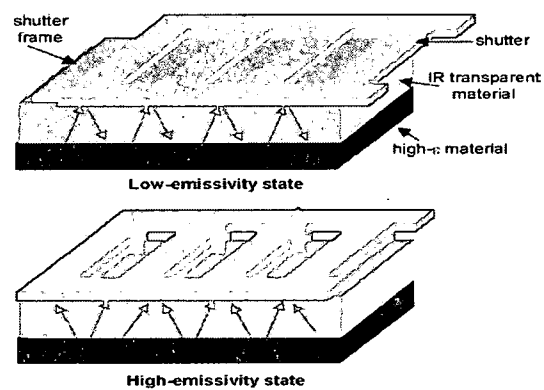


Figure 2.6: Shutter design for emissivity-based thermal switch [84].

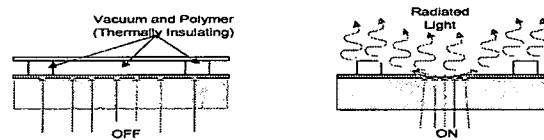


Figure 2.7: Schematic of emissivity-based thermal switch [86].

Other variable emission emissivity-based MEMS thermal switches are used for spacecraft applications. A new thermal control radiator requires input voltages on the order of 20 to 30 volts. The design consists of a gold membrane supported by NANO SU-8 (EPON epoxy based photoresist) posts, shown in Fig. 2.7. When the switch is in the 'OFF' state, the membrane is suspended above the substrate and the only heat that passes through the device leaks through the posts via conduction. In the 'ON' state, a voltage is applied across the membrane to the substrate, the membrane is pulled down to the substrate due to a capacitive force, allowing heat to flow through the membrane and radiates into space. For a membrane thickness of  $2\ \mu\text{m}$  and an effective membrane width of  $550\ \mu\text{m}$ , the authors reported a maximum conduction ratio, defined as the ratio of effective thermal conductivity when switch is off to when the switch is on, of 20,000 [85].

NASA's Mars rovers, launched in 2003, uses wax-activated thermal switches to ensure rover components stayed at a safe temperature [88]. The switches contain paraffin

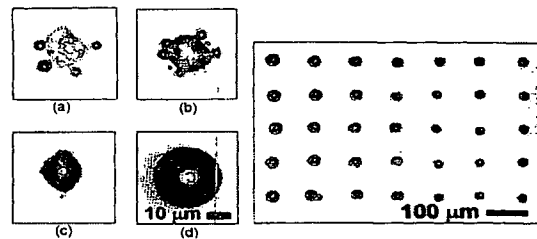


Figure 2.8: Photograph of liquid-mercury micro-droplet thermal potentiometer [87].

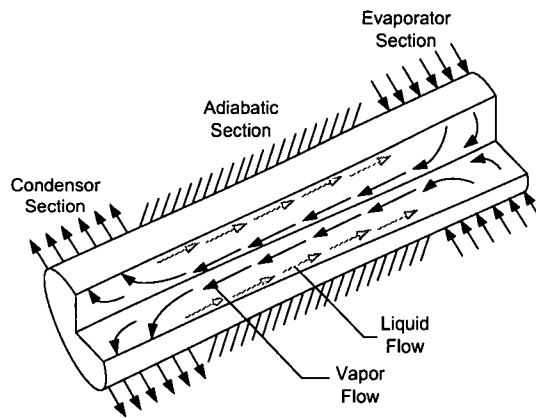


Figure 2.9: Schematic of traditional heat pipe.

wax which melt at a certain temperature. As the wax melts and expands, it pushes components together introducing a heat conduction path to the sensitive components.

A liquid-mercury micro-droplet array can also been used as a thermal switch. As reported, each drop is approximately  $31\ \mu\text{m}$  in diameter with a standard deviation of  $3\ \mu\text{m}$ . Most of the drops are resting on gold targets as shown in Fig. 2.8. When a force is applied to the drops, the contact diameter increases, therefore increasing the contact area and decreasing the thermal resistance. The authors predict that an array of 1000 droplets could produce a contact resistance change by a factor of 10 [87, 89, 90].

It was suggested by L. Kopf that a heat pipe can be used as a thermal switch at low temperatures [91]. The heat pipe, which contains a working fluid that condenses and evaporates once the system reaches a certain temperature, can be used to vary the heat flowing through system. If the temperature is well below the working temperature, very little heat flows through the switch. But if the temperature is equal to or greater than the working temperature, phase change occurs and large amounts of heat will flow through the switch.

## **2.3 Heat Pipes**

The last reference above cited the possibility of using heat pipes as thermal switches. This section provides a brief background of this technology. Heat pipes have been traditionally used in thermal management applications where large amounts of heat need to be transferred over considerable distances with a low allowable temperature drop [92, 93, 94]. Fig. 2.9 shows a schematic of a traditional heat pipe. A heat pipe is a hollow structure that consists of saturated liquid-vapor mixture and typically contains three different sections. The first section is the evaporator where heat is added to the pipe and the liquid evaporates. The vapor then flows through the adiabatic section where no heat is transferred. At the condenser section, heat is released from the pipe cooling the vapor until it condenses. The saturated liquid wicks up the side of the pipe due to capillary action until it reaches the evaporator section where the process is repeated. Capillary pressure driving this process is created by the liquid-vapor interface due to surface tension [95, 96, 97].

Micro or miniature heat pipe structures can be fabricated or easily integrated with electronics making them ideal for electronic packaging applications [98, 99, 100, 101, 102, 103]. Mallik et al. analytically proved the potential of a micro heat pipe array fabricated in a silicon chip could increase the effective thermal conductivity more than 10 times compared to the substrate alone and experimentally demonstrated that the surface temperature was reduced by 29% [101, 102].

## **2.4 Background Summary**

TE devices, thermal switches, and heat pipes have been used as thermal control/management solutions for a long time. The concept of enhancing TE power generation using thermal switches is a novel approach to waste heat recovery. The final design of our thermal switch is inspired by classical heat pipe design. Combining all three technologies



results in an innovative solution for a multifunctional aircraft skin to harvest waste heat from a radar system.

## **Chapter 3**

### **Conceptual Analysis of Energy Harvesting with Thermal Switching**

In this chapter, the benefits of thermal switching for TE energy harvesting are investigated using two analytical approaches. The first analytical model broadly identifies the important parameters in the energy harvesting system. The second model more precisely estimates the temperatures and heat flux through each component of the energy harvesting system. These approaches are discussed below.

#### **3.1 RC Equivalent Model**

A thermal RC equivalent one-dimensional spatial and transient thermal model of the thermoelectric energy recovery system is developed to identify the controlling parameters and their general impact on the TE efficiency [104, 105, 106, 107, 108, 109, 110, 111, 112]. Fig. 3.1 shows the equivalent thermal RC circuit [113], and Fig. 1.2 shows the illustrative multifunctional aircraft skin which includes the radar elements, thermal switch, TE device, and heat sink. All resistances and capacitances are shown in parallel consistent with the Cauer network representation for power electronics assuming one heat source, several different materials with corresponding resistances,  $R$ , and capacitances,  $C$ , one heat sink, and adiabatic lateral walls [114, 115, 116, 117]. All parameters used in the model are described in Table 3.1. The model consists of a variable heat source with non-negligible thermal capacitance. This heat source is directly connected to the thermal switch which

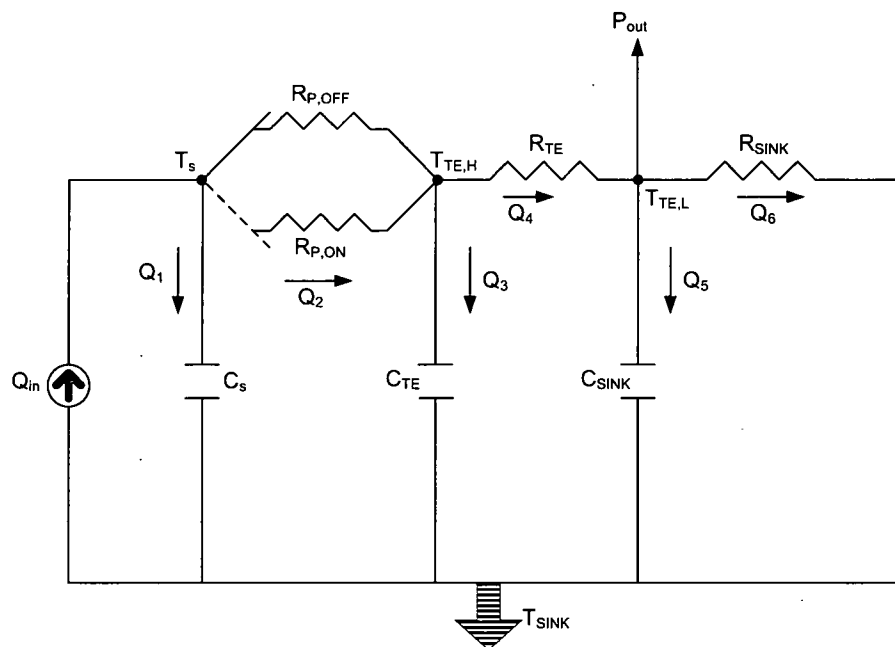


Figure 3.1: RC Equivalent Model of Energy Harvesting System with a Thermal Switch

in theory can instantaneously switch between two different states of thermal resistance,  $R_p$ . The heat conducts through the TE device and into the heat sink. Lateral temperature variations are neglected, and constant properties are considered for each of the elements. In this model, the thermal capacitance of the thermal switch is assumed small in comparison with the source. Thus  $C_p$  is assumed to be zero. The heat rejection by the source is given by  $Q_{in}$ . Although thermal to electrical energy conversion occurs throughout the TE device, it is represented in this model by  $P_{out}$  at the  $T_{TE,L}$  node [118, 119, 120]. The following analysis aims to derive the governing equations for the energy harvesting system. The TE efficiency is determined by the heat flowing through the TE device as shown in equation 3.1.

$$\eta = \frac{P_{out}}{Q_4} \quad (3.1)$$

where the efficiency of the TE device is determined from the hot side and cold side TE temperatures using equation 2.1. Kirchhoff's current law is applied to each temperature node, and yields the following equations [121].

$$Q_{in} = Q_1 + Q_2 \quad (3.2)$$

$$Q_2 = Q_3 + Q_4 \quad (3.3)$$

$$Q_4 = P_{out} + Q_5 + Q_6 \quad (3.4)$$

Using the electrical equivalent representation, the heat flowing through the source and sink thermal capacitors is given by the following equations [121].

$$Q_1 = C_s \frac{dT_s}{dt} \quad (3.5)$$

$$Q_3 = C_{TE} \frac{dT_{TE,H}}{dt} \quad (3.6)$$

$$Q_5 = C_{sink} \frac{dT_{TE,L}}{dt} \quad (3.7)$$

Table 3.1: Physical and spatial variables that remain fixed for all numerical cases studied

Parameter	Description
$Q_{in}$	Heat from source
$Q_1$	Heat flowing through source capacitance
$Q_2$	Heat flowing through thermal switch resistance
$Q_3$	Heat flowing through TE capacitance
$Q_4$	Heat flowing through TE resistance
$Q_5$	Heat flowing through sink capacitance
$Q_6$	Heat flowing through sink resistance
$T_s$	Temperature at source
$T_{sink}$	Temperature of the sink
$R_{p,off}$	Thermal resistance of switch when off
$R_{p,on}$	Thermal resistance of switch when on
$R_{TE}$	Thermal resistance of TE device
$R_{sink}$	Thermal resistance of sink
$C_s$	Thermal capacitance of source
$C_{TE}$	Thermal capacitance of TE device
$C_{sink}$	Thermal capacitance of sink
$P_{out}$	Power generated by TE device

The heat flowing through the thermal switch and the TE device relates respectively to the associated thermal resistances as shown in the following equations.

$$Q_2 = \frac{T_s - T_{TE,H}}{R_p} \quad (3.8)$$

$$Q_4 = \frac{T_{TE,H} - T_{TE,L}}{R_{TE}} \quad (3.9)$$

Combining Equations 3.1- 3.9 and rewriting in terms of source temperature yields the following differential equation relating the source temperature to heat input to the system [122, 123].

$$A_3 \frac{d^3 T_s}{dt^3} + A_2 \frac{d^2 T_s}{dt^2} + A_1 \frac{dT_s}{dt} + A_0 (T_s - T_{sink}) = B_2 \frac{d^2 Q_{in}}{dt^2} + B_1 \frac{dQ_{in}}{dt} + B_0 Q_{in} \quad (3.10)$$

$$\xi = \frac{1}{1 - \eta}$$

$$A_3 = \xi C_{sink} C_{TE} C_s R_{TE} R_p$$

$$A_2 = C_{TE} C_s R_p + \xi \left( C_{sink} (C_s R_p + C_s R_{TE} + C_{TE} R_{TE}) + \frac{C_{TE} C_s R_p R_{TE}}{R_{sink}} \right)$$

$$A_1 = C_s + C_{TE} + \xi \left( C_{sink} + \frac{C_s R_p}{R_{sink}} + \frac{C_s R_{TE}}{R_{sink}} + \frac{C_{TE} R_{TE}}{R_{sink}} \right)$$

$$A_0 = \frac{\xi}{R_{sink}}$$

$$B_2 = \xi C_{sink} C_{TE} R_{TE} R_p$$

$$B_1 = C_{TE} R_p + \xi \left( C_{sink} (R_p + R_{TE}) + \frac{C_{TE} R_p R_{TE}}{R_{sink}} \right)$$

$$B_0 = 1 + \xi \left( \frac{R_p}{R_{sink}} + \frac{R_{TE}}{R_{sink}} \right)$$

Due to its complexity, the ordinary differential equation represented by equation 3.10 cannot be solved analytically. To better understand the underlying physics in this problem, several assumptions are made to simplify this equation. First, it is assumed that the thermal resistances of the thermal switch and sink and the thermal capacitance of the sink are negligible when compared to the other parameters. Using this assumption, the RC equivalent model is simplified and is represented by Fig. 3.2.

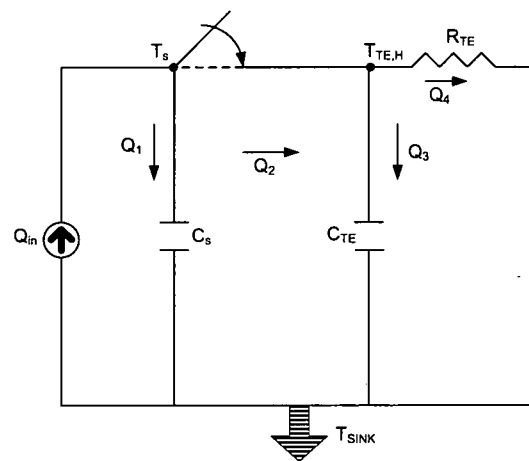


Figure 3.2: Simplified RC Equivalent Model of Energy Harvesting System with a Thermal Switch

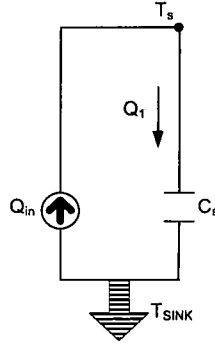


Figure 3.3: Simplified RC Equivalent Model of Energy Harvesting System with a Thermal Switch for  $t < 0$ .

The above stated problem is broken down into two time periods. First, the problem is considered before the switch is closed and therefore before  $t = 0$ . In this case, it is assumed that the switch remains open for  $t_{off}$  and is represented by Fig. 3.3. The solution for this circuit is shown in equation 3.11 [121].

$$T_s(t_{off}) - T_{sink}(t_{off}) = \frac{1}{C_s} Q_{in} t_{off} \quad (3.11)$$

Second, the time period after the switch closes is considered. The RC equivalent model is shown in Fig. 3.4, where  $C_{eq} = C_s + C_{TE}$ . Initially at  $t = 0$ , the source temperature is equal to the hot side temperature of the TE device,  $T_s(0) = T_{TE,H}$ , and the temperature difference is given by equation 3.12.

$$\Delta T(0) = T_{TE,H}(0) - T_{sink} = \frac{1}{C_s} Q_{in} t_{off} \quad (3.12)$$

Using this defined initial condition, the solution to the simplified RC equivalent model after the switch is closed is shown in equation 3.13.

$$\Delta T(t) = Q_{in} R_{TE} + Q_{in} R_{TE} \left( \frac{t_{off}}{R_{TE} C_s} - 1 \right) \exp \left( \frac{-t}{R_{TE} C_{eq}} \right) \quad (3.13)$$

This model illuminates the effects of source and TE device thermal capacitance. First, the source thermal capacitance is assumed to be much larger than the TE device thermal



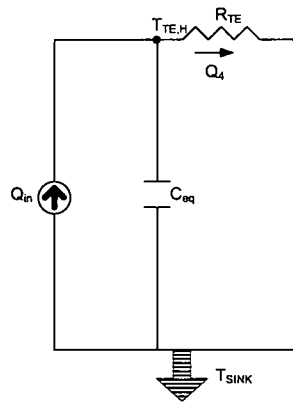


Figure 3.4: Simplified RC Equivalent Model of Energy Harvesting System with a Thermal Switch for  $t > 0$ .

capacitance,  $C_s \gg C_{TE}$ . This occurs when the source is more massive, and therefore can store more energy than the TE device, which is what is expected in practice. The initial condition remains the same as described by equation 3.12, and the final equation describing the temperature drop across the TE device becomes as shown in equation 3.14.

$$\Delta T(t) = Q_{in}R_{TE} + Q_{in}R_{TE} \left( \frac{t_{off}}{R_{TE}C_s} - 1 \right) \exp \left( \frac{-t}{R_{TE}C_s} \right) \quad (3.14)$$

From this equation, it is seen that as time progresses, the temperature difference,  $\Delta T(t)$  approaches the quantity  $Q_{in}t_{off}/C_s$ . During this time period, since  $\Delta T(t)$  is relatively large, significant power is being harvested by the TE device. So it is concluded that when the thermal capacitance of the source is greater than that of the TE device, the energy harvested by the TE device can be significant.

When the thermal capacitance of the TE device is much greater than the source, the source thermal capacitance is near zero and therefore the initial condition is represented by the following equation 3.15.

$$\Delta T(0) = 0 \quad (3.15)$$

The corresponding temperature drop across the TE device is thereby described by equation 3.16.

$$\Delta T(t) = Q_{in}R_{TE} + (0 - Q_{in}R_{TE}) \exp \left( \frac{-t}{R_{TE}C_{TE}} \right) \quad (3.16)$$

$$\begin{aligned} \Delta T(t) &\sim Q_{in}R_{TE} + (0 - Q_{in}R_{TE}) \exp(0) \\ &\sim 0 \end{aligned}$$

Thus, for a large TE device thermal capacitance, the temperature drop across the TE device for  $t > 0$  is approximately zero and therefore very little power is harvested by the TE device. In conclusion, a large thermal capacitance of the TE device is not favorable for an energy harvesting system with a thermal switch.

### 3.2 Analytical Finite Difference Model

The actively controlled thermal switch system shown in the RC equivalent model, Fig. 3.1, is modeled analytically and solved using a finite difference method shown schematically in Fig. 3.5. In the model, all material constants are considered constant. The resistance and capacitance of each material are modeled as shown in Fig. 3.6. Contact thermal resistances between the source, thermal switch, and sink are not considered. Under these assumptions, the following system of equations results. Conservation of energy is applied to each of the sub-elements to yield the following system of equations [124].

Source:

$$\frac{dT_s}{dt} = \frac{1}{C_s} (Q_{in}(t) - Q_{out}(t)) \quad (3.17)$$

Here,  $Q_{in}$  and  $Q_{out}$  are respectively the heat dissipation by the source and the heat leaving the source and passing either into the TE device (for the baseline case) and into the thermal switch otherwise.

Thermal switch:

$$\frac{dT_p}{dt} = \frac{1}{C_p} \left( k_p \frac{\partial^2 T_p}{\partial x^2} \right) \quad (3.18)$$

Sink heat exchanger:

$$\frac{dT_{sink}}{dt} = \frac{1}{C_{sink}} \left( k_{sink} \frac{\partial^2 T_{sink}}{\partial x^2} \right) \quad (3.19)$$

Finally, for the TE device, the quasi-steady assumption permits determination of the TE energy recovery efficiency from the hot side and cold side TE temperatures from equation 2.1.

The boundary conditions employed for these elements are continuity of heat flow and temperature at each interface. For convenience all temperatures are initially set equal to the sink temperature,  $T_{sink}$ . All material properties including the figure of merit,  $ZT$ , are assumed constant. Though in reality, these properties vary with temperature, since the TE

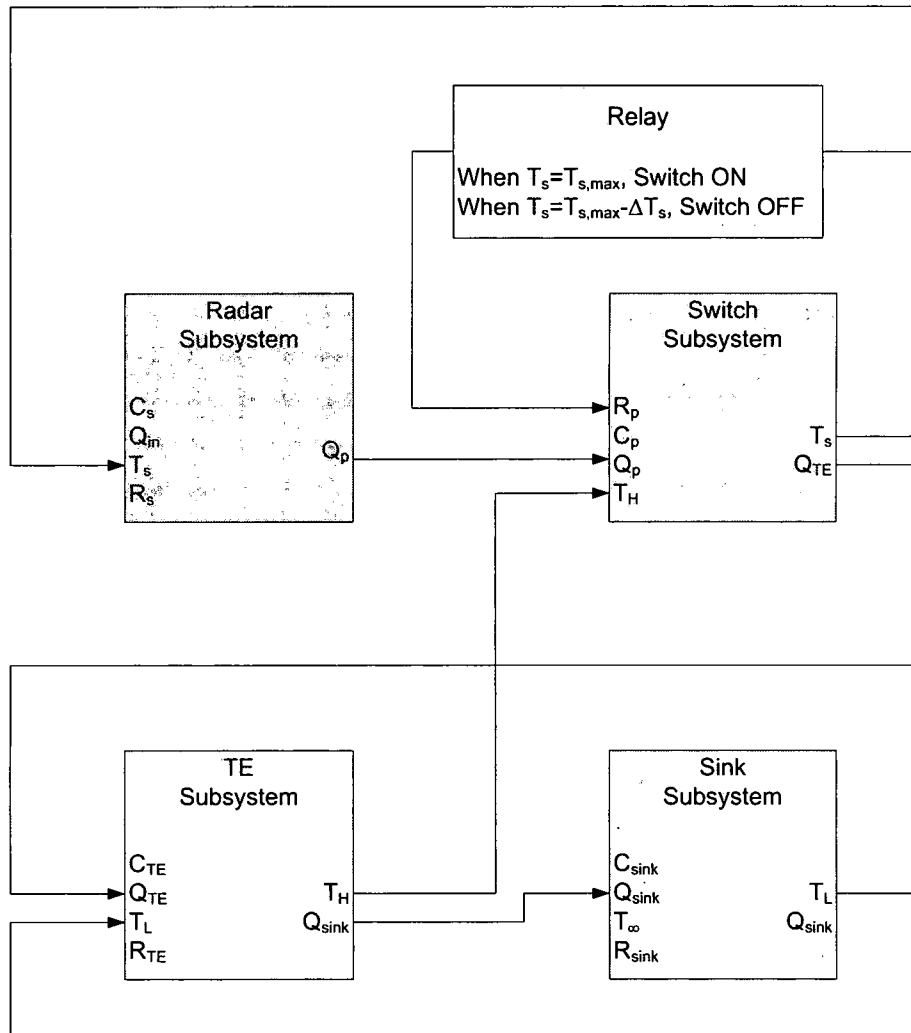
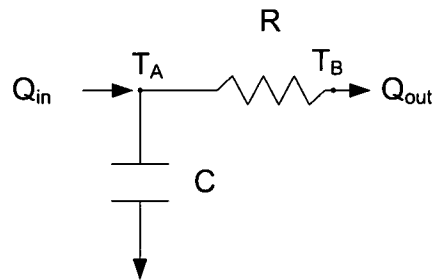


Figure 3.5: Finite difference model schematic.

a)



b)

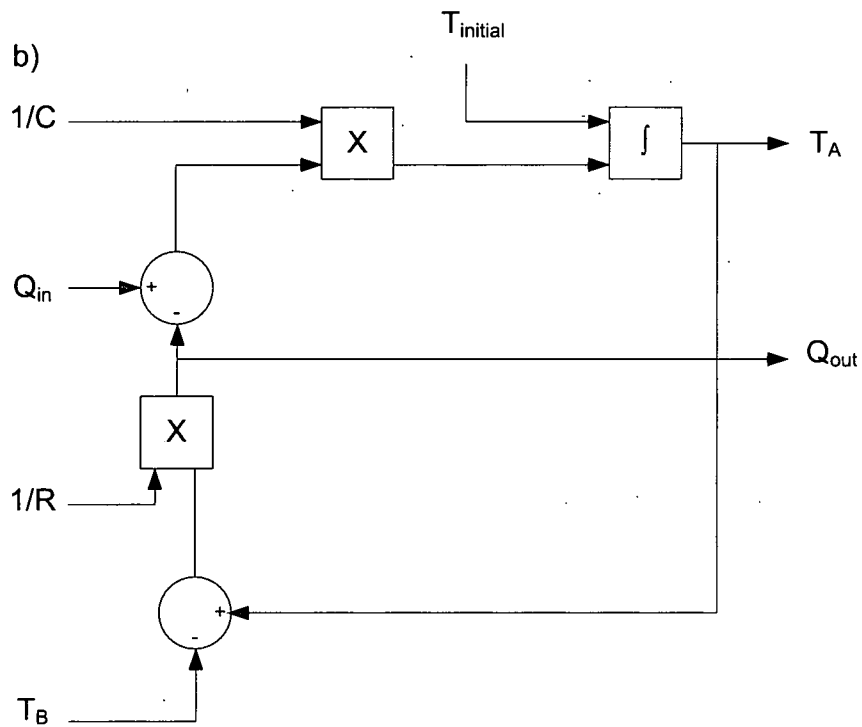


Figure 3.6: Finite difference model for one resistor and one capacitor.

device operates over a relatively small temperature range, this approximations has little effect on the final results.

The physical model given by equations 3.17-3.19 and the specified boundary and initial conditions are evaluated using a finite difference formulation. The ultimate aim of this formulation is to evaluate the time-averaged TE power output to heat input ratio shown in equation 3.20.

$$PR = \frac{P_{out}}{P_{in}} = \frac{\int W_{out}(t)dt}{\int W_{in}(t)dt} \quad (3.20)$$

where  $W_{out}$  and  $W_{in}$  represent the energy leaving the TE device and energy entering the TE device in the form of heat respectively.

### 3.2.1 Ideal Cases

The systems of equations given by equations 3.17-3.19 for both the baseline system without thermal switching and the thermal switching system are solved via a finite difference technique in a MatLab Simulink environment [125]. The benefit of using the Simulink environment for solving this dynamic system is that an active feedback schema can be easily employed as illustrated by Fig. 3.5. This active approach considered for the thermal switch model is the use of the simplest feedback schema; namely a 'relay' or 'on/off' control. More complicated control schemes do not improve the results significantly. When the temperature of the source reaches the maximum allowable or upper set-point temperature, the thermal resistance of the switch is set to its minimum value. Subsequently, as heat is drawn from the source, the source temperature diminishes. When this temperature falls below a lower set-point value, the thermal resistance is then set to its maximum value. For the purpose of the ideal numerical experiments conducted here, the upper set-point temperature is set to 150°C, and the lower set-point temperature is varied from 148°C to 100°C. Spatial and temporal grid insensitivity of all results is assured. The specific ap-

Table 3.2: Physical and spatial variables that remain fixed for all numerical cases studied

Variable	Value
$C_s$	1 J/K
$R_{TE}$	100 K/W
$R_{p,on}$	0.1 K/W
$C_{TE}$	0 J/K
$C_p$	0 J/K
$T_{sink}$	$-20^{\circ}\text{C}$
ZT	3

plication considered is associated with energy harvesting from integrated radar arrays in aircraft wings proposed for a new type of sensorcraft. A heating rate of above  $1 \text{ W/cm}^2$  and both transient (sinusoidal) and steady-state heat rates are analyzed. Consistent with this application, the source thermal capacitance,  $C_s$ , TE thermal resistance,  $R_{TE}$ , thermal switch 'on' state thermal resistance,  $R_{p,on}$ , TE thermal capacitance,  $C_{TE}$ , thermal switch thermal capacitance,  $C_p$ , sink temperature,  $T_{sink}$ , and TE ZT value given in Table 3.2 are specified for all cases.

In order to maximize the output power from the TE device, the thermal resistance of the TE device is set as the controlling thermal resistance for the system (exclusive of the thermal switch in its high thermal resistance state), since in order for the TE to be effective, a majority of the system temperature drop should occur across the TE device.

Two sets of numerical experiments are conducted. The first set is conducted to evaluate the time-averaged power output to heat input ratio defined in equation 3.20 of the TE with thermal switching relative to the baseline case for no switching subject to a sinusoidal heat input. The latter set of numerical experiments is conducted to evaluate the benefits of thermal switching for a constant heat load when operating below maximal heat loading conditions.

Table 3.3: Numerical cases evaluating effects of lower set-point temperature for variable heat flow input,  $Q_{in} = \beta + \beta \sin \omega t$ .

Case	C or NC	$\beta$ (W)	$\omega$ (Hz)	$R_{p,off}$ (K/W)	$R_{sink}$ (K/W)	$C_{sink}$ (J/K)	$\Delta T_s$ (°C)
1	NC	0.85	0.005	100	1	0.1	NA
1	C	0.85	0.005	100	1	0.1	2
2a	C	0.85	0.005	100	1	0.1	10
2b	C	0.85	0.005	100	1	0.1	25
2c	C	0.85	0.005	100	1	0.1	50

Tables 3.3-3.6 describe the test cases considered for the sinusoidal heat input numerical experiments. In these tables, the specific cases are characterized by: the control condition; heat input amplitude; frequency of heat input; thermal switch to TE thermal resistance; sink thermal resistance and capacitance; and low set-point temperature. The "no-control" (NC) condition refers to the baseline case with no thermal switch. The heat input amplitude is selected to yield a maximum source temperature nearly equal to the maximum allowable temperature 150°C for the thermal switching cases. In all, the test cases assessed are chosen to evaluate changes in lower set-point temperature, the ratio of high to low thermal resistance for the thermal switch, sink thermal resistance and capacitance, and heat input frequency. In each case  $T_{s,max} - \Delta T_s$  represents the permissible range of source temperatures. Relative to this table, variable heat input is defined by equation 3.21.

$$Q_{in} = \beta + \beta \sin \omega t \quad (3.21)$$

Table 3.7 presents similar information for the constant heat input numerical experiments. The specific cases considered are chosen to yield source temperatures below the allowable maximum for the baseline system. Thus, the no-control baseline cases repre-



Table 3.4: Numerical cases evaluating effects of thermal switch high to low resistance ratio for variable heat flow input,  $Q_{in} = \beta + \beta \sin \omega t$ .

Case	C or NC	$\beta$ (W)	$\omega$ (Hz)	$R_{p,off}$ (K/W)	$R_{sink}$ (K/W)	$C_{sink}$ (J/K)	$\Delta T_s$ (°C)
3a	NC	0.85	0.005	1000	1	0.1	NA
3b	NC	0.85	0.005	10	1	0.1	NA
3a	C	0.85	0.005	1000	1	0.1	10
3b	C	0.85	0.005	10	1	0.1	10

Table 3.5: Numerical cases evaluating effects of sink thermal capacitance and resistance for variable heat flow input,  $Q_{in} = \beta + \beta \sin \omega t$ .

Case	C or NC	$\beta$ (W)	$\omega$ (Hz)	$R_{p,off}$ (K/W)	$R_{sink}$ (K/W)	$C_{sink}$ (J/K)	$\Delta T_s$ (°C)
4a	NC	0.85	0.005	1000	10	1	NA
4b	NC	0.85	0.005	1000	0.1	0.01	NA
4a	C	0.85	0.005	1000	10	1	10
4b	C	0.85	0.005	1000	0.1	0.01	10

Table 3.6: Numerical cases evaluating effects of frequency of heat input for variable heat flow input,  $Q_{in} = \beta + \beta \sin \omega t$ .

Case	C or NC	$\beta$ (W)	$\omega$ (Hz)	$R_{p,off}$ (K/W)	$R_{sink}$ (K/W)	$C_{sink}$ (J/K)	$\Delta T_s$ (°C)
5a	NC	0.83	0.0005	1000	0.1	0.01	NA
5b	NC	1.5	0.05	1000	0.1	0.01	NA
5c	NC	1.51	0.5	1000	0.1	0.01	NA
5a	C	0.83	0.0005	1000	0.1	0.01	10
5b	C	1.5	0.05	1000	0.1	0.01	10
5c	C	1.51	0.5	1000	0.1	0.01	10

Table 3.7: Numerical cases evaluating constant heat flow input.

Case	C or NC	$Q_{in}$ (W)	$R_{p,off}$ (K/W)	$R_{sink}$ (K/W)	$C_{sink}$ (J/K)	$\Delta T_s$ (°C)
6a	NC	1.68	100	1	0.1	NA
6b	NC	0.84	100	1	0.1	NA
6c	NC	0.42	100	1	0.1	NA
6d	NC	0.21	100	1	0.1	NA
6a	NC	1.68	100	1	0.1	10
6b	NC	0.84	100	1	0.1	10
6c	NC	0.42	100	1	0.1	10
6d	NC	0.21	100	1	0.1	10

sents off-peak design conditions. These cases are posed primarily to evaluate the effect of changes in the steady heat input at constant control conditions.

Figure 3.7 shows the time history of the output to input power ratio, PR, for Case 1 with and without active control. Comparing the case of active control to no control, it is apparent that the active control case yields a substantially higher steady-state power ratio (15.9% compared to 7.2%) which is a remarkable enhancement. The reason for this improvement is apparent from examination of the source temperature time history in Fig. 3.8. Clear from this figure is that, in the absence of thermal switching, the maximum source temperature is well below that achievable with control. Thus, thermal switching yields a greater temperature drop across the TE device when heat is permitted to flow through it when the thermal switch is closed. Consequently the TE power ratio is improved relative to the no-control baseline case.

Figures 3.9 and 3.10, which show a finer presentation of the Case 1 time histories for the source as well as hot and cold side TE temperatures for respectively control and no control conditions, further illustrate this difference. With active control, the source temperature is maintained near 150°C at all times, whereas the hot side TE temperature cycles between the source temperature and just above the sink temperature as the switch thermal

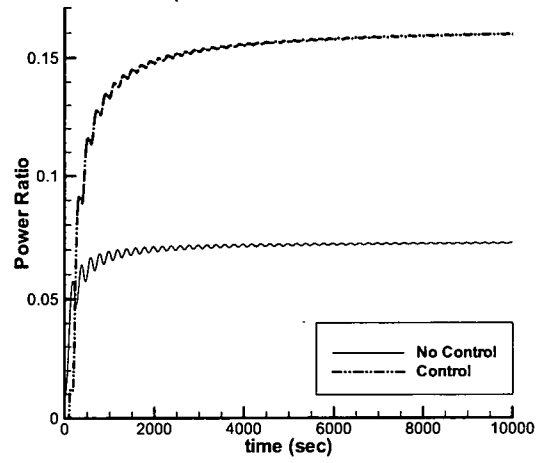


Figure 3.7: Overall TE Generator Efficiency for Case 1 with and without source temperature control,  $\beta = 0.85$  W,  $\omega = 0.005$  Hz,  $R_{p,off} = 100$  K/W,  $C_{sink} = 0.1$  J/K, and  $\Delta T_s = 2^\circ\text{C}$

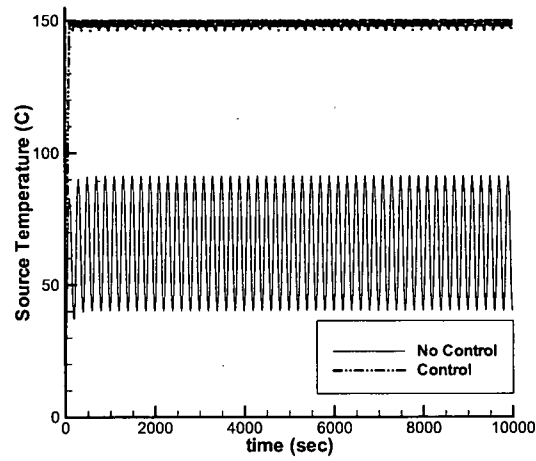


Figure 3.8: Source temperature for Case 1 with and without source temperature control,  $\beta = 0.85$  W,  $\omega = 0.005$  Hz,  $R_{p,off} = 100$  K/W,  $C_{sink} = 0.1$  J/K, and  $\Delta T_s = 2^\circ\text{C}$

resistance state is changed. The thermal switch resistance is in its low state (high conduction heat transfer from source to TE device) only when the TE hot side temperature is high, whereas the thermal switch is in its high state (poor conduction heat transfer from source to TE device) when the TE hot side temperature is low. Thus a majority of heat leaves the source when the source is near its maximum temperature. In contrast, for the baseline system, the source and TE hot side temperatures are nearly the same at all times, cycling between a low of 40°C to the maximum of 100°C.

The significance of these temperature histories is apparent from examination of Fig. 3.11, which shows the heat flow transient for Case 1 with active control. Both the heat input to the source and TE heat are shown. Clear from Fig. 3.11 is that at peak heat loading, no switching is required, since the temperature (shown in Fig. 3.9) is at its maximum. At minimum heat loading, the thermal switch is at its high thermal resistance state. At intermediate heat loading, the thermal switch is observed to cycle between its high and low thermal resistances. Most interesting is that the frequency of the switching increases as the source heat input decreases. It is noted that when the switching frequency becomes large, the assumption of quasi-steady TE operation brakes down. Case 6c represents the lowest heat input that can be appropriately considered with the quasi-steady TE model.

Table 3.8 summarizes the time averaged overall TE power ratios for the Case 1-5 simulations relative to changes in the lower set-point temperature, thermal switch high state resistance, sink thermal resistance and capacitance, and source heat frequency. Most apparent from this table is that thermal switching produces an improved power ratio for all cases considered. The improvement is seen to be somewhat insensitive to changes in the lower set-point temperature, as long as the lower set-point temperature is not too low. The improvement is also seen to be strongly dependent upon the high thermal resistance state of the thermal switch. A thermal switch high resistance value of at least 10 times the TE thermal resistance is seen to be highly desirable. The sink thermal resistance

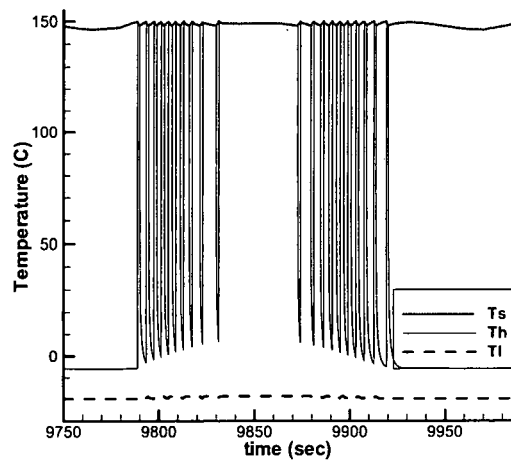


Figure 3.9: Source and hold and cold side of the TE tempaure histories for Case 1 with active control once system reached steady state,  $\beta = 0.85 \text{ W}$ ,  $\omega = 0.005 \text{ Hz}$ ,  $R_{p,off} = 100\text{K/W}$ ,  $C_{sink} = 0.1\text{J/K}$ , and  $\Delta T_s = 2^\circ\text{C}$

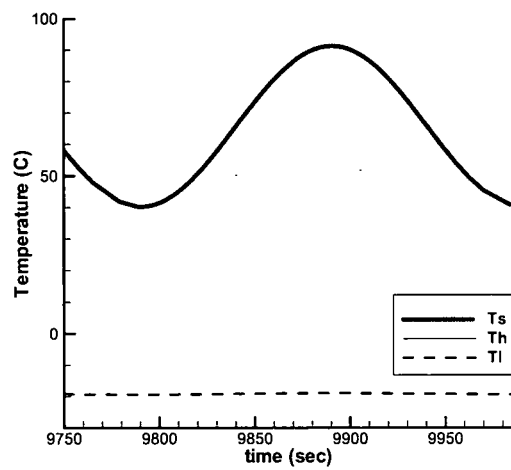


Figure 3.10: Source and hold and cold side of the TE tempaure histories for Case 1 without active control once system reached steady state,  $\beta = 0.85 \text{ W}$ ,  $\omega = 0.005 \text{ Hz}$ ,  $R_{p,off} = 100\text{K/W}$ ,  $C_{sink} = 0.1\text{J/K}$ , and  $\Delta T_s = 2^\circ\text{C}$

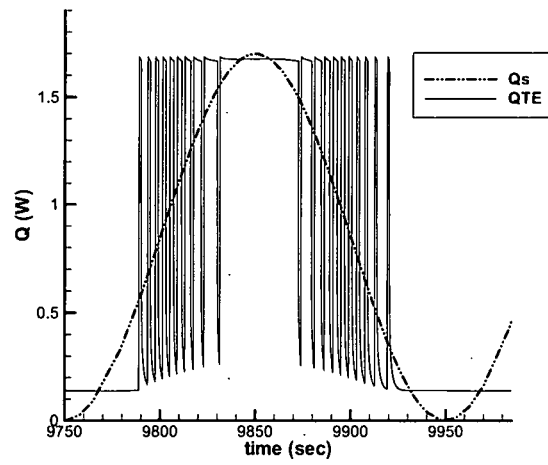


Figure 3.11: Source and heat flow transients for Case 1 with active control once system reached steady state,  $\beta = 0.85$  W,  $\omega = 0.005$  Hz,  $R_{p,off} = 100$  K/W,  $C_{sink} = 0.1$  J/K, and  $\Delta T_s = 2^\circ\text{C}$

Table 3.8: Numerical cases evaluating constant heat flow input.

Case	Parameter Changing	Change Direction	PR <sub>nc</sub> (%)	PR <sub>switching</sub> (%)
1	Lower	↓	7.2	15.9
2a	Set-point	↓	7.2	16.3
2b	Temperature	↓	7.2	16.1
2c		↓	7.2	15.7
3a	Thermal Switch	↓	7.2	17.5
3b	Resistance	↓	7.2	9.1
4a	Sink Thermal Resistance	↓	6.9	15.7
4b	and Capacitance	↓	7.3	17.8
5a	Source Heat	↑	12.6	17.9
5b	Input	↑	18.7	18.0
5c	Frequency	↑	18.9	18.9

and capacitance, which in all cases considered is at most 1/10<sup>th</sup> that of the TE device, is seen to have only a slight impact on the improvement. Of course, a larger sink thermal resistance and capacitance is seen to be detrimental to the power ratio. Finally, the results demonstrate thermal switching improvement is most prominent at moderate source heat input frequency. When this frequency is very large, thermal switching offers no improvement in energy recovery since the source temperature varies only slightly with time due to the filtering effect of the source thermal capacitance. At very low frequencies, the power ratio for the control case is still relatively high, however, the baseline no-control power ratio is greater than for higher source heat input frequencies since the source temperature is permitted to cycle hotter when the heat input is high. Thus, the source rejects heat to the TE primarily when the source temperature is high, and therefore when the temperature drop across the TE device is high.

Table 3.9 summarizes the overall power ratios for the constant heat input numerical experiments. As seen in the table, the most substantial improvement in power ratio occurs when the steady heat input rate is well below the rated maximum, which results in a source

Table 3.9: Numerical cases evaluating constant heat flow input.

Case	Parameter Changing	Change Direction	PR <sub>nc</sub> (%)	PR <sub>switching</sub> (%)
6a	Source Heat	↓	18.6	18.8
6b	Input	↓	6.6	15.7
6c		↓	2.1	13.7

temperature also well below the maximum permissible. Case 6c shows a remarkable improvement over the no-control case of 554 %. These results demonstrate that for multi-state heat generation systems, e.g., where the heat dissipation is steady-state, but can be at two or more levels, the active thermal switch concept has the most benefit, since the switch continues to maintain the source temperature at near maximum whenever heat is permitted to flow from the source to the TE device.

Finally, to investigate the feasibility of using a thermal switch in current and future applications, an additional numerical test set is considered where the TE ZT value is varied from 1 to 5. Both constant heat input and a variable heat input cases are evaluated. The test conditions for this set shown in Table 6, other than the ZT value, are identical with those employed in Case 2a, where thermal switching is demonstrated to provide sizeable benefit relative to no control. The constant heat input case assumes a heat input of 0.84 W, and the non-dimensional cyclic heat input is considered to be  $0.85+0.85\sin(0.5t)$ W.

The power ratio for the constant and cyclic heat input cases is summarized in Tables 3.11 and 3.12 for ZT values of 1, 2, 3, 4, and 5 for respectively variable and constant heat input. These results show that source temperature modulation for both have substantial benefit over the entire ZT range considered. From these results it can generally be stated that source temperature modulation via a thermal switch could be equally beneficial for currently available TE devices and for future state-of-the-art high ZT devices.

The analysis presented here reveals the significance of active thermal switching for



Table 3.10: Physical and spatial variables for ZT sensitivity study for constant and cyclic heat input

Variable	Value
$C_s$	1 J/K
$R_{TE}$	100 K/W
$R_{p,on}$	0.1 K/W
$C_{TE}$	0 J/K
$C_p$	0 J/K
$T_{sink}$	$-20^{\circ}\text{C}$
$R_{p,off}$	1 K/W
$R_{sink}$	0.01 K/W
$C_{sink}$	0.1 K/W
$\Delta T_s$	$10^{\circ}\text{C}$

Table 3.11: Summary of overall energy recovery power ratio with and without control for variable heat input and varying ZT values

ZT	$PR_{nc}$ (%)	$PR_{switching}$ (%)
1	3.4	8.6
2	5.6	13.8
3	7.2	17.5
4	8.5	20.2
5	9.6	22.5

Table 3.12: Summary of overall energy recovery power ratio with and without control for constant heat input and varying ZT values

ZT	$PR_{nc}$ (%)	$PR_{switching}$ (%)
1	3.1	7.8
2	5.1	12.4
3	6.6	15.7
4	7.7	18.2
5	8.7	20.2

Table 3.13: Physical and spatial variables that remain fixed for all constant heat input simulated cases studied for realistic conditions

Variable	Value
$C_{TE}$	25 J/K
$R_{TE}$	2.5 K/W
$T_{s,steady}$	118.8°C
$T_{s,max}$	160°C
$T_{sink}$	-20°C
$R_{p,on}$	1.75 K/W
$R_{p,off}$	120 K/W
$C_{sink}$	100,000 J/K
$R_{sink}$	0.0005 K/W
$R_{mounting}$	4.39 K/W
ZT	1

TE thermal energy harvesting in an ideal application when the heat generation may have several states, or when the heat flow or the overall thermal resistance is variable with time.

### 3.2.2 Realistic Cases

The previous section explores the effects of adding a thermal switch to an ideal energy harvesting system. Most of the parameters discussed above can not be easily tested in the lab. This section seeks to explore the effects of a thermal switch in a realistic energy harvesting system to be defined below.

Using the same finite difference model, the following thermal resistances, capacitances, temperatures and thermoelectric properties are kept constant throughout the constant heat source simulation, in an effort to represent the experimental set-up conditions, as shown in Table 3.13.

The finite difference model is used to predict the behavior of the waste heat recovery system with three different heat source thermal capacitances. The heat input,  $Q_{IN}$ , is adjusted until the steady-state source temperature is  $119 \pm 1.0^\circ\text{C}$ . For each case studied,

Table 3.14: Summary of simulated and experimental power output ratio improvements for constant heat input.

Case	1	2	3
$C_s(\text{J/K})$	38.5	100	300
$\Delta T_s(^{\circ}\text{C})$	30	25	20
$\text{PR}_{fd}(\%)$	4.6	13.1	26.8

$\Delta T_s$  is varied until a maximum power ratio is determined analytically. Table 3.14 shows the results for the analytical model with constant heat input.

As is observed from Table 3.14, the power ratio of the energy recovery system increases as the source capacitance increases. The relationship between source thermal capacitance the TE device thermal capacitance is discussed in more detail in Section 4.3. Additionally, the realistic model results prove the usefulness of a thermal switch in energy harvesting systems under conditions easily duplicated in a lab setting.

### 3.3 Conceptual Analysis Conclusions

In this chapter, two different analytical approaches were used to investigate the effectiveness of thermal switching to improve energy harvesting. The first model found that a large thermal capacitance of a TE device with respect to the source thermal capacitance was not favorable for an energy harvesting system with thermal switching. The second model showed that for constant and variable heat inputs with ideal conditions, improvements of up to 554% and 144% respectively could be realized.

## **Chapter 4**

### **Feasibility Experiment for Thermal Switch Augmentation of Energy Harvesting**

In this chapter, the feasibility of using a thermal switching to augment TE energy harvesting is investigated. The details of the experimental set-up, procedure, and results are discussed below.

#### **4.1 Experimental Set-up and Procedure**

To experimentally investigate the feasibility of employing a thermal switch to augment waste heat recovery, an experimental set-up comprised serially of a fixed heat source, a variable air gap serving as a thermal switch, a thermoelectric device and a heat sink mounted on a translation stage is employed. A schematic of this system is shown in Fig. 4.1. This set-up consists of a fixed heat source (1- inch silicon heater pad) attached to an aluminum or copper heat-spreader to simulate waste heat [126]. This heat source assembly is mounted to a fixed plate located above a lower assembly that rests on a scissor jack driven by a stepper motor thereby permitting the lower assembly to be traversed up and down. Resting on top of the scissor jack, the TE device (Hi-Z HZ-2 Thermoelectric Module with ceramic plates) is sandwiched between heat flux sensors and thermocouples. The heat sink, which is constructed of a copper plate with embedded tubing connected to a cooling bath pumping a 70/30 mixture of glycol to distilled water near  $-20^{\circ}\text{C}$ , rests on top

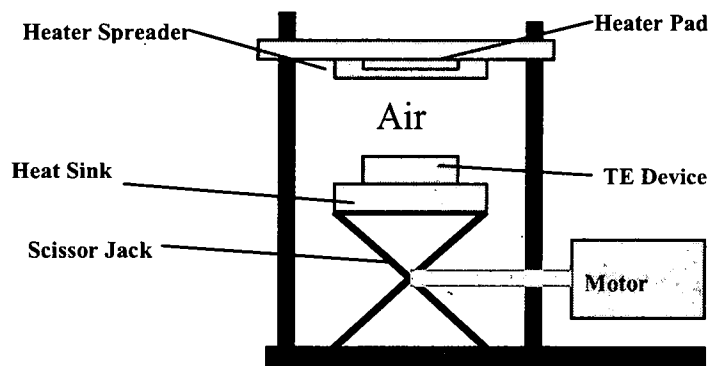


Figure 4.1: Variable air-gap experimental set-up schematic

of the scissor jack. To represent the thermal switch in the high thermal resistance state, the stepper motor drives the scissor jack down until a desired air gap distance of 8 mm is achieved. The 8 mm gap is chosen to minimize the heat transfer from the heat source and the TE device during open conditions. Distances greater than 8 mm show little heat transfer benefit, and distances below 8 mm have notably increased heat transfer. Thus the high thermal resistance state is associated with conduction, radiation, and convection across the air gap. To represent the thermal switch in the low thermal resistance setting, the stepper motor drives the scissor jack up until the TE device is firmly pressed against the heat source assembly. When closed, the low thermal resistance between the heater assembly and the TE device is dominated by the contact resistance between the TE device and heater spreader. Gentle pressure between heat source and TE device, achieved by application of a weight atop the "floating" heat source, ensures adequate thermal contact between the heater spreader and TE device [127].

The goal of this investigation is to determine the improvement of time averaged overall TE device power output to power input ratio for a waste heat recovery system with a thermal switch, and compare it to a similar system without a thermal switch. The power

ratio for the system ( $PR_{exp}$ ) is defined as the ratio of time averaged power generated by the TE device to the power into the system in the form of heat from the source as shown by equation 3.20. The power ratio improvement due to switching is given by the equation 4.1.

$$PR \text{ Improvement} = \frac{PR_{switching} - PR_{nc}}{PR_{nc}} \quad (4.1)$$

Experiments are conducted for both constant heat and variable heat input. For the constant heat input tests, once the circulator (heat sink) reaches a constant temperature, the silicon rubber heater pad (heat source,  $Q_{in}$ ) is set to a constant power setting to ensure that the source temperature with no thermal switching is  $119 \pm 1.0^\circ\text{C}$  at the low thermal resistance setting. The air gap is set to zero guaranteeing firm contact between the heater assembly and the TE device. In this condition, the system achieves steady state ( $\pm 0.1^\circ\text{C}$ ) prior to recording data to establish the system performance for no switching. Once this baseline is established, switching is employed by opening the air gap to a distance of 8 mm and monitoring the source temperature. Once the source temperature reaches  $160 \pm 1.0^\circ\text{C}$ , the gap is once again zeroed. When the source temperature reaches the lower bound, defined as  $T_s - \Delta T_s$ , the air gap is again set to 8 mm and the process is repeated. The output power from the TE device is sampled every one second and the overall power ratio, PR, is calculated.

The variable heat input test begins by determining the baseline, no control data set for a heat input described by equation 3.21. After the baseline is established, switching is employed as described above in the constant heat input test procedures. For both constant and variable heat input tests, all temperatures and voltages are recorded using an HP E1421B data acquisition system and are sampled every second. All results presented in this chapter are from a single run with the described inputs.

## 4.2 Experimental Results

### 4.2.1 Constant Heat Input

For the constant heat input tests, the ratio between the maximum source temperature for switching and the steady-state source temperature (no switching) is maintained at 1.333 in degrees Celsius by adjusting the heat input to the system. This ratio is set to mirror a safety factor built into design of a thermal management system. The thermal resistances, capacitances, temperatures and thermoelectric properties are kept constant throughout the constant heat source test as summarized in Table 4.1. Three source thermal capacitances are tested to determine the effects of source thermal capacitance on power ratio improvements. For each source capacitance tested, several different source temperature ranges,  $T_{s,max} < T_s < T_{s,max} - \Delta T_s$ , are considered in an effort to find the best range of permissible source temperatures which results in the greatest output power ratio for energy harvested. The mounting resistance,  $R_{mounting}$ , of the TE device is determined experimentally and includes the epoxy and ceramic plates used to mount the TE device to the experimental set-up and contact resistance.

Fig. 4.2 shows a plot of output power ratio improvement as a function of source temperature for the three source capacitances tested. As seen in the figure, an optimal  $\Delta T_s$  exists for each source capacitance considered. If the  $\Delta T_s$  value is too small, the time that the source is in contact with the TE device and energy is being harvested,  $t_{on}$ , is small in comparison to the time the source is not in contact with the TE device (no energy harvested),  $t_{off}$ , as seen in Fig. 4.3. If  $\Delta T_s$  is too large, the source temperature drops to the point of degrading the output power of the TE device, as is observable in Fig. 4.4.

Table 4.2 shows the results for the optimal  $\Delta T_s$  for each source capacitance tested. As the source thermal capacitance increases relative to the TE device thermal capacitance, the output power ratio improvement increases as previously observed in the analytical

Table 4.1: Physical and spatial variables that remain fixed for all constant heat input experimental cases studied.

Variable	Value
$C_{TE}$	25 J/K
$R_{TE}$	2.5 K/W
$T_{s,steady}$	119°C
$T_{s,max}$	160°C
$T_{sink}$	-18.5°C
$R_{p,on}$	1.75 K/W
$R_{p,off}$	120 K/W
$C_{sink}$	$\sim \infty$ J/K
$R_{sink}$	$\sim 0$ K/W
$R_{mounting}$	4.39 K/W
ZT	1

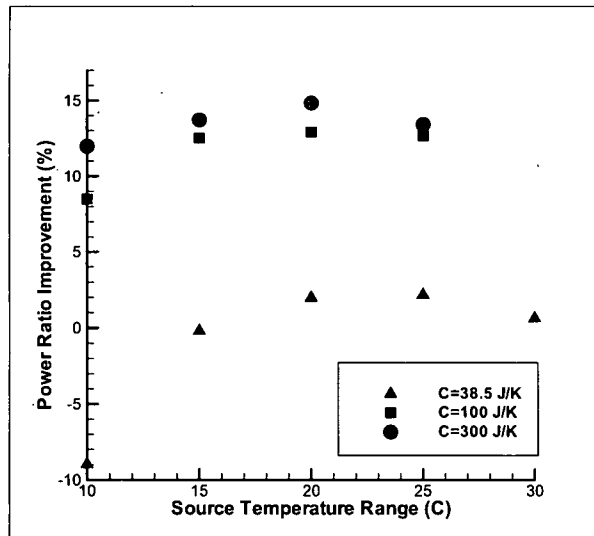


Figure 4.2: Power output ratio improvements for constant heat input and  $C_s = 38.5$ , 100, and 300 J/K as a function of  $\Delta T_s$ .



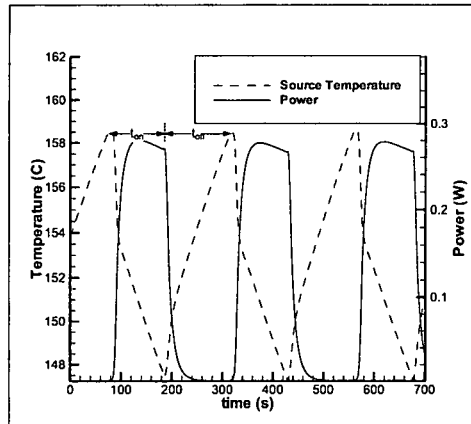


Figure 4.3: Source temperature and TE output power with  $C_s = 100\text{J/K}$ , and  $\Delta T_s = 10^\circ$ .

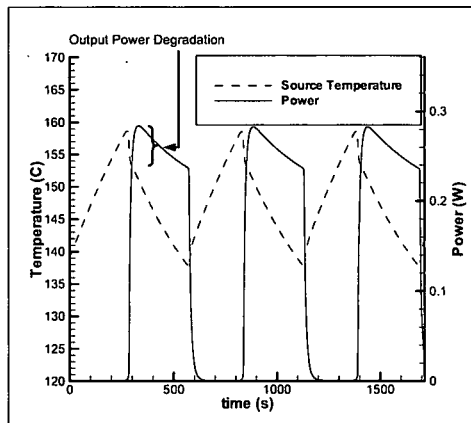


Figure 4.4: Source temperature and TE output power with  $C_s = 100\text{J/K}$ , and  $\Delta T_s = 25^\circ$

Table 4.2: Summary of the optimal experimental power output ratio improvements for constant heat input and variable source capacitance

Case	1	2	3
$Q_{in}(W)$	27	27	32.7
$C_s(J/K)$	38.5	100	300
$\Delta T_s(^{\circ}C)$	25	20	20
$\frac{t_{on}}{t_{off}}$	1.01	1.07	1.01
$PR_{nc}(\%)$	$1.2 \pm 0.32$	$1.4 \pm 0.32$	$1.7 \pm 0.32$
$MaxPR_{switching}(\%)$	$1.2 \pm 0.32$	$1.6 \pm 0.32$	$1.9 \pm 0.32$
$PR_{Improvement}(\%)$	$2.2 \pm 0.95$	$12.9 \pm 0.95$	$14.8 \pm 0.95$

model. Larger source capacitances allow the source to store more thermal energy when the thermal switch resistance is high. When the thermal switch resistance is low, more thermal energy is forced through the system. When the thermal capacitance of the TE device is small in comparison to the source, relatively little energy is stored in the TE device, and thus the heat dissipates from the TE device when the thermal switch is off (at lower average temperature differences) is relatively small. The ratio of source contact time with the TE device,  $t_{on}$ , divided by time the source is not in contact with the TE device,  $t_{off}$ , at optimal  $\Delta T_s$  conditions is given as  $t_{on}/t_{off}$ . In all cases for the experiments conducted, the optimal on time versus off time ratio is about 1. This result is not a general rule, but a function of the experimental conditions. Experimental uncertainty of time-averaged power ratio improvement for the system is determined to be 0.96%. Also from Table 4.2, the power ratios for both the no control and switching cases are extremely low, on the order of 1 to 2 %. Though these measured values are low, they are calculated from voltages and currents that range from 0.05 to 1.4 Volts and 0.01 to 0.3 Amps respectively, well within the resolution of the measurement instruments.

#### 4.2.2 Variable Heat Input

For the variable heat input tests, the heat source capacitance is constant for all cases but the sinusoidal heat source input frequency is varied. Table 4.3 shows the fixed thermal resistances, capacitances, temperatures and thermoelectric properties for these tests. The frequency is changed from 0.003 Hz to 0.0003 Hz in order to better understand the effects of heat input frequency on power ratio improvements.

To find the optimal output power ratio at each thermal load frequency,  $\Delta T_s$  is varied until a maximum power improvement ratio is determined. As can be seen from Table 4.4, as the frequency decreases, the maximum source temperature without control,  $T_{s,max,nc}$ , increases. Additionally, the output power ratio improvement is best in Case 2 for a frequency of 0.000556 Hz and  $\Delta T_s=20^\circ\text{C}$ . In Case 1, the high frequency heat input prevents the heat source from fully reaching its maximum value, therefore the power ratio improvement is degraded. In Case 3, the frequency is low enough that the non-negligible energy stored in the TE device is lost during open switch conditions. This heat dissipation from the TE device during this period is associated with an effectively low temperature drop across the TE device, thus degrading the time-averaged power ratio improvement. One can conclude that the optimal frequency for energy harvesting for transient heat input would depend on the thermal capacitances of the source, TE device, and the sink. If the thermal capacitance of the TE device is negligible, lower frequencies should produce more beneficial results with thermal switching.

#### 4.3 Capacitance Effects

For constant heat input, it is noticed that as the source thermal capacitance increases at constant TE thermal capacitance, the output power ratio increases for both the experiment and finite difference simulation, as seen in Tables 3.14 and 4.2. To fur-

Table 4.3: Physical and spatial variables that remain fixed for all variable heat input experimental cases studied.

Variable	Value
$Q_{\max}$	44 W
$C_s$	100 J/K
$C_{TE}$	25 J/K
$R_{TE}$	2.5 K/W
$T_{s,\max}$	$160^\circ \pm 1.0C$
$T_{\text{sink}}$	$-18.5^\circ \pm 1.0C$
$R_{P,\text{ON}}$	1.75 K/W
$R_{P,\text{OFF}}$	120 K/W
$C_{\text{sink}}$	$\sim \infty$ J/K
$R_{\text{sink}}$	$\sim 0$ K/W
$R_{\text{mounting}}$	4.39 K/W
ZT	1

Table 4.4: Summary of the optimal experimental power output ratio improvements for variable heat input and variable source capacitance

Case	1	2	3
$f(\text{Hz})$	0.00333	0.00056	0.00028
$T_{s,\max,\text{nc}}(^{\circ}\text{C})$	102	130.6	150.8
$\Delta T_{s,\text{opt}}(^{\circ}\text{C})$	20	20	30
$\frac{t_{\text{on}}}{t_{\text{off}}}$	0.472	0.517	0.630
$\text{AvePR}_{\text{nc}}(\%)$	$1.3 \pm 0.32$	$1.4 \pm 0.32$	$1.4 \pm 0.32$
$\text{MaxPR}_{\text{switching}}(\%)$	$1.6 \pm 0.32$	$1.8 \pm 0.32$	$1.8 \pm 0.32$
$\text{PRImprovement}(\%)$	$20.0 \pm 0.95$	$30.0 \pm 0.95$	$25.8 \pm 0.95$

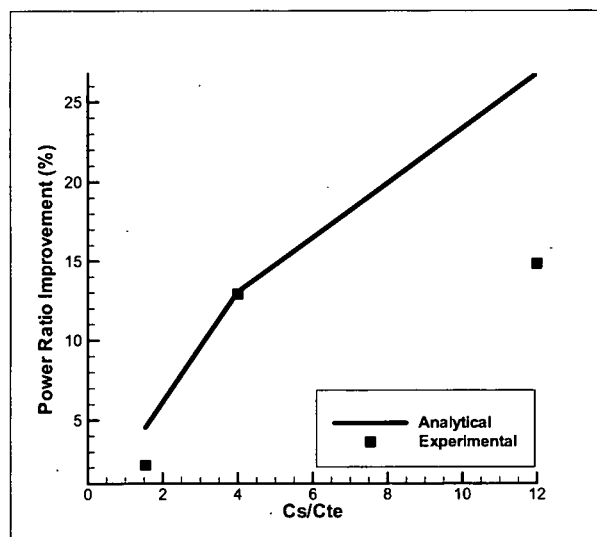


Figure 4.5: Finite difference model and experimental power output ratio improvements as a function of thermal capacitance ratio

ther investigate this phenomenon, the effect of different capacitance ratios, defined as the source thermal capacitance divided by the TE device thermal capacitance, on power output ratio is investigated both analytically and experimentally. As seen in Fig. 4.5, increasing the capacitance ratio increases the output power ratio of the system with thermal switch control. Notably, when the thermal capacitance of the TE device is greater than the source, controlled thermal switching has no beneficial effect. For this case, heat transfer to the TE device causes significant thermal energy storage in the TE device. Thus, when the thermal resistance of the thermal switch is high, the thermal energy storage in the TE device is released at a smaller effective temperature drop across the device thus reducing overall performance. Therefore the source thermal capacitance must be greater than the TE device thermal capacitance in order for thermal switching to be beneficial in waste heat recovery systems. This high thermal capacitance ratio can be realized in practice with thin-film superlattice TE devices.

#### **4.4 Comparison Between Analytical Model and Variable Air-Gap Experiment**

A plot of the source temperature and TE output power for the finite difference model with constant heat input is shown in Fig. 4.6. A similar plot with the experimental data is shown in Fig. 4.7. These plots for both the finite difference model and experiment for comparable input parameters are very similar. In fact, both the analytical model and experiment require a heat input of 32.7 W to achieve the required steady-state temperature of 119°C in the low thermal resistance setting. The finite difference model shows a maximum power ratio of 0.7%, with overall power improvement ratios increased by 26.8%. The maximum power ratio of the experimental system is 1.9%, with overall power improvement ratios increased by 14.8%. The greatest difference between the analytical and experimental results is at the highest source capacitance, where heat losses to the environment are largest and

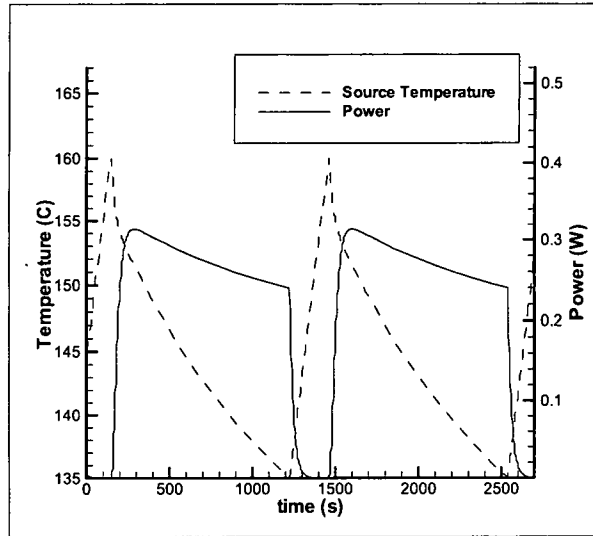


Figure 4.6: Finite difference results for constant heat input for  $Q_{in} = 32.7\text{W}$ ,  $C_s = 300\text{J/K}$ , and  $T_{s,max} = 160^\circ\text{C}$ .

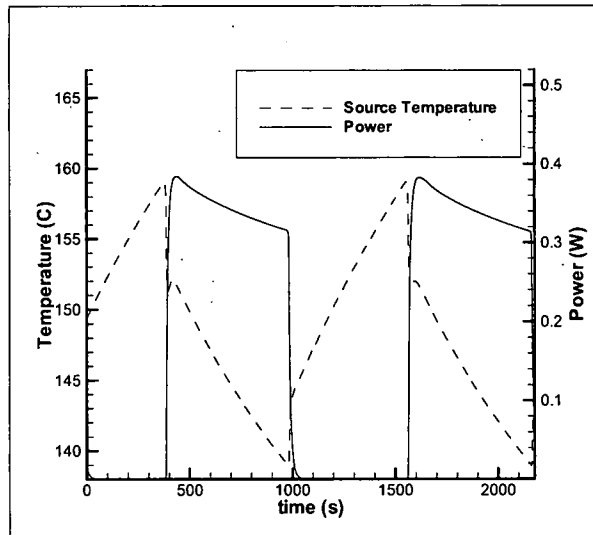


Figure 4.7: Experimental results for constant heat input for  $Q_{in} = 32.7\text{W}$ ,  $C_s = 300\text{J/K}$ , and  $T_{s,max} = 160^\circ\text{C}$ .

not accounted for in the analytical model. Thus the analytical results overestimate the experimental measurements.

#### **4.5 Projected Results for State of the Art TE Device**

While the experimental improvements are notable, the overall power ratios are still low because of the mounting resistance of the TE used in the experiment. In order to better understand the effects of thermal switching for waste heat recovery systems with state-of-the-art TE devices, results for a state-of-the-art TE device are projected using the experimentally verified analytical model. For a waste heat recovery system operating at a maximum source temperature of  $160^{\circ}\text{C}$ , a source capacitance of  $100\text{ J/K}$ , a TE capacitance of  $1\text{ J/K}$ , a  $ZT$  of 3, and minimal mounting resistance and heat loss, the overall power output ratio improves to more than 35% with a thermal switch as predicted by the finite difference model.

The experimental and analytical results provided in these chapters proved that thermal switching can improve the performance of waste heat recovery systems. Also, the source thermal capacitance must be greater than the thermal capacitance of the TE device for thermal switching to improve output power recovered from a waste heat recovery system. Additionally, the experimental results verified the effectiveness of the analytical finite difference model described in Ch. 3. Finally, the analytical model predicted that thermal switching could boost a state-of-the-art waste heat recovery system output power ratio by 35% for constant heat input in certain design space conditions.



## Chapter 5

### Thermal Switch Designs Exploration

With the feasibility of augmenting TE energy harvesting via thermal switching verified analytically and experimentally, a realistic design is investigated. To attack this problem, several candidate solutions are identified and analytically explored. The first two candidate designs are based on Micro-Electrical-Mechanical systems (MEMS). The first design utilizes horizontal bimaterial beams, and the second uses vertical bimaterial beams. Both MEMS designs rely on bending caused by residual stress within the beam structure due to the mismatch of thermal expansion coefficients. As the temperature of the beams increases, the bending decreases allowing the beams to make thermal contact between the heat source and the TE device. The third design utilizes wax wells, in which the wax is imbedded with carbon nano particles to increase the thermal conductivity. As the temperature of the wax increases, the wax swells and makes thermal contact between the heat source and the TE device. The final design utilizes a micro heat pipe concept, in which each heat pipe consists of a chamber filled with saturated liquid and vapor. As the temperature increases inside the chamber, the liquid starts to evaporate and the vapor begins to condense allowing heat to transfer much more effectively from the heat source to the TE device. All four designs are compared using common metrics including switching ratio defined as the ratio of thermal resistance in the high and low state, required actuation energy, mass to actuation energy ratio, maximum heat flow through the device, and entropy

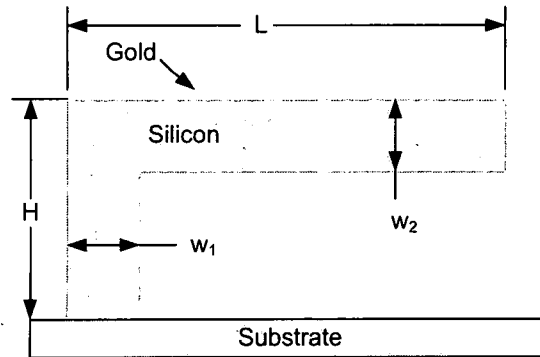


Figure 5.1: Front view of horizontal MEMS bimaterial beam.

generated for one switching period. Both the horizontal MEMS beams and the micro heat pipe design are fabricated, and only the micro heat pipe design is tested.

## 5.1 Horizontal Micro-Electrical-Mechanical System

The first thermal switch design considered is the horizontal bimaterial beam array using a MEMS fabrication process. Each beam consists of a polysilicon post with a cantilevered beam made of polysilicon and a thin layer of gold as shown in Fig. 5.1. The polysilicon and gold layers have different coefficients of thermal expansion resulting in lateral motion when the assembly is heated [128].

To utilize this bimaterial beam array as a thermal switch, the beam must make thermal contact between the heat source and heat sink at a prescribed temperature. The PolyMUMPS [129] process is used to design an array of horizontal polysilicon cantilevered beams of thickness,  $1.5 \mu\text{m}$ , length,  $100 \mu\text{m}$ , and various widths, with a  $0.5 \mu\text{m}$  layer of gold on top, shown in Fig. 5.1. When the thermal switch is in the off position (minimal heat is allowed to flow through the switch), the cantilevered beam is not in contact with either the heat source or the TE device. The length of the beam is determined with this constraint in mind. Assuming the poly 2 layer is used to create the beam, and gold is used to create

the top layer of the beam, the length is such that the tip does not extend beyond the height of the post structure of length  $d$ . The distance is defined to be:

$$d = \frac{L^2}{2R} \quad (5.1)$$

where  $R$  is the radius of curvature of the beam is defined by equation 5.2,

$$R = \frac{(t_1 + t_2)^3}{6t_1t_2(\alpha_2 - \alpha_1)\Delta T} \quad (5.2)$$

Here  $\alpha$  is the coefficient of thermal expansion of material 1 and 2,  $t$  is the thickness of material 1 and 2, and  $\Delta T$  is the temperature difference between the deposition temperature and actual temperature [130].

For a residual stress thermal switch made in the PolyMUMPS process for the proposed design, the distance between the substrate and the horizontal beams is  $2.5\mu\text{m}$ . By using equations 5.1 and 5.2, the length of the beam is determined to be  $100\mu\text{m}$  to prevent the beam from extending past the top surface of the post structure when the structure is released. Now that the length of the beam is defined, the performance of the thermal switch is modeled using the design constants and material constants shown in Table 5.1.

Equations 5.1 and 5.2 are used to develop a relationship between ambient temperature and deflection of the tip of the beam as shown in Fig. 5.2.

From this figure, it is seen that the residual stress thermal switch is in its "off" state, or in other words, the only heat flowing through the switch is conduction through the posts, between  $30^\circ\text{C}$  and  $180^\circ\text{C}$ . The cantilevered beam is not extending beyond the post in this temperature range. The thermal switch is in its "on" state beyond  $180^\circ\text{C}$ . This means that when the beam makes contact with the source heat flows through the beam and the post, thus decreasing the thermal resistance of the device.

For a beam with a length of  $100\mu\text{m}$ , width of  $10\mu\text{m}$ , a silicon thickness of  $1.5\mu\text{m}$ , and a layer of gold on top of thickness  $0.5\mu\text{m}$ , as seen in Figure 5.2, a deflection of  $3\mu\text{m}$

Table 5.1: Physical parameters for MEMS horizontal residual stress beams.

Variable	Description	Value
$t_1$	Thickness of Si	$1.5 \mu\text{m}$
$\alpha_1$	Thermal expansion coef. of Si	$2.33 \mu\text{m/mK}$
$t_2$	Thickness of gold	$0.5 \mu\text{m}$
$\alpha_2$	Thermal expansion coef. of gold	$14.2 \mu\text{m/mK}$
$T_0$	Deposition temperature	$100^\circ\text{C}$
$L$	Length of beam	$100 \mu\text{m}$
$H$	Height of post	$4.25 \mu\text{m}$
$\delta$	Thickness of gold	$0.5 \mu\text{m}$
$K_{\text{Si}}$	Thermal conductivity of Si	$168 \text{ W/mK}$
$K_{\text{g}}$	Thermal conductivity of gold	$319 \text{ W/mK}$
$w_1$	Width of Si	$10 \mu\text{m}$
$w_2$	Width of gold	$1.5 \mu\text{m}$
$\rho_{\text{Si}}$	Density of Si	$2330 \text{ kg/m}^3$
$C_{\text{Si}}$	Thermal capacitance of Si	$678 \text{ J/kgK}$

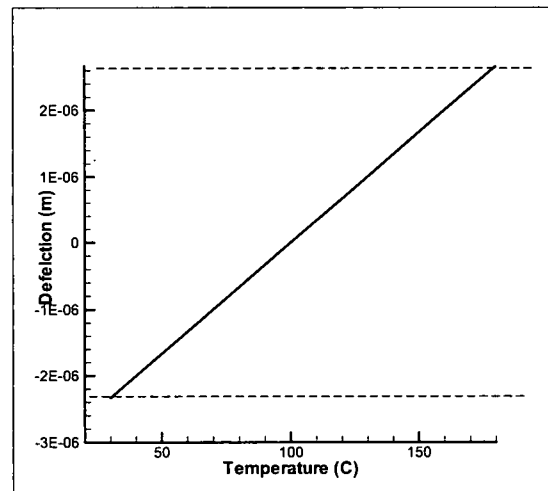


Figure 5.2: Plot of ambient temperature versus deflection of the tip of the residual stress thermal switch.

is realized at a temperature of 180°C. At this temperature and deflection, the horizontal beam makes thermal contact with the heat source.

To estimate the thermal switching resistance ratio, or the thermal resistance of the switch in its 'off' state divided by the thermal resistance in its 'on' state, it is assumed that the entire horizontal beam makes thermal contact with the heat source. Therefore the thermal resistance of the switch in the 'on' state is estimated by equation 5.3.

$$R_{on} = \frac{H - w_2}{K_{Si}w_1w_2} + \frac{\delta}{K_gLw_3} + \frac{w_2}{K_{Si}Lw_3} \quad (5.3)$$

where  $\delta$  represents the thickness of the gold layer, and  $w_3$  represents the width of the thermal switch.

The thermal resistance of the switch in the 'off' state, assuming that heat conducts through the silicon and gold post, is estimated as shown in equation 5.4.

$$R_{off} = \frac{H}{K_{Si}w_1w_3} + \frac{\delta}{K_gLw_3} \quad (5.4)$$

Equation 5.5 shows that the estimated thermal switching resistance ratio for one horizontal MEMS residual stress beam is approximately 1.5. Recognize that this does not represent a maximum value by any means.

$$\text{Ratio} = \frac{R_{off}}{R_{on}} = \frac{(HK_g + \delta K_{Si})L}{HLK_g - LK_gw_2 + (\delta K_{Si} + K_gw_2)w_1} = 1.5 \quad (5.5)$$

To find the energy required per area and mass to actuation energy ratio to actuate a MEMS horizontal thermal switch, the mass is estimated assuming that the entire structure is silicon, e.g. the amount of gold is minimal. The energy for actuation is assumed equal to the amount of energy needed to raise the temperature of the cantilever system from -20°C to 180°C.

$$V = w_1(H - w_2)w_3 + Lw_2w_3 + m_{connect}$$

$$m = V\rho = 7.63e - 12m$$

$$\begin{aligned}
A &= (L + w_1)(w_3 + w_1) = 2.2e - 9 \text{m}^2 \\
Q_{in} &= mC_{Si}\Delta T = 1.03e - 6 \text{J} \\
\frac{Q_{in}}{A} &= 470.3 \frac{\text{J}}{\text{m}^2} \\
\frac{m/Q_{in}}{A} &= 3352 \frac{\text{kg}}{\text{Jm}^2}
\end{aligned}$$

Here  $m_{\text{connect}}$  is the mass of the silicon that connected the horizontal beam together.

To estimate the maximum heat flow through the device, the 'on' state thermal resistance is used [131].

$$Q_{\text{max}} = \frac{\Delta T}{R_{\text{on}}} = \frac{180 - -20^\circ\text{C}}{174.186 \frac{\text{K}}{\text{W}}} = 1.15 \text{W} \quad (5.6)$$

The associated maximum heat flux is  $5.2e8 \text{W/m}^2$  assuming heat transfer area equal to the footprint of the cantilever.

Another metric to compare possible thermal switch designs is entropy generated per cycle because lower entropy generated indicates a more robust design. There are 3 states of operation of the horizontal beam switch. First is when the beam is open and closing, heat flows into the silicon post from the source. The entropy generated during this time period, assuming the period of operation is 30 seconds per cycle, is shown in equation 5.7.

$$S_{\text{gen}} = \frac{Q_{in}\Delta t}{T_s} = 2.45e - 9 \text{J/K} \quad (5.7)$$

The second term includes the heat flowing through the switch in the 'on' state and is described by equation 5.8.

$$S_{\text{gen}} = Q_{\text{max}}\Delta t \left( \frac{1}{T_s} + \frac{1}{T_{\text{sink}}} \right) = 0.18 \text{J/K} \quad (5.8)$$

The third terms describes the entropy generated as the switch opens and heat flows from the switch to the sink as shown in equation 5.9.

$$S_{\text{gen}} = \frac{Q_{in}\Delta t}{T_{\text{sink}}} = 4.09e - 9 \text{J/K} \quad (5.9)$$

The entropy generated during the actuation of the switch is the addition of the entropy during the opening and closing of the switch shown in equations 5.7 and 5.9 respectively. The total entropy generated due to the actuation of the thermal switch normalized by area is described in equation 5.9.

$$\frac{S_{\text{gen}}}{A} = \frac{2.45\text{e} - 9 + 4.09\text{e} - 9 \frac{\text{J}}{\text{K}}}{2.2\text{e} - 9 \text{ m}^2} = 4.09\text{e} - 9 \text{ J/K} \quad (5.10)$$

The horizontal MEMS beam array was fabricated and a photograph is shown in Fig. 5.3

## 5.2 Vertical Micro-Electrical-Mechanical System

Another MEMS inspired design concept is an array of vertical bi-material beams, shown in Fig. 5.4a. Deep reactive ion etching can be used to create high aspect ratio trenches in the bulk material, and a highly conformal metal can be deposited on one side of the beam [128]. Deposition takes place at an elevated temperature, so when the structure is released, it will bend. This design utilizes a silicon substrate and a thin film of gold to construct the bimaterial beams. To ensure proper thermal contact between the heat source and the thermal switch, the heat source is pressed against the vertical beams such that the beams are slightly curved as shown in Fig. 5.4b. As the temperature of the thermal switch increases, the beams curl and the radius of curvature decreases. Because the beams are enclosed within a gap of height  $G$ , the beams will only start to move when the radius of curvature is less than  $R_0$ . This is called the 'switch-off' temperature.

The parameters used to design the MEMS vertical bimaterial beams such as length and thickness are described in Table 5.2. The radius of curvature of the bimaterial beam is described by equation 5.2. The gap height,  $G$ , is described by equation 5.11.

$$G = R_0 \sin\left(\frac{1}{R_0}\right) = 998\mu\text{m} \quad (5.11)$$

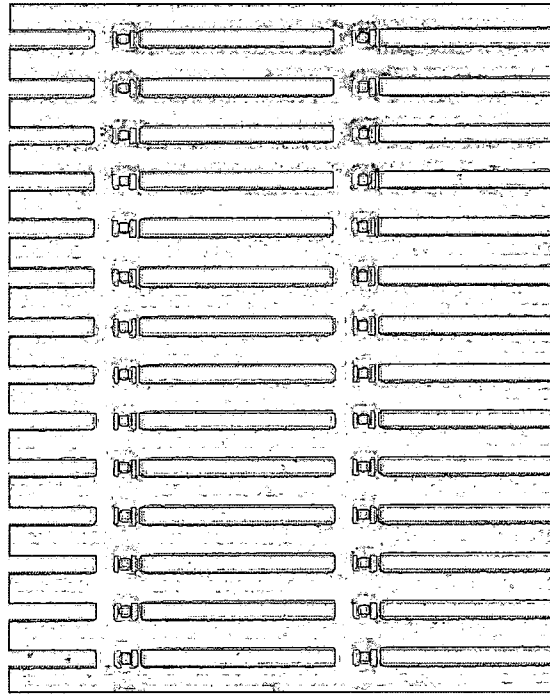


Figure 5.3: Photograph of fabricated horizontal MEMS bimaterial beam design.

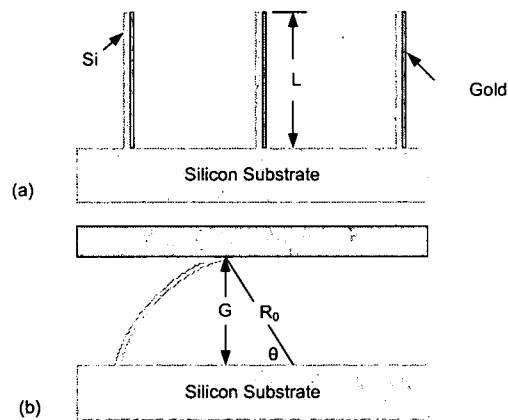


Figure 5.4: Front view of vertical MEMS bimaterial beam.



Table 5.2: Physical parameters for MEMS vertical residual stress beams.

Variable	Description	Value
$t_1$	Thickness of Si	$10\ \mu\text{m}$
$\alpha_1$	Thermal expansion coef. of Si	$2.6\ \mu\text{m/mK}$
$t_2$	Thickness of gold	$2\ \mu\text{m}$
$\alpha_2$	Thermal expansion of gold	$14\ \mu\text{m/mK}$
$T_{\text{deposit}}$	Deposition temperature	$20\ ^\circ\text{C}$
$T_{\text{switch}}$	Switching temperature	$150\ ^\circ\text{C}$
$T_{\text{TE}}$	TE device temperature	$-20\ ^\circ\text{C}$
$L$	Length of beam	$0.001\ \text{m}$
$\varepsilon$	Emissivity	$0.5$
$s$	Space between vertical beams	$5\ \mu\text{m}$
$K_{\text{Si}}$	Thermal conductivity of Si	$168\ \text{W/mK}$
$\rho_{\text{Si}}$	Density of Si	$2330\ \text{kg/m}^3$
$C_{\text{Si}}$	Thermal capacitance of Si	$678\ \text{J/kgK}$

When the switch is in the 'off' position, most of the heat transfer is due to radiation and is estimated by equation 5.12.

$$\begin{aligned} h_r &= \sigma \varepsilon (T_s^2 + T_{TE}^2) (T_s + T_{TE}) \\ A &= s + t_1 m^2 \\ R_{off} &= \frac{1}{h_r A} \\ R_{off} &= \frac{1}{h_r (s + t_1)} \end{aligned} \quad (5.12)$$

When the switch is in the 'on' position, heat conducts through the silicon of width  $t$  and length  $L$  and is described by equation 5.13.

$$R_{on} = \frac{L}{K_{Si} t_1^2} \quad (5.13)$$

Using equations 5.12 and 5.13 and the parameters in Table 5.2, the thermal resistance ratio is given by equation 5.14.

$$\text{Ratio} = \frac{R_{off}}{R_{on}} = 16,020 \quad (5.14)$$

The volume, mass, cross-sectional area, and heat stored in the switch (presumed to be the actuation energy) are described by the following equations.

$$\begin{aligned} V &= t_1^2 L + (s + t_1)^2 \\ m &= V \rho = 2.38e - 10 \text{ m} \\ A &= s + t_1 = 15e - 6 \text{ m}^2 \\ Q_{in} &= m C_{Si} \Delta T = 27.6e - 6 \text{ J} \end{aligned}$$

The actuation energy per area and mass to actuation energy ratio are calculated using the following equations.

$$\frac{Q_{in}}{A} = 190.4 \frac{\text{J}}{\text{m}^2}$$

$$\frac{m/Q_{in}}{A} = 1.83 \frac{\text{kg}}{\text{Jm}^2}$$

The maximum heat flow through the switch is approximated by equation 5.15

$$Q_{max} = \frac{\Delta T}{R_{on}} = \frac{150 - -20^\circ\text{C}}{59.5\text{e}3 \frac{\text{K}}{\text{W}}} = 0.0029 \text{ W} \quad (5.15)$$

Again entropy generated is calculated for the 3 states of operation of the vertical MEMS beam similar to the horizontal beam. First, when the switch is in the 'off' state and is closing, heat flows into the silicon post from the source. The entropy generated during this time period, assuming the period of operation is 30 seconds per cycle, is shown in equation 5.7.

$$S_{gen} = \frac{Q_{in}\Delta t}{T_s} = 6.49\text{e} - 8 \text{ J/K} \quad (5.16)$$

The second term includes the heat flowing through the switch in the 'on' state and is described by equation 5.17.

$$S_{gen} = Q_{max}\Delta t \left( \frac{1}{T_s} \right) + \frac{1}{T_{sink}} = 0.00054 \text{ J/K} \quad (5.17)$$

The third terms describes the entropy generated as the switch opened and heat flows from the switch to the sink as shown in equation 5.9.

$$S_{gen} = \frac{Q_{in}\Delta t}{T_{sink}} = 1.08\text{e} - 7 \text{ J/K} \quad (5.18)$$

The entropy generated to the actuation of the switch is the addition of the entropy during the opening and closing of the switch shown in equations 5.16 and 5.18 respectively. The total entropy generated due to the actuation of the thermal switch normalized by cantilever footprint area is described in equation 5.18.

$$\frac{S_{gen}}{A} = \frac{6.49\text{e} - 8 + 1.08\text{e} - 7 \frac{\text{J}}{\text{K}}}{15\text{e} - 6 \text{ m}^2} = 0.012 \text{ J/K} \quad (5.19)$$

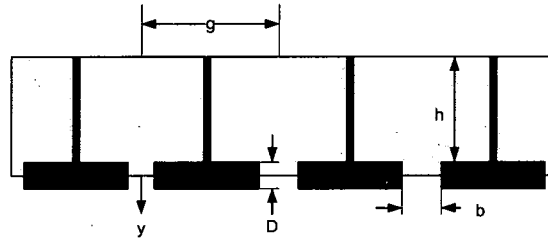


Figure 5.5: Schematic of wax well thermal switch.

### 5.3 Wax-Filled Wells

The third design considered is an array of wells filled with carbon fiber filled wax. In this concept, the majority of the wax is contained within the wells. As the wax melts, it expands and starts to flow down into narrow channels or fingers amplifying the expansion of the wax as shown in Fig. 5.5.

To analyze the temperature distribution in this melting problem, a simplified 1-D conduction solution from Ozisik is employed [116]. It is assumed that initially the temperature of the wax is at its melting temperature,  $T_m$ , but all the wax is solid. The temperature along the top edge is assumed to be  $T_f$  and the temperature at the bottom edge is  $T_a$  as shown in Fig. 5.6. Because the well width is much wider than the height,  $g \gg h$ , the temperature distribution is estimated employing a 1-D conduction solution in the  $y$  direction. The solid ribs of cells are relatively thin and do not contribute to the overall heat conduction and are therefore neglected. The wax and carbon fibers are assumed to be homogeneously mixed therefore assumed to have effective properties throughout the wax. The 1-D heat conduction problem with a single phase and constant density is solved utilizing the integral method. For the top liquid wax portion,  $0 < y < S_f(t)$ , and  $t > 0$ , the governing differential equation is given by equation 5.20.

$$\frac{\partial^2 T_{l1}}{\partial y^2} = \frac{1}{\alpha_l} \frac{\partial T_{l1}(y,t)}{\partial t} \quad (5.20)$$

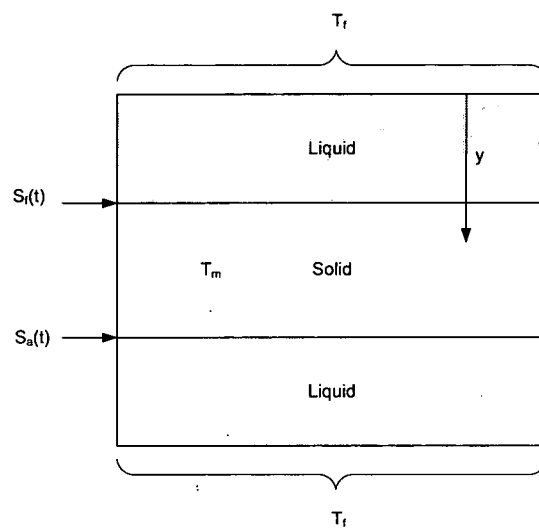


Figure 5.6: Simplified 1-D conduction boundary condition

where  $T_{l1}$  represents the temperature of the top liquid portion of the wax, and  $\alpha_1 = k/c_p\rho$ . For the solid wax portion,  $S_f(t) < y < S_a(t)$ , and  $t > 0$ , the governing differential equation is equation 5.21.

$$\frac{\partial^2 T_s}{\partial y^2} = \frac{1}{\alpha_1} \frac{\partial T_s(y, t)}{\partial t} \quad (5.21)$$

where  $T_s$  represents the temperature of the solid portion of the wax. Finally, for the bottom liquid portion,  $S_a(t) < y$ , and  $t > 0$ , the governing differential equation is equation 5.22.

$$\frac{\partial^2 T_{l2}}{\partial y^2} = \frac{1}{\alpha_2} \frac{\partial T_{l2}(y, t)}{\partial t} \quad (5.22)$$

where  $T_{l2}$  represents the temperature of the liquid wax on the bottom of the well.

At the top boundary, or  $y = 0$ , the temperature is equal to  $T_0$ . For the interfaces, or  $y = S(t)$ , the temperature is equal to  $T_m$ , and an energy balance of the interface boundary lead to the equation 5.23.

$$-k_l \frac{\partial T_{l1}}{\partial y} = \rho L \frac{dS(t)}{dt} \quad (5.23)$$

where  $L$  represents the energy per mass required to melt all of the wax.

The solution for the temperature distribution is given by equation 5.24.

$$T(y, t) = T_m + b_1(y - S) + c_1(y - S)^2 \quad (5.24)$$

Where,

$$\begin{aligned} b_1 &= \frac{\alpha \rho L}{kS} \left( 1 - (1 + \mu)^{1/2} \right) \\ c_1 &= \frac{b_1 S + (T_0 - T_m)}{S^2} \\ \mu &= \frac{2k}{\alpha \rho L} (T_0 - T_m) \end{aligned}$$

Substituting the temperature profile into the energy-integral equation, the differential equation describing the solid-line interface is evaluated to be as shown in equation 5.25.

$$A \frac{dS}{dt} = 6\alpha \frac{1 - (1 + \mu)^{1/2} + \mu}{5 + (1 + \mu)^{1/2} + \mu} \quad (5.25)$$

with  $S = 0$  at  $t = 0$ .

The solution to this differential equation for the leading and trailing interfacial fronts is given by equations 5.26.

$$S_f(t) = S_a(t) = 2 \left( 3 \frac{1 - (1 + \mu)^{1/2} + \mu}{5 + (1 + \mu)^{1/2} + \mu} \right)^{1/2} \sqrt{\alpha t} \quad (5.26)$$

The temperatures at the top and bottom boundaries,  $T_f$  at  $y = 0$  and  $T_a$  at  $y = h$ , are assumed to be above the melting temperature. Given that the interfacial movement from the top edge down and bottom edge up is respectively represented by  $S_f(t)$  and  $S_a(t)$ , when these two interfaces meet is when all of the wax is melted. The wax well height,  $h$ , represents the total height of the wax well and therefore the addition of the location of the top interface and the bottom interface as shown in equation 5.27.

$$h = S_f(t) + S_a(t) \quad (5.27)$$

The volume of one well is  $V_{\text{cell}} = hg$ . The mass of the solid wax must be equal to the mass of the melted liquid,  $\rho_s hg = \rho_l(hg + bD)$ . Combining these two equations and solving for  $h$  yields equation 5.28.

$$h = \frac{bD}{g(\rho_s/\rho_l - 1)} \quad (5.28)$$

To define the resistance ratio, the thermal resistance of the 'on' state is estimated to be conduction through the wax well, the wax finger, and air surrounding the finger, and is shown in equation 5.29.

$$R_{\text{on}} = \frac{D}{k_{\text{air}}(g - b) + k_{\text{wax}}b} \quad (5.29)$$

The thermal resistance in the 'off' state, assuming wax only fills the chamber of height  $h$  and air fills the finger of height  $D$ , is calculated using conduction through the wax well and through the air and is given by equation 5.30.

$$R_{\text{on}} = \frac{D}{k_{\text{air}}g} \quad (5.30)$$

Table 5.3: Physical parameters for wax wells.

Variable	Description	Value
$k_{air}$	Thermal conductivity of air	26.3 e-3 W/mK
$k_{wax}$	Thermal conductivity of the wax	100 W/mK
$T_f$	Temperature of top surface of wax	423 K
$T_a$	Melting temperature of wax	383 K
$T_m$	Temperature of bottom surface of wax	373 K
$\rho_s$	Density of solid wax	920 kg/m <sup>2</sup>
$\rho_l$	Density of liquid wax	740 kg/m <sup>2</sup>
$C_{p,wax}$	Specific heat of wax	2890 J/kgk
Ratio	Switching ratio	1000

Using equations 5.29 and 5.30, the thermal resistance ratio is given by equation 5.31.

$$\text{Ratio} = \frac{R_{off}}{R_{on}} = \frac{k_{air}(g - b) + k_{wax}b}{k_{air}g} \quad (5.31)$$

Table 5.3 defines the physical parameters to evaluate this design. Using parameters from Table 5.3 and equations 5.27 to 5.31, values for height of channel, height of wax wells, and width of wax wells are calculated.

$$D = 0.000237 \text{ m}$$

$$h = 0.000256 \text{ m}$$

$$g = (3.8b) \text{ m}$$

With these parameters defined, the switching ratio is calculated to be 1000, and the actuation energy per area is calculated using equation 5.32.

$$\frac{Q_{in}}{A} = \frac{m_{wax}C_{p,wax}\Delta T}{A} = 780e3 \frac{\text{J}}{\text{m}^2} \quad (5.32)$$

The mass to actuation energy is calculated using equation 5.33.

$$\frac{m/Q_{in}}{A} = 6065 \frac{\text{kg}}{\text{Jm}^2} \quad (5.33)$$



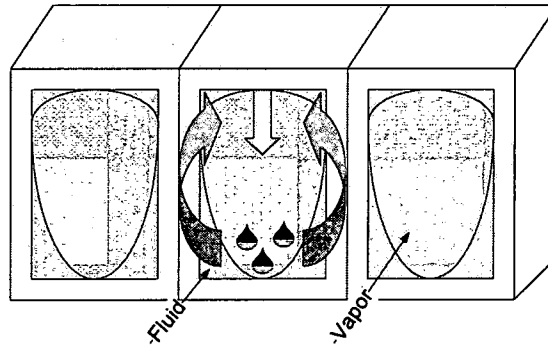


Figure 5.7: Schematic of micro heat pipe array.

Finally, the entropy generated due to actuation is calculated using equation 5.34.

$$\frac{S_{gen}}{A} = \frac{Q_{in}/T_s + Q_{in}/T_{sink}}{A} = 4925 \frac{J}{Km^2} \quad (5.34)$$

#### 5.4 Micro Heat Pipes

The final design considered is an array of micro heat pipes as seen in Fig. 5.7 and 5.8. The heat pipe is designed to have a working fluid that would evaporate and condense at a temperature close to 150°C. The design consists of a Silicon wafer, SU8 side walls, and a fluid/vapor mixture in each well. The bottom of the copper heat spreader serves as the top of the micro heat heat thermal switch. The physical dimensions of this design are shown in Table 5.4.

Silicon is chosen as the substrate material for its availability and relatively high thermal conductivity. SU8 is chosen as the wall material for its relatively low thermal conductivity and layer thickness. The properties of these materials are shown in Table 5.5.

Several working fluids are identified and 1-Propanol is chosen for several reasons. First of all, it is a relatively safe fluid to work with, and second, the saturation pressure spikes at a saturation temperature near 150°C as seen in Fig. 5.9. The properties of propanol in the evaporator section of the heat pipe are given in Table 5.6 [132, 133].

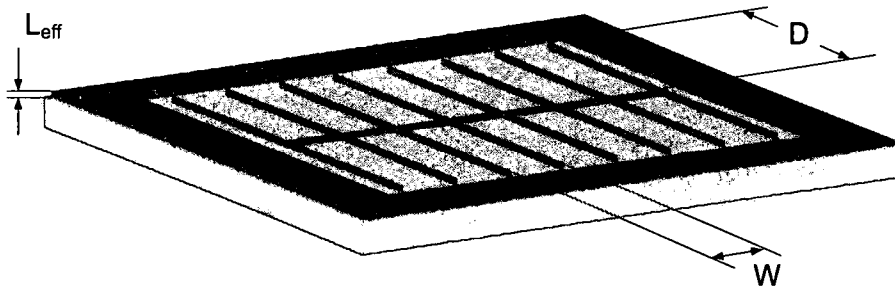


Figure 5.8: Illustration of micro heat pipe with design variables.

Table 5.4: Physical dimensions for micro heat pipe.

Variable	Description	Value
$t_{Si}$	Thickness of Si wafer	$280e-6$ m
$t_w$	Thickness of SU8 walls	$20e-6$ m
$D$	Length of heat pipe channel	$2000e-6$ m
$L_{eff}$	Height of heat pipe channel	$50e-6$ m
$W$	Width of heat pipe channel	$500e-6$ m

Table 5.5: Properties for Silicon and SU8.

Variable	Description	Value
$k_{Si}$	Thermal conductivity of Si	140 W/mK
$k_{SU8}$	Thermal conductivity of SU8	0.2 W/mK
$c_{p,Si}$	Specific heat of Si	678 J/kgK
$c_{p,SU8}$	Specific heat of SU8	1500 J/kgK
$\rho_{p,Si}$	Density of Si	$2330\text{kg/m}^3$
$\rho_{p,SU8}$	Density of SU8	$1200\text{ kg/m}^3$

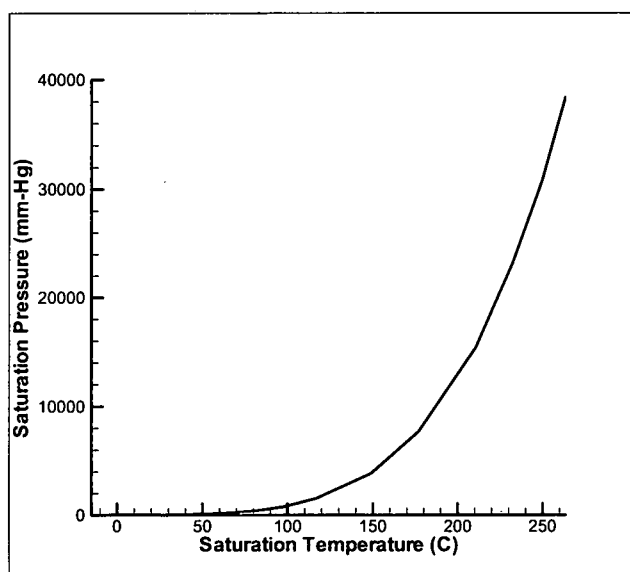


Figure 5.9: Saturation pressure and temperature for 1-Propanol [132].

Table 5.6: Physical parameters for evaporator section in micro heat pipe.

Variable	Description	Value
$P_{v,sat}$	Saturation pressure of vapor	683.6 KPa
$\sigma$	Interfacial tension	12.7e-3 N/m
$\rho_l$	Density of liquid	660 kg/m <sup>3</sup>
$\rho_v$	Density of vapor	13.8 kg/m <sup>3</sup>
$\mu_l$	Liquid viscosity	188e-6 Ns/m <sup>2</sup>
$\mu_v$	Vapor viscosity	11.5e-6 Ns/m <sup>2</sup>
$h_{fg}$	Latent heat of vaporization	544 KJ/kg
$k_l$	Thermal conductivity of liquid	133.5e-3 W/mK
$k_v$	Thermal conductivity of vapor	28.9e-3 W/mK
$c_{p,l}$	Specific heat of liquid	4360 J/kgK
$T_{evap}$	Temperature of the evaporator section	423 K

This micro heat pipe is modeled using steady state heat pipe equations provided in Faghri [95, 134]. The first parameter calculated is the maximum heat flow restricted by capillary action, or the ability of the fluid to wick up the solid SU8 walls in the corners.

The following equations are used to calculate the parameters needed to determine capillary limitation.

$$fRe = 15.115$$

$$A_v = DW$$

$$P_v = 2D + 2W$$

$$r_h = \frac{4A_v}{P_v}$$

$$\phi = \frac{\pi}{4}$$

$$\alpha = \frac{\pi}{180}$$

$$\psi = \frac{\pi}{2}$$

$$g = 9.81 \frac{m}{s^2}$$

$$C_1 = \frac{1}{2 \int \left( \frac{\cos(\alpha) \cos(\phi - \alpha) - (\sin^2(\theta) - \cos^2(\alpha) \sin^2(\phi - \theta))}{\cos(\alpha + \phi)} \right)^2 d\theta} = 0.833$$

$$\begin{aligned}
C_2 &= \frac{1}{\cos(\alpha + \phi) \sin(\phi)} \int \left( \cos(\alpha) \cos(\phi - \theta) - \left( \sin^2(\phi) - \cos^2(\alpha) \sin^2(\phi - \theta) \right)^{0.5} \right)^2 d\theta \\
&= 0.44
\end{aligned}$$

The following equations are solved iteratively to find the maximum heat flow associated with the capillary limitation.

$$\begin{aligned}
\Delta P_v &= \left( \frac{f Re \mu_v}{2 r_h^2 A_v \rho_v h_{fg}} \right) L_{eff} Q_{cap} \\
r_{cap,c} &= \frac{W}{2} \\
r_{cap,e} &= \frac{3\sigma}{4 \left( \frac{\sigma}{r_{cap,c} + \Delta P_v + \rho_l g L_{eff} \sin(\psi)} \right)} \\
C^* &= 0.5 \left( 1 + \frac{r_{cap,c}}{r_{cap,e}} \right) \\
Q_{cap} &= \left( \frac{\sigma}{r_{cap,e}} - \frac{\sigma}{r_{cap,c}} - \Delta P_v \right) \left( \frac{2 C_1 (C^* C_2 r_{cap,e})^4 \rho_l h_{fg}}{f Re \mu_l L_{eff}} \right)
\end{aligned}$$

After iteration converged, the maximum heat flow per area is calculated to be  $Q_{cap}/A = 5.71e6 \text{ W/m}^2$ :

The next limitation explored is the sonic limitation ensuring that the maximum vapor velocity never exceeds the speed of sound. Table 5.7 shows the estimated properties at the condenser section of the heat pipe. Using these values, maximum vapor velocity is estimated using equation 5.35.

$$c_0 = \sqrt{K R_g T_{cond}} \quad (5.35)$$

and the sonic limit is calculated using equation 5.36.

$$Q_{sonic} = \frac{\rho_l c_0 h_{fg} A_v}{\sqrt{2(K+1)}} \quad (5.36)$$

Table 5.7: Physical parameters for condenser section in micro heat pipe.

Variable	Value
$\rho_l$	732.5 kg/m <sup>3</sup>
$h_{fg}$	687 KJ/kg
$c_{p,l}$	3.21 J/kgK
$c_{p,v}$	1.65 J/kgK
$K$	1.2
$T_{cond}$	273 K

When the sonic limit is normalized by area, the maximum heat flow through the device due to the sonic limit is 4.68e10 W/m<sup>2</sup>. Since the capillary limit is less than the sonic limit, the maximum heat flow through the device is dictated by the capillary limit of 5.71 W/m<sup>2</sup>.

To estimate the thermal switching resistance ratio, the thermal resistances of each component of the micro heat pipe are calculated. The thermal resistance of the silicon wafer is determined by equation 5.37.

$$R_{bottom} = \frac{t_{Si}}{k_{Si} (W + t_w) (D + t_w)} \quad (5.37)$$

The thermal resistance of the SU8 walls are calculated from equation 5.38.

$$R_{wall} = \frac{L_{eff}}{k_{SU8} ((W + t_w) (D + t_w) - WD)} \quad (5.38)$$

The approximate thermal resistance of the interior of the micro heat pipe when the switch is 'off', assuming the entire volume is a saturated vapor, is calculated from equation 5.39.

$$R_{in} = \frac{L_{eff}}{k_v DW} \quad (5.39)$$

Noted that this calculation ignores the fact the liquid will be present in the corners. The thermal resistance when the switch is in the 'off' state is thus approximated by equation 5.40.

$$R_{off} = \frac{R_{wall} (R_{in} + R_{bottom})}{R_{wall} + R_{in} + R_{bottom}} \quad (5.40)$$

Finally, the thermal resistance when the switch is in the 'on' state is approximated by equation 5.41.

$$R_{on} = \frac{R_{wall} R_{bottom}}{R_{wall} + R_{bottom}} \quad (5.41)$$

From equations 5.40 and 5.41, the thermal switch resistance ratio is given by equation 5.42.

$$\text{Ratio} = \frac{R_{off}}{R_{on}} = 674 \quad (5.42)$$

The required energy to actuate the switch is calculated using the following equations.

$$\Delta T = T_{evap} - T_{cond} = 170K$$

$$V_{in} = DWL_{eff}$$

$$V_{SU8} = L_{eff} t_w D + W t_w D$$

$$V_{Si} = (D + t_w)(W + t_w) t_{Si}$$

$$Q_{in} = \rho_l V_{in} c_{p,l} \Delta T$$

$$Q_{SU8} = \rho_{SU8} V_{SU8} c_{p,SU8} \Delta T$$

$$Q_{Si} = \rho_{Si} V_{Si} c_{p,Si} \Delta T$$

$$Q_{actuation} = Q_{in} + Q_{SU8} + Q_{Si}$$

Required actuation energy per area becomes  $Q_{actuation} A = 87,727 \text{ W/m}^2$ . The mass to actuation energy is calculated using equation 5.43.

$$\frac{m/Q_{in}}{A} = 7.53 \frac{\text{kg}}{\text{Jm}^2} \quad (5.43)$$

Lastly, the entropy generated during the switching operation is calculated using equation 5.44.

$$S_{gen} = \frac{Q_{actuation}}{T_{evap}} + \frac{Q_{actuation}}{T_{cond}} \quad (5.44)$$

The entropy generated during switching per area becomes  $S_{gen}/A = 554 \frac{\text{J}}{\text{Km}^2}$ .

Table 5.8: Thermal switch design comparison.

	Horizontal MEMS	Vertical MEMS	Wax Well	Micro Heat Pipe
Switching ratio	1.5	16,000	1000	674
Required Actuation Energy ( $\text{J}/\text{m}^2$ )	470	1.83	780,000	87,726
Mass to Actuation Energy ( $\text{kg}/\text{Jm}^2$ )	3352	0.578	6,065	7.53
Maximum Heat Flow ( $\text{W}/\text{m}^2$ )	5.2e8	190.4	5.0e11	5.71e6
Entropy Generated ( $\text{J}/\text{Km}^2$ )	3.0	0.01	4,925	554

## 5.5 Design Comparison

Four designs for passive switch operation are compared in Table 5.8. From Table 5.8 the design with the largest switching ratio, lowest required actuation energy and entropy generated was the vertical MEMS design. This design unfortunately is associated with the lowest maximum heat flow through the device. Further, it was very sensitive to changes in temperature and other physical parameters of the design rendering it extremely difficult to reliably operate. The next best design was the micro heat pipe with a switching ratio of 674, required actuation energy of 87,726  $\text{J}/\text{m}^2$ , maximum heat flow through the device of 5.71e6  $\text{W}/\text{m}^2$ , and entropy generation of 554  $\text{J}/\text{Km}^2$ . This design was deemed to be robust and could easily be fabricated using a MEMS fabrication process. Because of these reasons, the micro heat pipe design was chosen to be fabricated, thermally characterized, and integrated with the whole energy harvesting system.



## Chapter 6

### Micro Heat Pipe Fabrication and Characterization

This chapter describes the fabrication process of the micro heat pipe array using MEMS fabrication techniques, the experimental set-up used to evacuate and fill the heat pipe, and its characterization relative to use as a passive thermal switch.

#### 6.1 Fabrication

The fabrication process of the micro heat pipe array starts with preparing a 275  $\mu\text{m}$  thick silicon wafer by polishing both the top and bottom sides as seen in Fig. 6.1a. The next step is to spin on a coat of SU8 negative photoresist at a thickness of 50  $\mu\text{m}$  as seen in Fig. 6.1b. This layer is first prebaked to set the photoresist. In Fig. 6.1c, a glass mask with patterned chrome is placed above the SU8 layer and exposed to UV light. Because

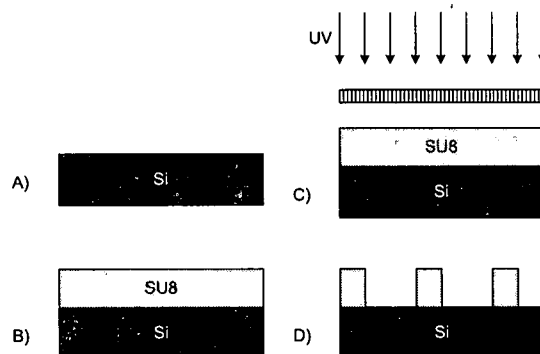


Figure 6.1: MEMS fabrication process for micro heat pipe array.

SU8 is a negative photoresist, the areas that are exposed to UV light form a strong acid. During the post exposure bake, an acid-initiate thermally driven epoxy cross-linking occurs, causing these sections of SU8 to become stronger. The weaker SU8 that is not exposed to UV light is stripped away with acetone leaving the stronger cross-linked SU8 attached to the silicon wafer as seen in Fig. 6.1 [135, 128].

The final thermal switch design that is fabricated using the MEMS fabrication process described above is shown in Fig. 6.2 and a photograph of the fabricated micro heat pipe is shown in Fig. 6.3. As can be seen from the drawing, each heat pipe chamber is 500  $\mu\text{m}$  wide, 50  $\mu\text{m}$  deep, and approximately 2 mm long. There are 14 heat pipe channels in the MEMS device. The overall coverage is 5 mm X 5 mm. The bottom of the copper heat spreader acts as the lid for the silicon heat pipe chip.

## **6.2 Assembly**

In order to characterize the thermal switch performance as a function of source temperature, the following characterization set-up is configured as shown in Fig. 6.4. This set-up consists of a cartridge heater, a copper heat spreader instrumented with five thermocouples, the thermal switch (heat pipe array), and the heat sink. The instrumented heat spreader is used to calculate heat flux through the heat spreader into the thermal switch.

To evacuate and fill the heat pipe area of the thermal switch, the set-up depicted in Fig. 6.5 is employed. The micro heat pipe array is epoxied to the copper heat spreader. The open channels of the micro heat pipe array are beneath a fill channel in the heat spreader. The fill channel interfaces with a hole in a stainless steel tube passing through the heat spreader (with a mating hole in the tube). On the left-hand side, this steel tube connects to a flexible tube which fits over a barb that is connected to the push-button gas tight syringe. On the right-hand side, the steel tube connects to a one-way valve. The other

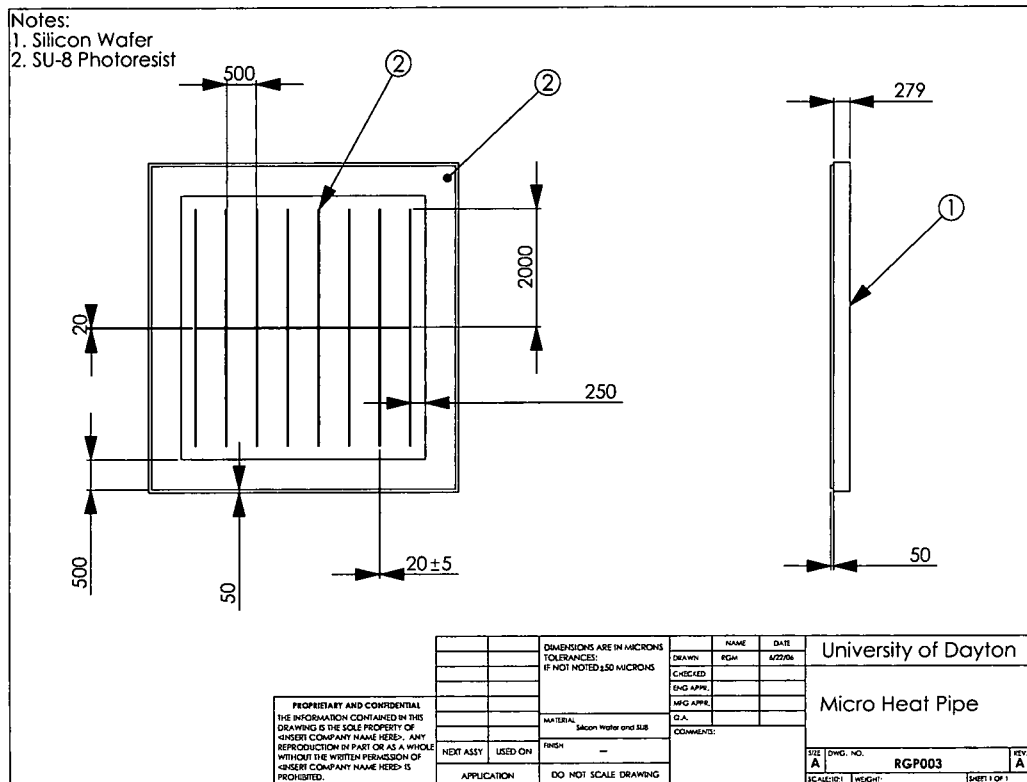


Figure 6.2: Drawing for final design of micro heat pipe array.

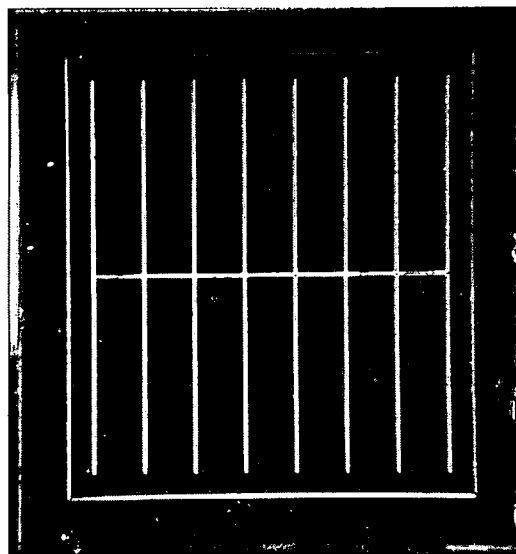


Figure 6.3: Photograph of final design of micro heat pipe array.

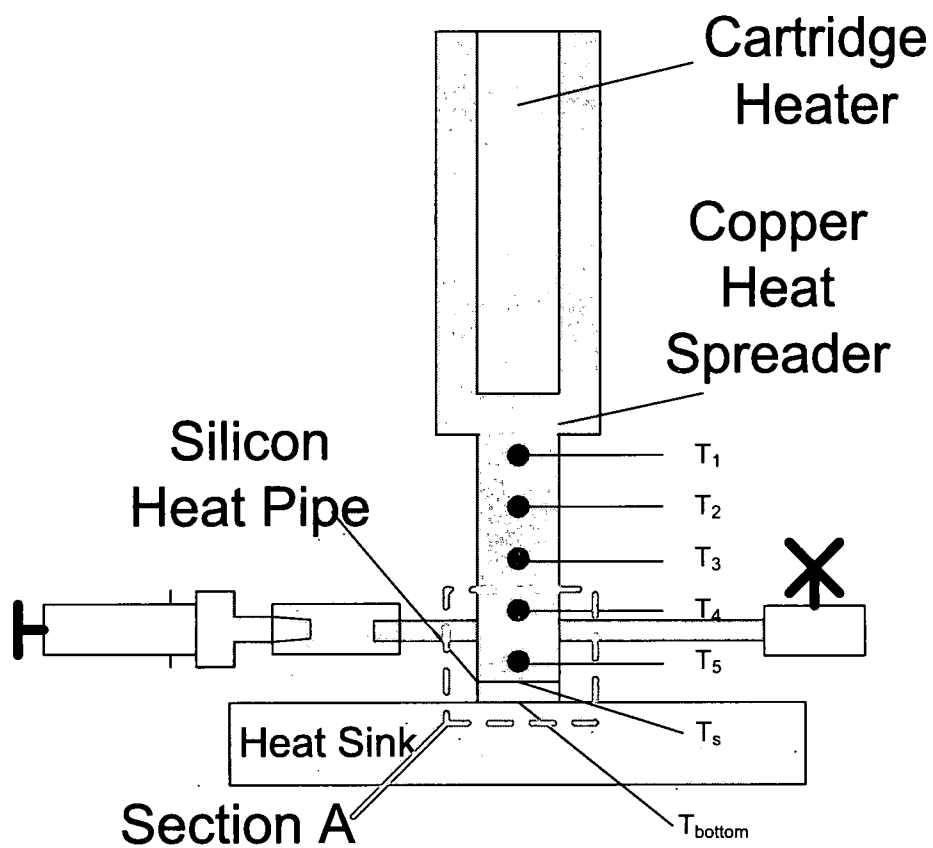


Figure 6.4: Schematic for experimental set-up for thermal switch temperature characterization.

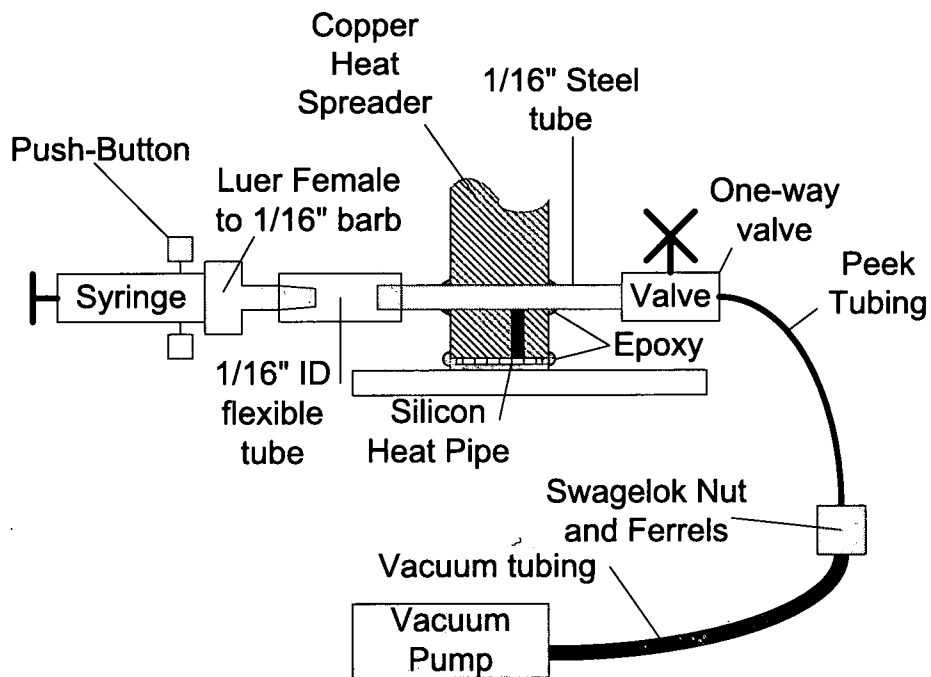


Figure 6.5: Section A, schematic for experimental set-up for filling the micro heat pipe.

side of the valve connects to PEEK tubing which fits to a Swagelok nut and ferrel assembly connected to the vacuum pump.

To evacuate the heat pipe area of the thermal switch, the following procedure is used. First, the push-button valve on the syringe is closed. Next, the one-way valve is opened and the vacuum pump is turned on. The vacuum pressure is monitored using a vacuum gauge. Once a vacuum level of -25 in.Hg. or lower is achieved, the one-way valve is closed.

To fill the now evacuated heat pipe with 1-Propanol, the gas-tight syringe push button valve is opened and the pre-fixed volume of 1-Propanol is dispensed into the heat pipe. The fluid volume is varied from a volume fraction, or fluid volume divided by total evacuated space, of 1 to 0.05.

## **6.3 Experimental Procedure**

Once the thermal switch is filled with the propanol, the test micro heat pipe array is aligned to ensure contact between the thermal switch bottom surface and the cold plate. The heater is turned on and the thermocouples are monitored until steady-state operation is assured. The temperatures of all thermocouples are recorded, and both the thermal resistance of the switch and source temperature are calculated.

Many variables can affect the heat pipe performance of a heat pipe thermal switch. Some of these variables include fluid choice and volume fill ratio. A series of characterization experiments are employed to identify proper fluid choices and fill ratios.

### **6.3.1 Thermal Switch Resistance Measurement**

The thermal switch thermal resistance is calculated from the thermocouple measurements indicated in Fig. 6.1. The temperatures at each thermocouple position are used to

estimate the heat flux into the thermal switch in the copper heat spreader. The heat flowing through the copper heat spreader is represented by equation 6.1.

$$Q = kA \frac{dT}{dx} \quad (6.1)$$

However, since the material is removed from the copper heat spreader for the insertion of the thermocouples, the heat measurement is corrected to account for the reduced cross-sectional area in the proximity of the thermocouples as shown in Fig. 6.6. To simplify the correction, the thermocouple material voids are assumed to be square holes with a volume equal to the actual cylindrical holes drilled into the copper heat spreader. The effective thermal resistance of the copper heat spreader where thermocouples are present, section A – A, is equal to  $L_1/kA_1$  where the length is 0.0014 m and the cross-sectional area is  $4.01\text{e-}5 \text{ m}^2$  yielding an effective thermal resistance of 0.09 K/W. Similarly, the thermal resistance of the heat spreader in between thermocouple locations, section B – B, is  $L_2/kA_2$  where the length is 0.0034 m and the cross-sectional area is  $4.36\text{e-}5 \text{ m}^2$ , which results in a thermal resistance of 0.20 K/W. The total effective thermal resistance between thermocouple measurements is calculated by adding the thermal resistances of sections A – A and B – B in Fig. 6.6 as shown in equation 6.2.

$$R_{\text{eff}} = R_{\text{cu}} + R_{\text{TC}} = 0.09 \text{ K/W} + 0.20 \text{ K/W} = 0.29 \text{ K/W} \quad (6.2)$$

Now, knowing that the distance,  $\Delta x$ , in between thermocouples is 0.004763 m and that the term  $dT/dx$  is approximated by  $(T_i - T_{i-1})/\Delta x$ , the simplified heat flow is represented by equations 6.3 and 6.4.

$$Q = \frac{T_i - T_{i-1}}{R_{\text{eff}}} = 3.4359 (T_i - T_{i-1}) \quad (6.3)$$

$$Q = 3.4359 \Delta x \frac{(T_i - T_{i-1})}{\Delta x} = 3.4359 (0.004763) \frac{(T_i - T_{i-1})}{\Delta x} \approx 0.016365 \frac{dT}{dx} \quad (6.4)$$

The derivative,  $dT/dx$  is calculated using the first four thermocouples. The fifth thermocouple reading is altered due to its proximity to the heat pipe filling port and is therefore



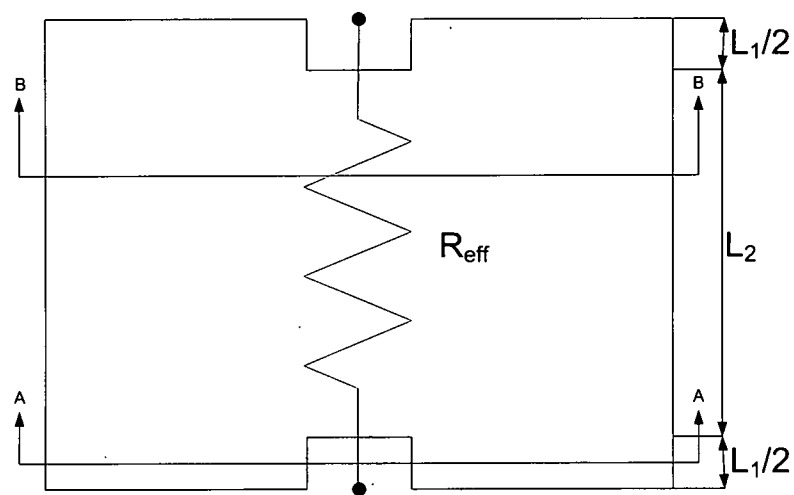


Figure 6.6: Effective thermal resistance of copper heat spreader accounting for thermocouple holes.

neglected. A least squares regression method is used to determine the best fit line from which  $dT/dx$  and  $T_s$  are calculated. Equation 6.5 represents the estimated temperature as a function of  $x$  [136].

$$T(x) = \frac{S_{XT}}{S_X^2} (x - \bar{x}) + \bar{T} \quad (6.5)$$

where  $S_{XT}$  and  $S_X$  are the sample variance and covariance and are given by the following equations.

$$S_X^2 = \sum \frac{(x - \bar{x})^2}{n} \quad (6.6)$$

$$S_{XT} = \sum \frac{(x - \bar{x})(T - \bar{T})}{n} \quad (6.7)$$

From equation 6.5,  $dT/dx$  is estimated by the slope of the best fit line of the recorded temperatures represented by equation 6.8.

$$\frac{dT}{dx} = \sum \frac{S_{XT}}{S_X^2} \quad (6.8)$$

The source temperature, or the temperature at the top of the thermal switch is estimated using this slope. The total thermal resistance from the 4<sup>th</sup> thermocouple to the top of the thermal switch is 1.005383 K/W and is calculated using the thermal resistance for conduction ( $R = L/kA$ ) and adjusting for the changing cross-sectional area due to the fill ports as shown in Fig. 6.5. Using this corrected thermal resistance and the heat calculated from equation 6.3, the estimated source temperature is calculated as shown in equation 6.9

$$T_s = T_4 - QR = T_4 - 1.005383Q \quad (6.9)$$

The thermal resistance of the thermal switch is calculated using the estimated temperature at the source and heat pipe interface, the measured temperature from the thermocouple beneath the thermal switch,  $T_{bottom}$ , and the measured heat flowing through the copper heat spreader as given by equation 6.10.

$$R_{switch} = \frac{Q}{T_s - T_{bottom}} \quad (6.10)$$

Table 6.1: Experimental uncertainty associated with heat flow, source temperature, and thermal resistance of thermal switch.

Variable	Uncertainty (%)
Q	$\pm 2.4$
$T_s$	$\pm 1.25$
$R_{\text{switch}}$	$\pm 3.8$

#### 6.3.1.1 Uncertainty

The uncertainty of the thermal resistance calculation of the thermal switch is estimated knowing the tolerances of the copper heat spreader design, estimated thermocouple separation variation in the heat spreader, and the standard deviation of experimental data. The subsequent thermal resistance uncertainty of the copper heat spreader is calculated to be  $\pm 0.001218$  K/W. The uncertainty of the temperature difference across the thermal switch was experimentally determined to be  $\pm 0.1\%$  and for the temperature measured from the thermocouples is  $\pm 1^\circ\text{C}$ . The corresponding uncertainty associated with the heat flow through the heat spreader is calculated to be  $\pm 2.4\%$ . The experimental uncertainty associated with the heat flowing through the system, the estimated source temperature, and the thermal resistance of the thermal switch is outlined in Table 6.1.

## 6.4 Results

### 6.4.1 Baseline

The first step in characterizing the thermal switch performance is to gain a baseline of thermal resistance associated with the silicon chip and SU8 photoresist used to construct the device in the absence of a fluid fill. To accomplish this task, the thermal resistance of the thermal switch is determined with air in the channels and under vacuum as seen in Table 6.2. As observed in this table, the thermal resistance of the thermal switch

Table 6.2: Physical and spatial variables that remain fixed for all numerical cases studied

Condition	R (K/W)
Air	$23.8 \pm 3.8$ K/W
Vacuum	$24.0 \pm 3.8$ K/W

under vacuum is slightly greater than when the micro heat pipe array is filled with air which makes sense. When the air is evacuated, the only path for heat to travel through the switch is by conduction through the SU8 walls and radiation from the top hot surface to the bottom cool surface. When the air is present inside the chambers, convection also adds to the heat transfer and therefore lowers the thermal resistance [137].

#### 6.4.2 Thermal Switch Filled with Propanol

Note, tests were conducted after filling the heat pipe propanol as the working fluid at various volume fractions.

##### 6.4.2.1 Liquid Volume Fraction of 1

The thermal switch is filled completely with propanol. Figure 6.7 shows the thermal resistance of the switch as a function of source temperature. Apparent from this plot is that thermal resistance of the heat pipe filled with propanol is less than with air or vacuum. Therefore it is assumed that heat is conducting through the propanol and decreasing thermal resistance, although not appreciably so. Also observed from the plot, is that the thermal resistance of the switch decreases with increasing source temperature. This indicates some form of phase change at elevated temperatures. Once the source temperature exceeds  $75^{\circ}\text{C}$ , the source temperature is seen to fluctuate as illustrated in Fig. 6.8.

This fluctuation indicates nucleation of a bubble. As the bubble size grows, the thermal resistance of the thermal switch increases due to the decrease of fluid in the heat

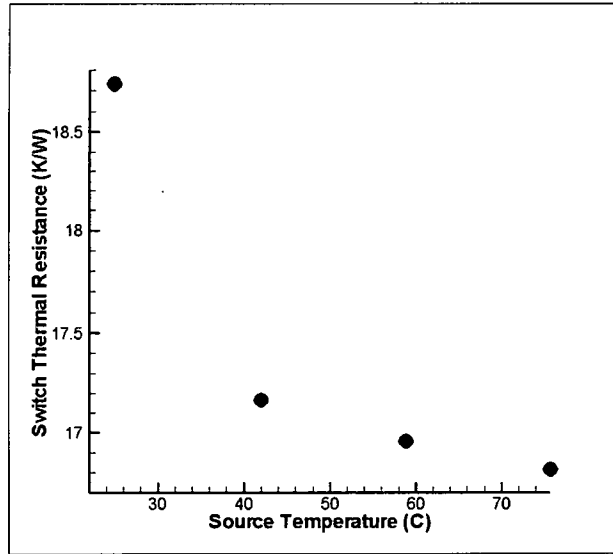


Figure 6.7: Plot of thermal resistance of thermal switch with propanol as a function of source temperature with a liquid volume fraction of 1.

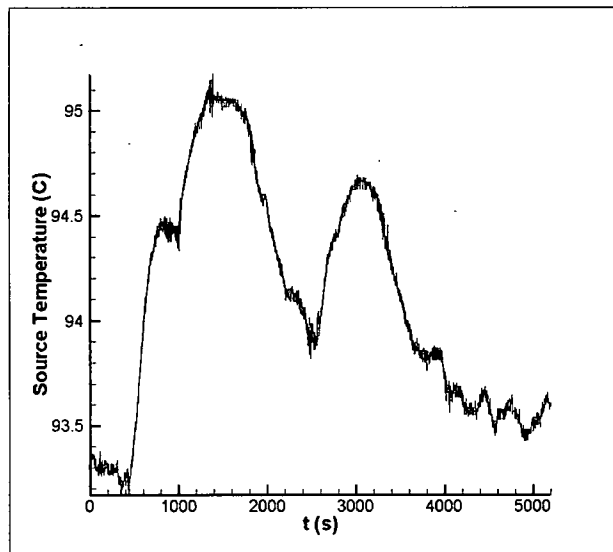


Figure 6.8: Plot of source temperature with a thermal switch with propanol with a liquid volume fraction of 1 at heat input of 10 W.

pipe channels [138]. The source temperature is seen to increase by almost  $2^{\circ}\text{C}$  and then returns to the original temperature. As a consequence, the thermal resistance of the switch also fluctuates, as seen in Fig 6.9, where the thermal resistance is observed to increase from  $16.8\text{ K/W}$  to  $17.8\text{ K/W}$ .

#### **6.4.2.2 Liquid Volume Fraction of 0.3**

For proper heat pipe operation, saturated liquid and vapor must be present, so smaller volume fill fractions are explored. Figure 6.10 shows the thermal resistance of the thermal switch with a liquid fill ratio of 0.3. As can be seen from this figure, the thermal resistance of the switch initially is  $10.8\text{ K/W}$ , but as the source temperature increases, the thermal resistance decreases to  $8.1\text{ K/W}$  yielding a thermal resistance ratio of 1.3, well below the desired ratio of 500. Also, the thermal resistance begins to drop when the source temperature is near  $40^{\circ}\text{C}$ , well below the desired temperature near  $150 - 160^{\circ}\text{C}$ .

#### **6.4.2.3 Liquid Volume Fraction of 0.1**

For a volume fraction of 0.1, the thermal resistance drops from  $7.8\text{ K/W}$  to  $6.5\text{ K/W}$  over a temperature range of  $15^{\circ}\text{C}$  to  $125^{\circ}\text{C}$  as seen in Fig. 6.11. The thermal resistance ratio is calculated to be 1.2.

The overall thermal resistance of the switch with the 0.1 fill ratio is less than the switch with the 0.3 fill ratio. This indicates that the 0.1 switch has more phase change occurring resulting in the lower thermal resistance.

Although no fluctuations of source temperature are observed for a liquid volume fraction of 0.3 or 0.1, a heat pipe with these volume fractions could still be used as a thermal switch when the heat source varies with time because thermal resistance is a function of source temperature. As the source temperature increases, the thermal resistance of the switch decreases allowing more heat to flow through the system. In contrast, as the source

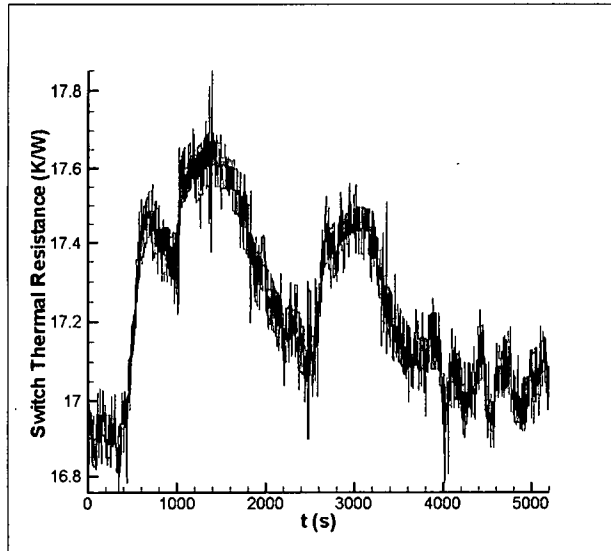


Figure 6.9: Plot of thermal resistance of thermal switch with propanol as a function of source temperature with a liquid volume fraction of 1 at heat input of 10 W.

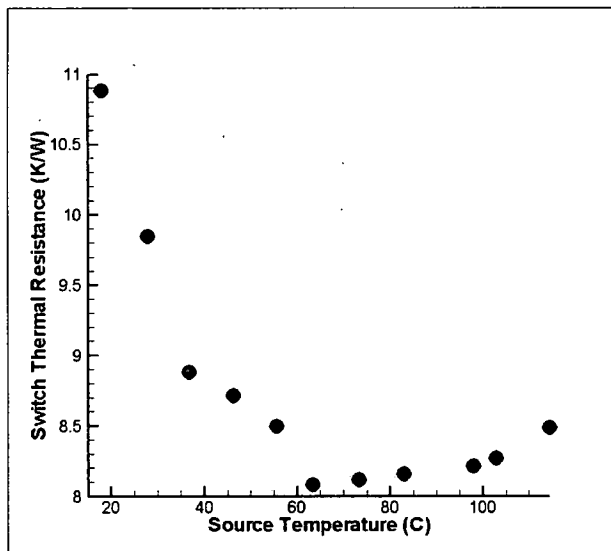


Figure 6.10: Plot of thermal resistance of thermal switch as a function of source temperature with a liquid volume fraction of 0.3 of propanol.

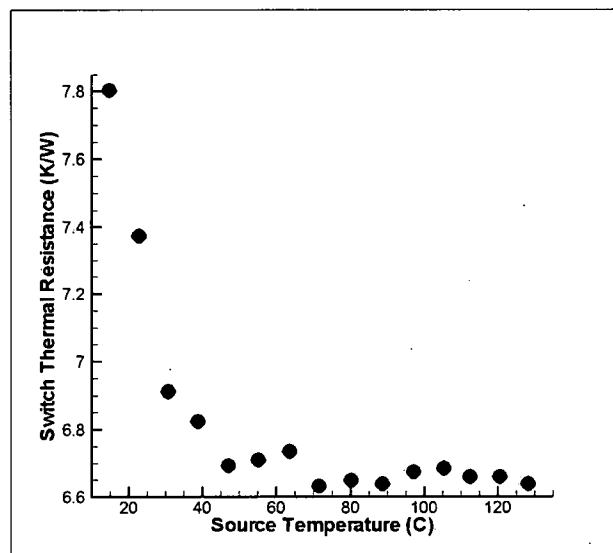


Figure 6.11: Plot of thermal resistance of thermal switch as a function of source temperature with a liquid volume fraction of 0.1 of propanol.



temperature decreases, the thermal resistance increases, resulting in energy storage in the heat source. Unfortunately, the thermal resistance ratio was far smaller than desired.

To summarize the performance of the heat pipe filled with propanol, thermal switching behavior was observed for constant heat inputs when the fill ratio was 1. The heat pipe with lower fill ratios could still act as a thermal switch but for variable heat inputs. Regardless of the heat input, all data sets recorded with propanol exhibited switching behavior well below the desired temperatures. Therefore different fluid choices are explored.

#### **6.4.3 Thermal Switch Filled with Decane**

The next fluid tested was decane. As seen in Fig. 6.12, the saturation pressure starts to spike at a higher saturation pressure indicating that the phase change during heat pipe operation will occur at higher temperatures.

##### **6.4.3.1 Liquid Volume Fraction of 0.1**

A volume fraction of 0.1 is chosen to ensure saturated vapor and liquid are present in the heat pipe channels. Figure 6.13 shows the measured thermal resistance of the micro heat pipe as a function of source temperature.

As can be seen from this figure, the transition temperature is near 60°C for decane, compared to 30°C for propanol. Recalling that the desired transition temperature is near 150°C, decane produces results closer to the required temperature range, but still not close enough. The thermal switch filled with 10% decane has an upper thermal resistance of 18.4 K/W and a lower resistance of 13.4 K/W yielding a thermal resistance ratio of 1.4, still well below the ratio of 500 that was desired but greater than the thermal resistance ratios for propanol.

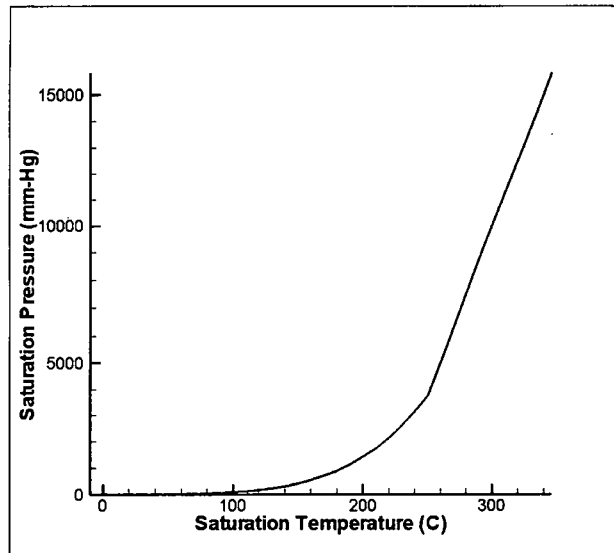


Figure 6.12: Saturation pressure and temperature for Decane [139].

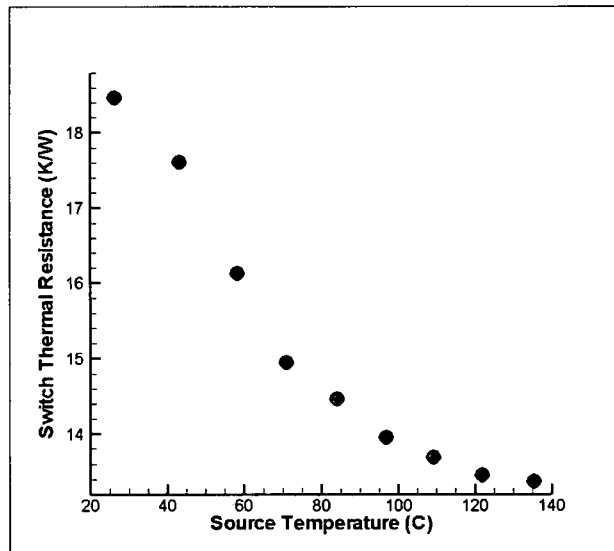


Figure 6.13: Plot of thermal resistance of thermal switch as a function of source temperature with a liquid volume fraction of 0.1 of decane.

#### **6.4.3.2 Volume Fraction of 0.2**

A volume fraction of 0.2 is also tested. Figure 6.14 shows the thermal resistance of the micro heat pipe as a function of source temperature. It is clear that the thermal resistance of the switch decreases as the source temperature increases but there is no evidence of a quick drop-off needed for proper switch operation. Also, there is very little thermal resistance change over this temperature range. Therefore, it is evident that a heat pipe filled with 20% decane is not appropriate for this application.

#### **6.4.3.3 Volume Fraction of 0.05**

Because it is evident that larger liquid volume fractions do not produce the desired results, a volume fraction of 0.05 is tested. The thermal resistance drops near a temperature of 50°C, well below the desired temperature, and the thermal resistance ratio is about 1.6 as seen in Fig, the highest of any condition evaluated. 6.15.

In conclusion, decane proved to be a better fluid choice for the desired application but still resulted in less than desired thermal resistance ratios and transition temperatures. An even larger hydrocarbon chain likely could achieve the desired micro heat pipe performance.

This chapter outlined the fabrication and characterization of a micro heat pipe thermal switch. The MEMS based thermal switch design was filled with propanol and decane at different fill ratios and conceptually demonstrated that a micro heat pipe could be used as a thermal switch.

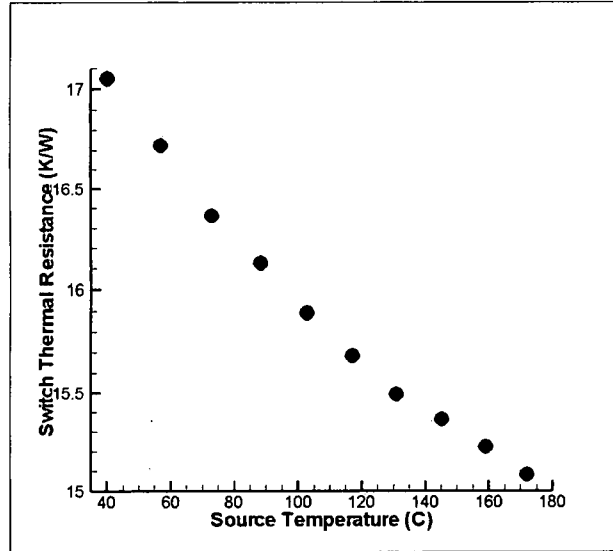


Figure 6.14: Plot of thermal resistance of thermal switch as a function of source temperature with a liquid volume fraction of 0.2 of decane.

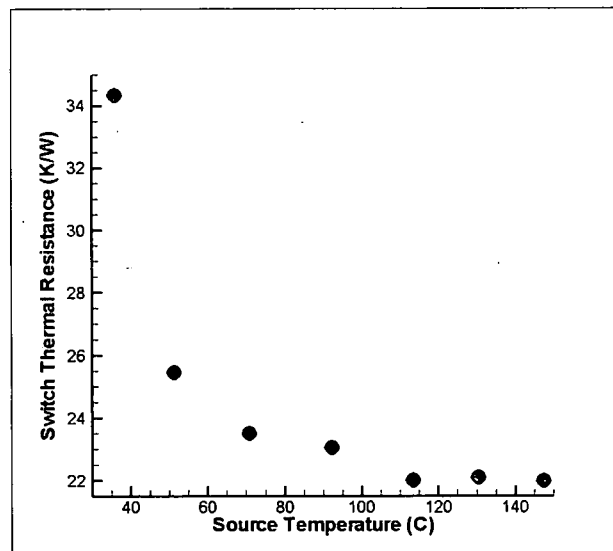


Figure 6.15: Plot of thermal resistance of thermal switch as a function of source temperature with a liquid volume fraction of 0.05 of decane.

## **Chapter 7**

### **Conclusions and Recommendations**

#### **7.1 Thermal Switching Enhancement of Energy Harvesting**

This dissertation successfully investigated the promise of thermal switching in thermoelectric energy harvesting. First, analytical models were used to study the enhancement of thermoelectric energy harvesting with source temperature control. The RC equivalent analysis utilized an electrical equivalent model to understand the controlling parameters of the energy harvesting system with and without source temperature switching. From this analysis, it was evident that the thermal capacitance of the source and the TE device were important to determine the effectiveness of thermal switching. The next model numerically investigated the system in more detail using a finite difference approach. From this model, it was shown that thermoelectric energy harvesting could realistically be enhanced with thermal switching by up to 35%.

Next, an experimental set-up with a variable air-gap serving as the thermal switch was employed and verified a thermal switching enhancement of 15% and 30% for constant and variable heat input respectively. This experiment also supported the fact that the source thermal capacitance must be greater than the TE device thermal capacitance for thermal switching to enhance TE energy harvesting.

After comparing several possible thermal switch designs, a micro heat pipe design was identified as the best solution. Using steady-state heat pipe analysis, a MEMS based

micro heat pipe was designed, fabricated, and characterized for thermal resistance performance at different source temperatures. The MEMS based thermal switch design was filled with propanol and decane at different fill ratios and conceptually demonstrated that micro heat pipe could be used as a thermal switch. In particular, a fill ratio of 1 (pure liquid) led to bubble nucleation that resulted in variable thermal resistance for constant heat inputs. Also, fill ratios between 0.05 and 0.3 demonstrated some thermal switching capability as a result of internal evaporation and condensation. However, the thermal resistance swing as the source temperature increased was far less than desired. Although the micro heat pipe showed variable thermal resistance as the source temperature change, the thermal resistance ratio was not great enough. Also, the thermal resistance transitioned at temperatures much lower than the desired temperature of 150°C.

## **7.2 Recommendations**

Future micro heat pipe designs should include several alterations. First, the heat pipe channels should be widened to increase the thermal resistance in the 'off' state. This would also increase the evaporation and condensation and therefore heat flow during the 'on' state. Second, every effort should be made to decrease the inlet and outlet volumes. In the design tested in this dissertation, this excess volume far exceeded the heat pipe volume making it very difficult to ensure the presence of saturated liquid and vapor in the test area. Third, another working fluid needs to be identified with a transition temperature closer to the required 150°C. With these changes, the micro heat pipe design should have higher thermal resistance ratios and a more desirable transition temperature. Another option is to design a conventional heat pipe more on a macro-scale as illustrated in Fig. 7.1. This design could utilize a polymer as the structural material with long porous channels thus increasing the thermal resistance of the switch in the absence of phase change. In

addition, the heat source is located beneath the switch utilizing gravity to assist fluid flow by forcing condensed liquid to fall back to the heated surface. Once a suitable thermal switch has been designed, and experimentally characterized, it should be integrated with a TE device to test overall performance.

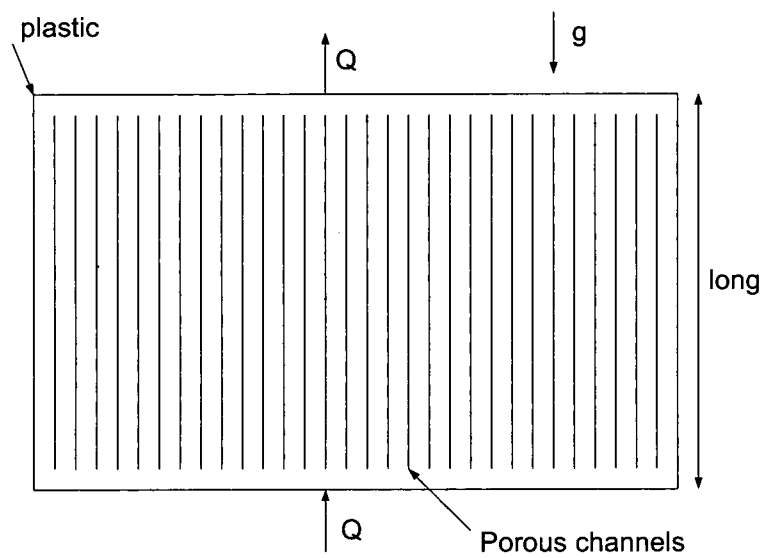


Figure 7.1: Illustration of macro-scale heat pipe design for a thermal switch.



## **Appendix A**

### **Publications**

#### **A.1 Peer-Reviewed Journal Publications**

McCarty, R., Hallinan K. P., Sanders, B., and Sophomone, T. "Enhancing Thermoelectric Energy Recovery Via Modulations of Source Temperature for Cyclical Heat Loadings," to be published in Journal of Heat Transfer, June 2007.

McCarty, R., Monaghan, D., Hallinan, K., and Sanders, B., "Experimental Verification of Source Temperature Modulation Via a Thermal Switch in Thermoelectric Energy Harvesting," to be published in Journal of Thermophysics and Heat Transfer, 2007.

#### **A.2 Peer-Reviewed Conference Publications**

Eger, C., Kocoloski, M., McCarty, R., Kissock, K., Hallinan, K. P., "Industrial Solid-State Energy Harvesting: Potential, Mechanisms, and Examples," submitted to American Council for an energy-Efficient Economy Summer Study in Energy Efficiency in Industry, July 24-27, 2007.

McCarty, R., Monaghan, D., Hallinan, K., and Sanders, B., "Experimental Verification of Source Temperature Modulation Via a Thermal Switch in Thermoelectric Energy Harvesting," American Society of Mechanical Engineers International Mechanical Engineering Congress and Exposition, November 5-10, 2006.

Pastor, C., Sanders, B., Joo, J., and McCarty, R., "Kinematically Designed Flexible Skins for Morphing Aircraft," American Society of Mechanical Engineers International Mechanical Engineering Congress and Exposition, November 5-10, 2006.

Ahlers, K., Hallinan, K., Sanders, B., and McCarty, R., "Design of a Multifunctional Aircraft Skin with Energy Harvesting Via Entropy Generation Minimization," American Society of Mechanical Engineers International Mechanical Engineering Congress and Exposition, November 5-10, 2006. to be submitted to International Journal of Exergy.

Sanders, B., McCarty, R., Ahlers, K., and Hallinan, K. P., "Structurally Integrated Thermal Energy Harvesting Subsystems," North Atlantic Treaty Organization Research and Technology Organization Specialist Meeting of Multifunctional Structures, October 2-6, 2006, Vilnius, Lithuania.

McCarty, R., Hallinan, K. P., Sanders, B., and Sophomone, T., "Enhancing Thermoelectric Energy Recovery Via Modulations of Source Temperature for Cyclical Heat Loadings," Proceedings of American Society of Mechanical Engineers and Pacific Rim Technical Conference and Exhibition on Integration and Packaging of MEMS, NEMS, and Electronic Systems, July 17- 22, 2005.

Ahlers, K., McCarty, R., Hallinan, K., and Sanders, B., "Optimal Design of a Multifunctional Aircraft Skin with Energy Harvesting Via Entropy Generation Minimization," International Green Energy Conference, June 12-16, 2005, Waterloo, Canada.

## Appendix B

### Variable Air-Gap Experimental Results, Constant Heat Input

The following plots are the result of the variable air-gap test for constant heat input. Several source capacitances were tested that include  $C_s = 38.5$ , 100, and 300 J/K.

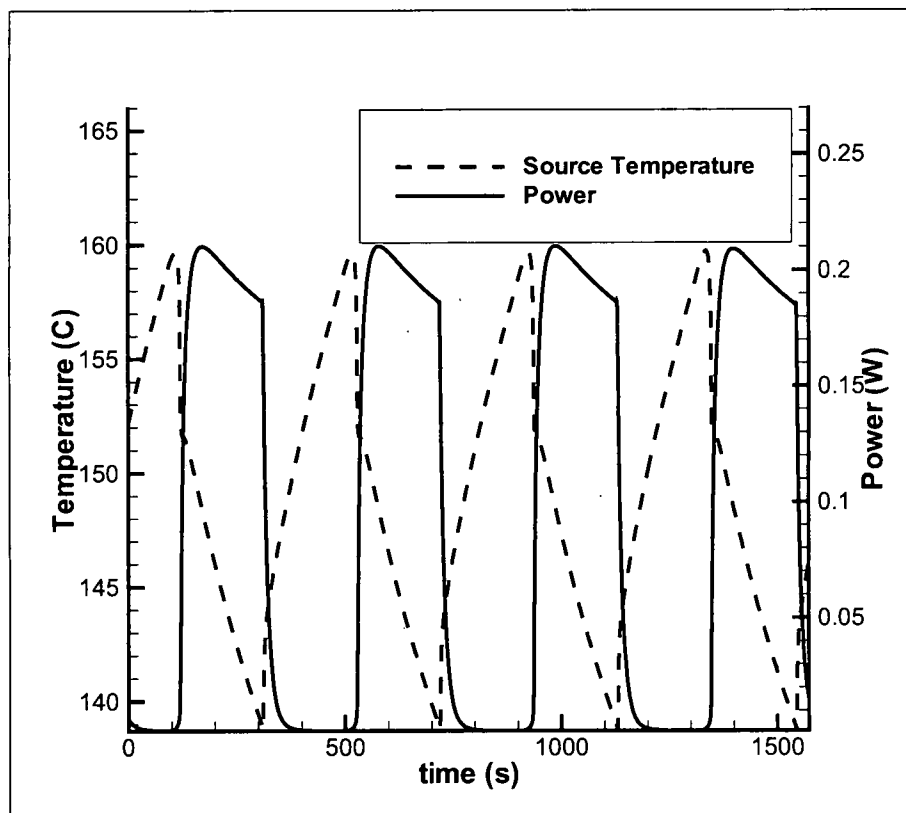


Figure B.1: Source temperature and TE output power with  $C_s = 38.5$  J/K, and  $\Delta T_s = 20^\circ\text{C}$ .

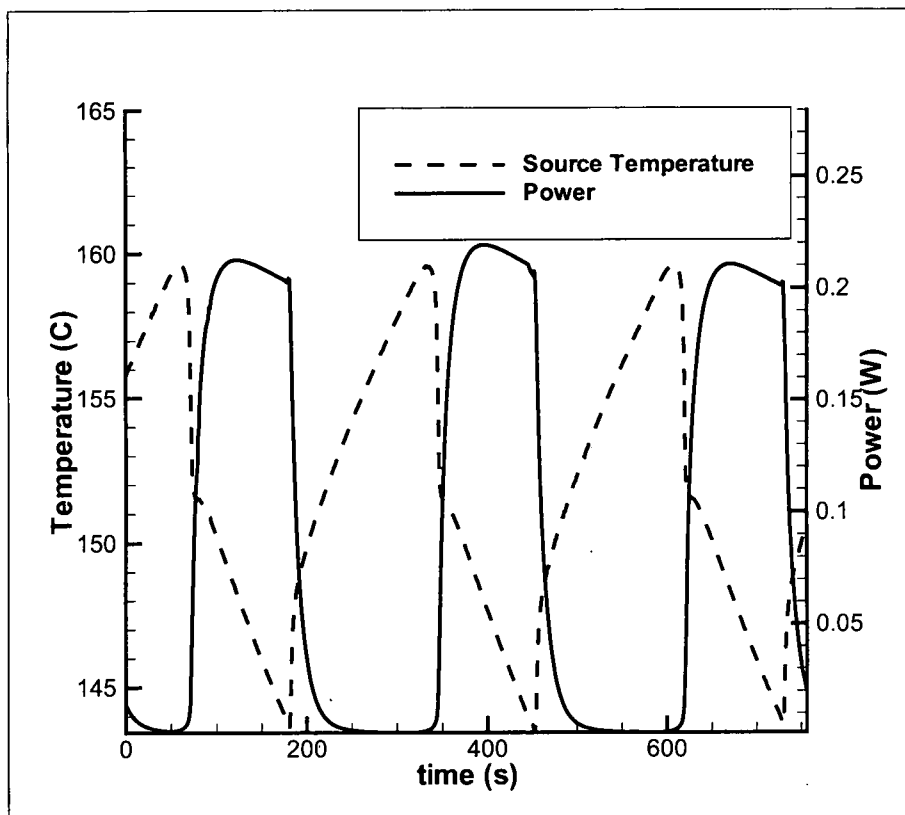


Figure B.2: Source temperature and TE output power with  $C_s = 38.5\text{J/K}$ , and  $\Delta T_s = 15^\circ\text{C}$ .

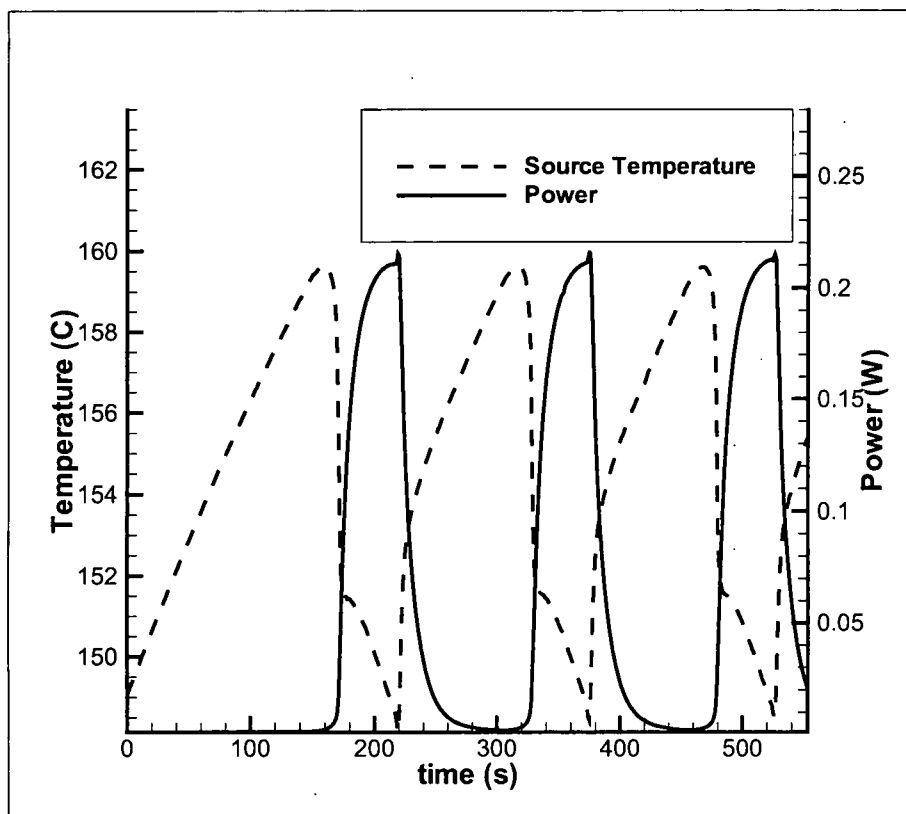


Figure B.3: Source temperature and TE output power with  $C_s = 38.5\text{J/K}$ , and  $\Delta T_s = 10^\circ\text{C}$ .

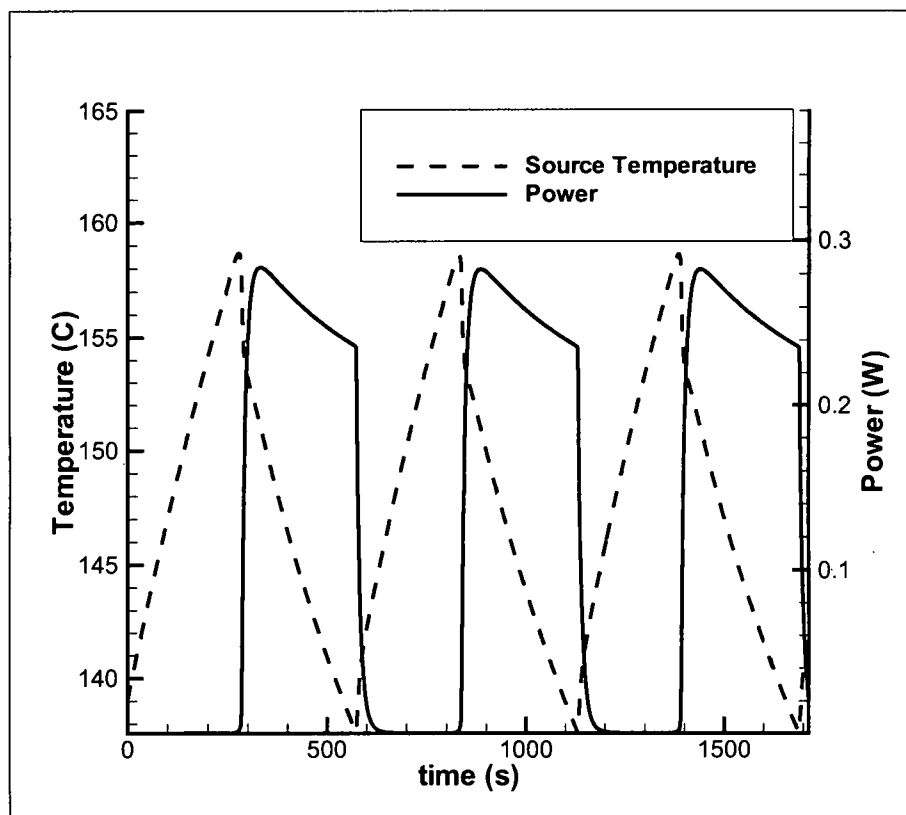


Figure B.4: Source temperature and TE output power with  $C_s = 100\text{J/K}$ , and  $\Delta T_s = 20^\circ\text{C}$ .

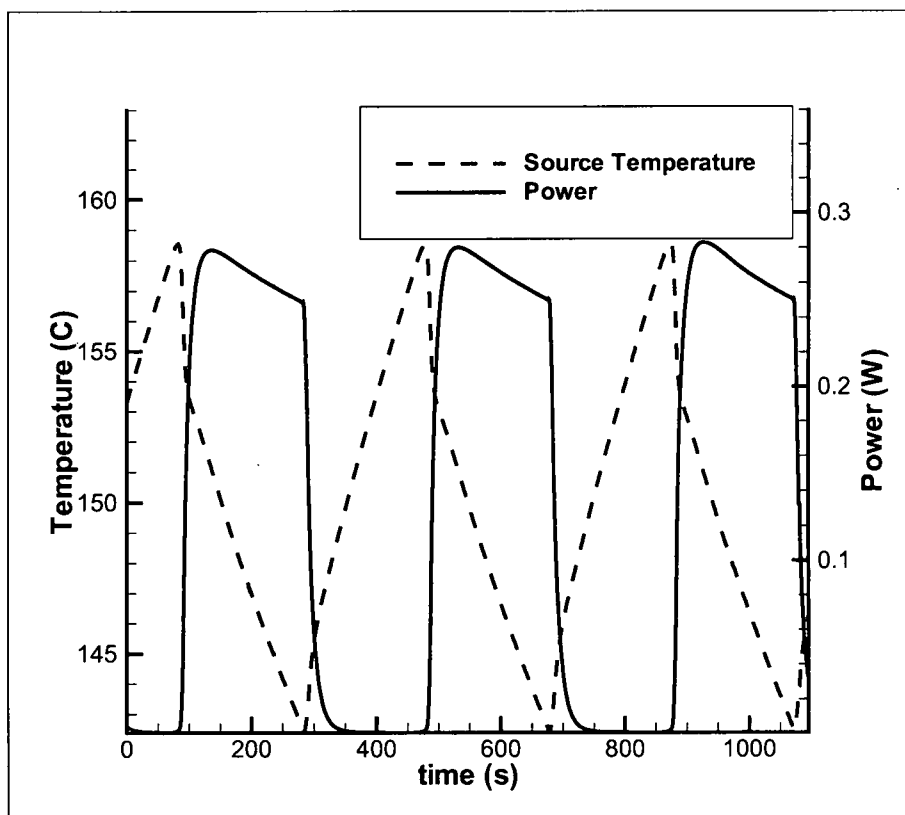


Figure B.5: Source temperature and TE output power with  $C_s = 100\text{J/K}$ , and  $\Delta T_s = 15^\circ\text{C}$ .

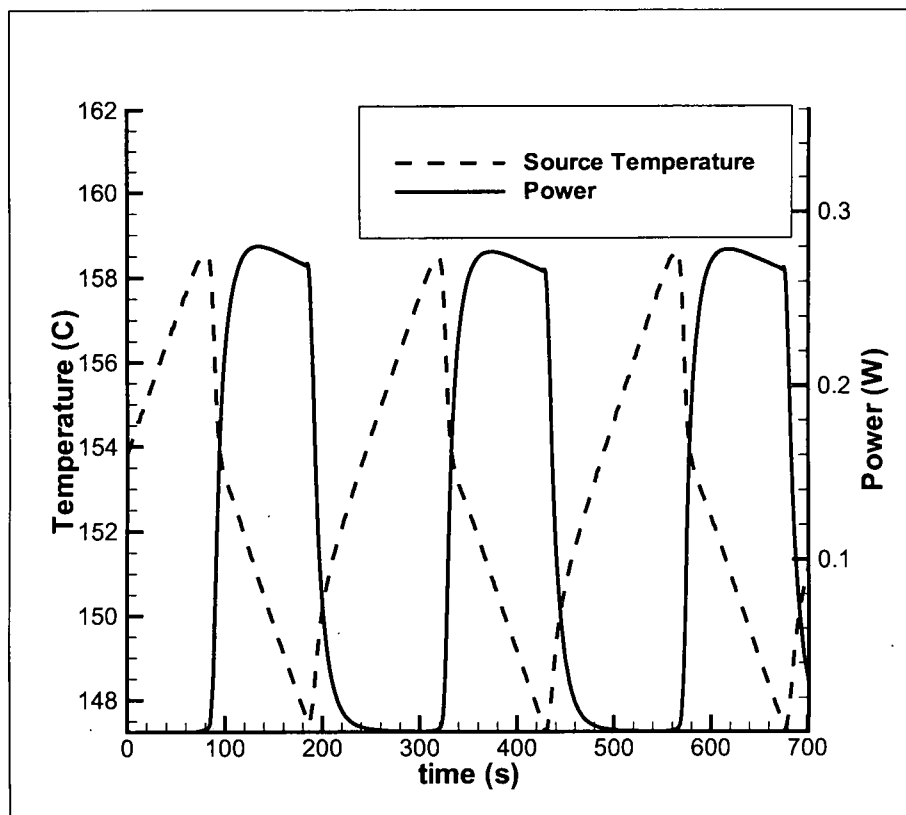


Figure B.6: Source temperature and TE output power with  $C_s = 100\text{J/K}$ , and  $\Delta T_s = 10^\circ\text{C}$ .



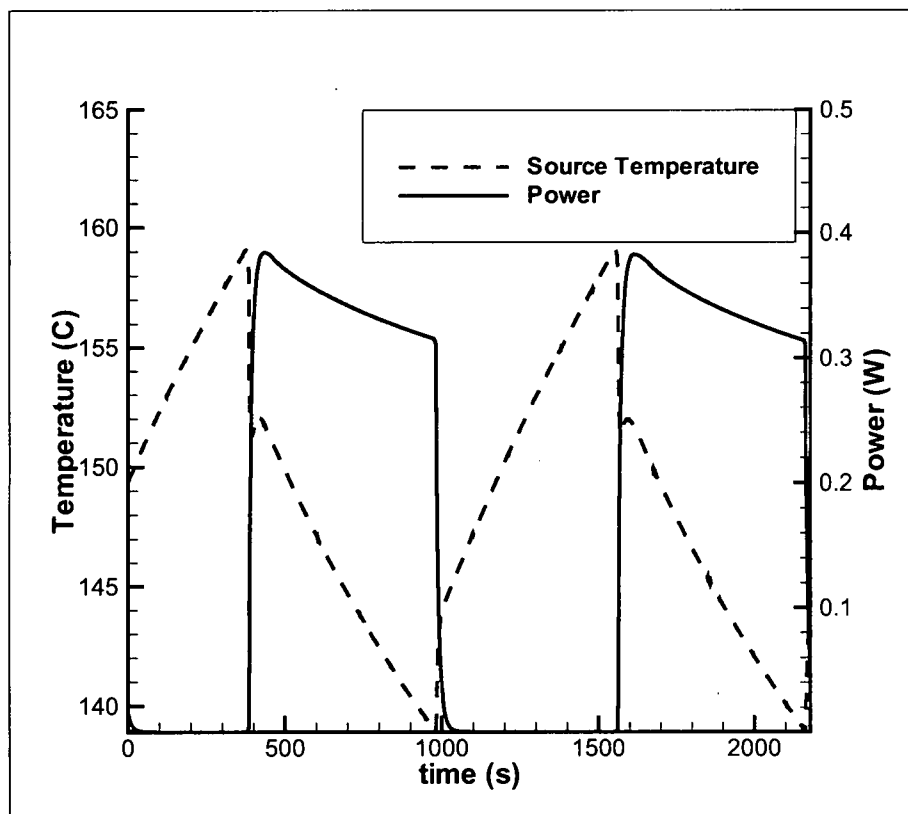


Figure B.7: Source temperature and TE output power with  $C_s = 300\text{J/K}$ , and  $\Delta T_s = 20^\circ\text{C}$ .

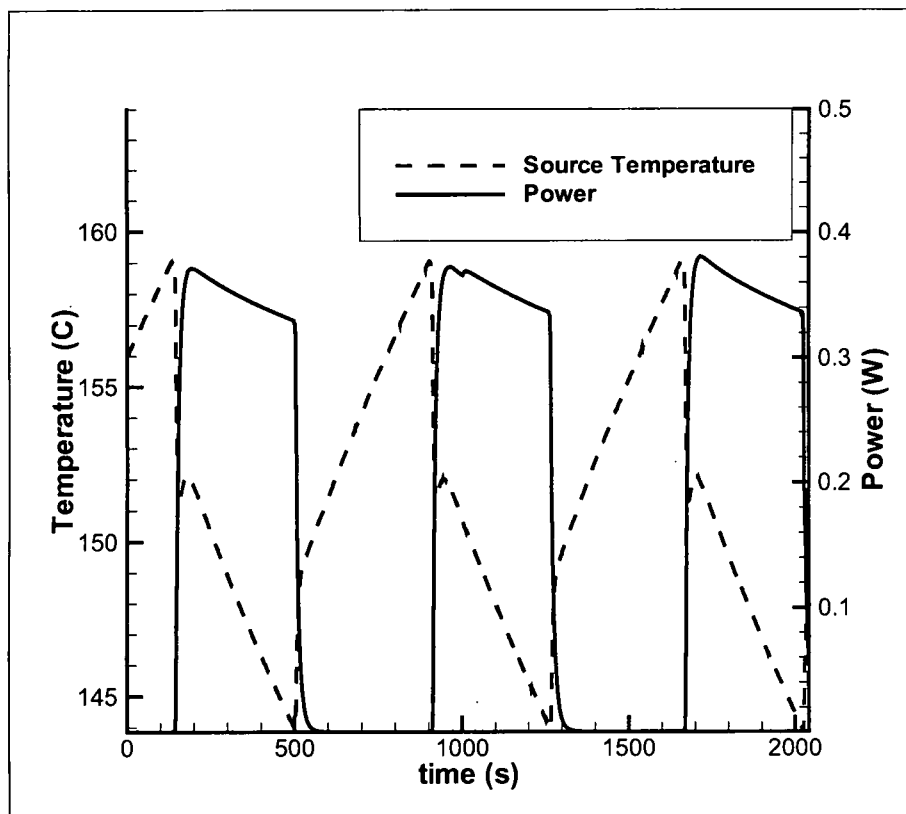


Figure B.8: Source temperature and TE output power with  $C_s = 300\text{J/K}$ , and  $\Delta T_s = 15^\circ\text{C}$ .

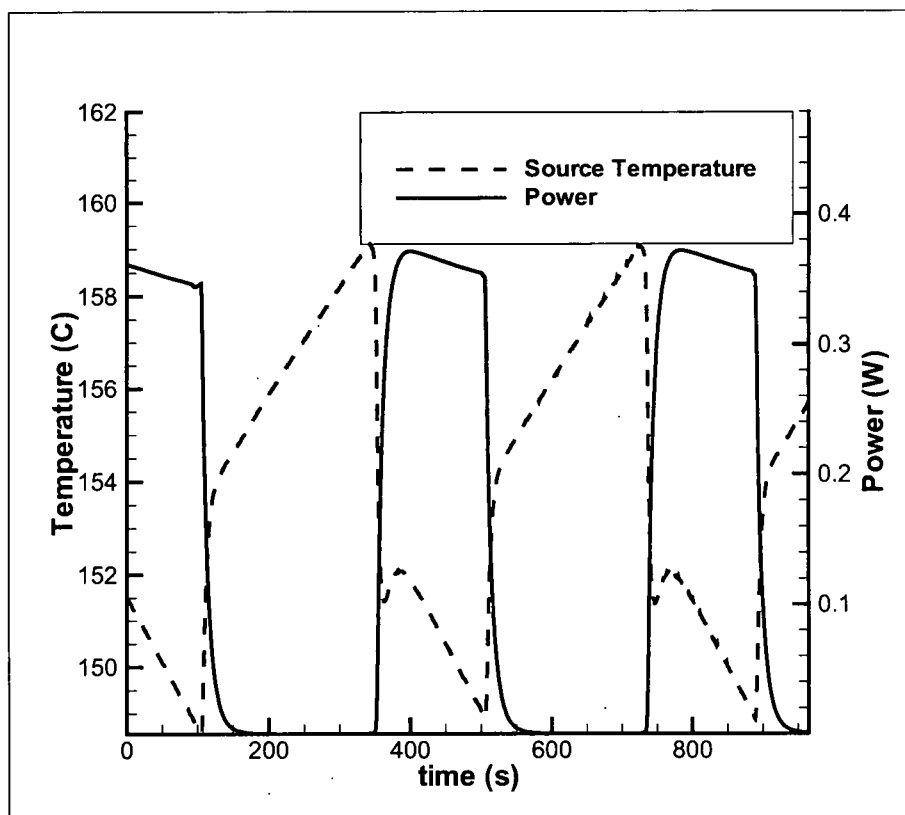


Figure B.9: Source temperature and TE output power with  $C_s = 300\text{J/K}$ , and  $\Delta T_s = 10^\circ\text{C}$ .

## **Appendix C**

### **Variable Air-Gap Experimental Results, Variable Heat Input**

The following plots are the result of the variable air-gap test for variable heat input. The source capacitances remained the same for all test and was 100 J/K. The frequency of the heat input varied from  $f = 0.000278$ ,  $0.000556$ , and  $0.00333$  Hz.

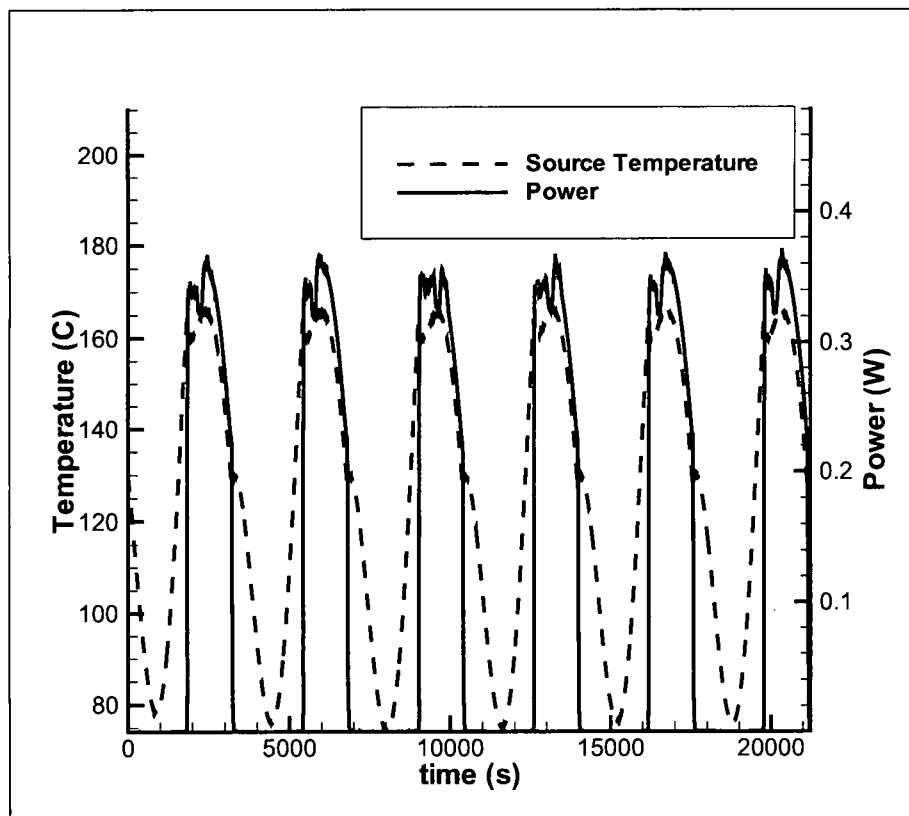


Figure C.1: Source temperature and TE output power with  $C_s = 100\text{J/K}$ ,  $\Delta T_s = 30^\circ\text{C}$ , and  $f = 0.000278\text{Hz}$ .

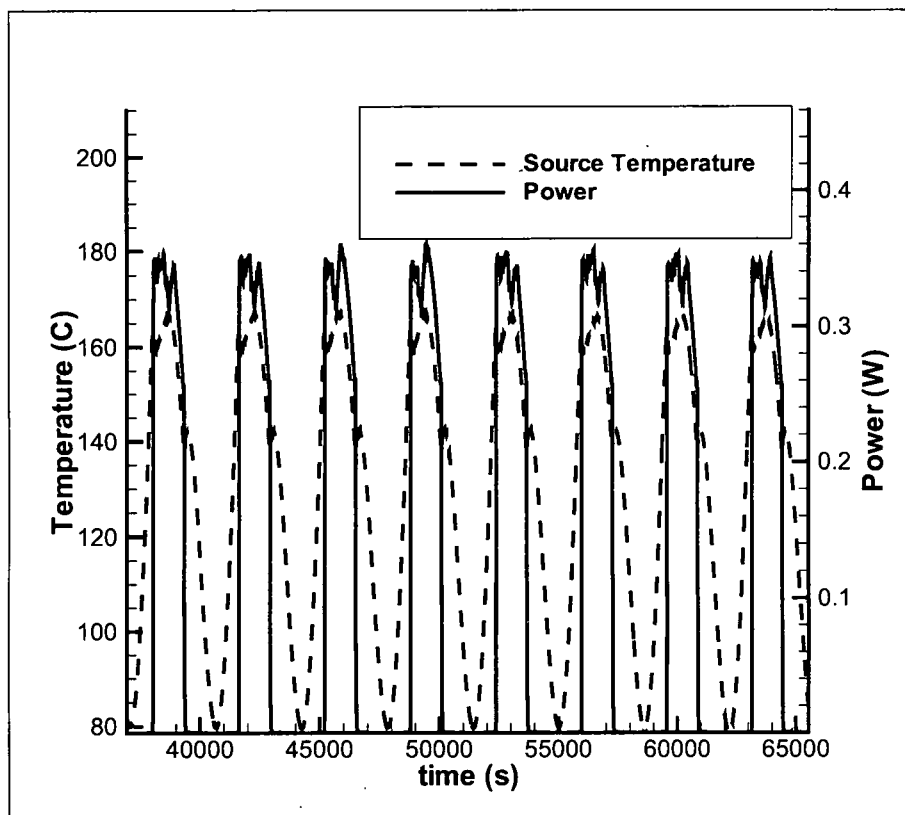


Figure C.2: Source temperature and TE output power with  $C_s = 100\text{J/K}$ ,  $\Delta T_s = 20^\circ\text{C}$ , and  $f = 0.000278\text{Hz}$ .

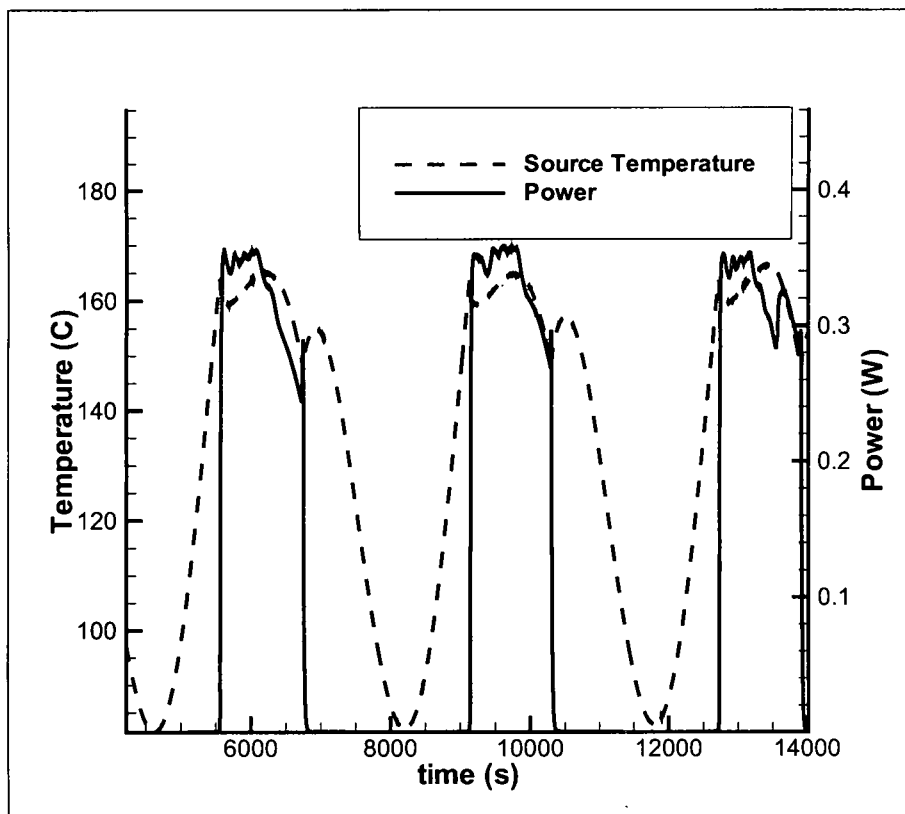


Figure C.3: Source temperature and TE output power with  $C_s = 100\text{J/K}$ ,  $\Delta T_s = 10^\circ\text{C}$ , and  $f = 0.000278\text{Hz}$ .

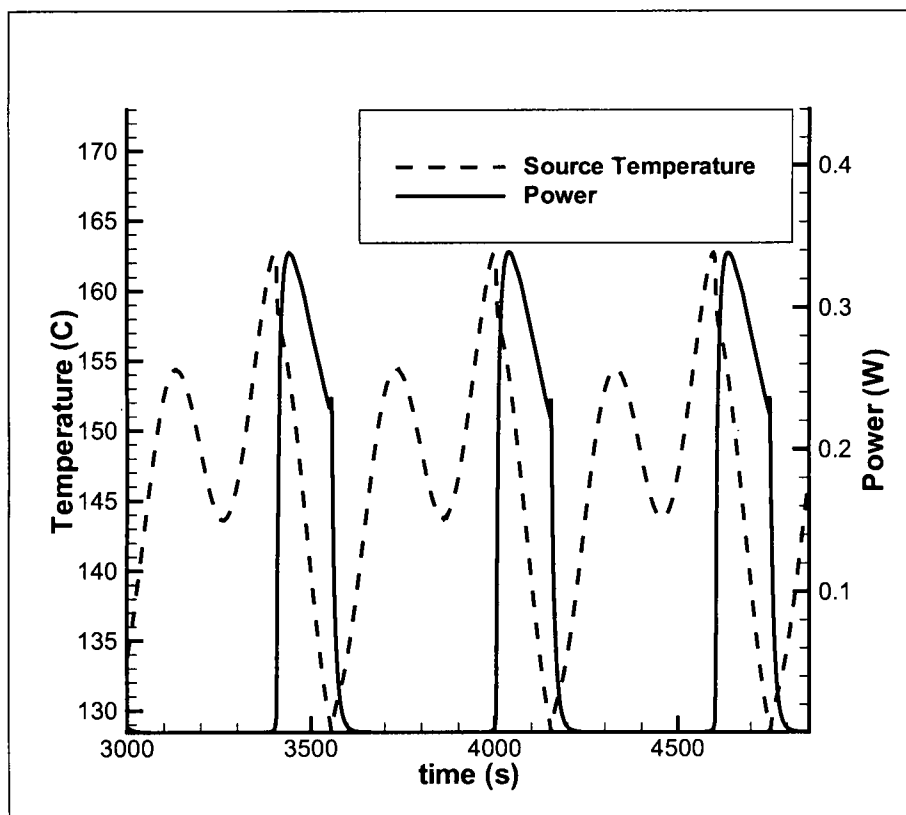


Figure C.4: Source temperature and TE output power with  $C_s = 100\text{J/K}$ ,  $\Delta T_s = 30^\circ\text{C}$ , and  $f = 0.00333\text{Hz}$ .



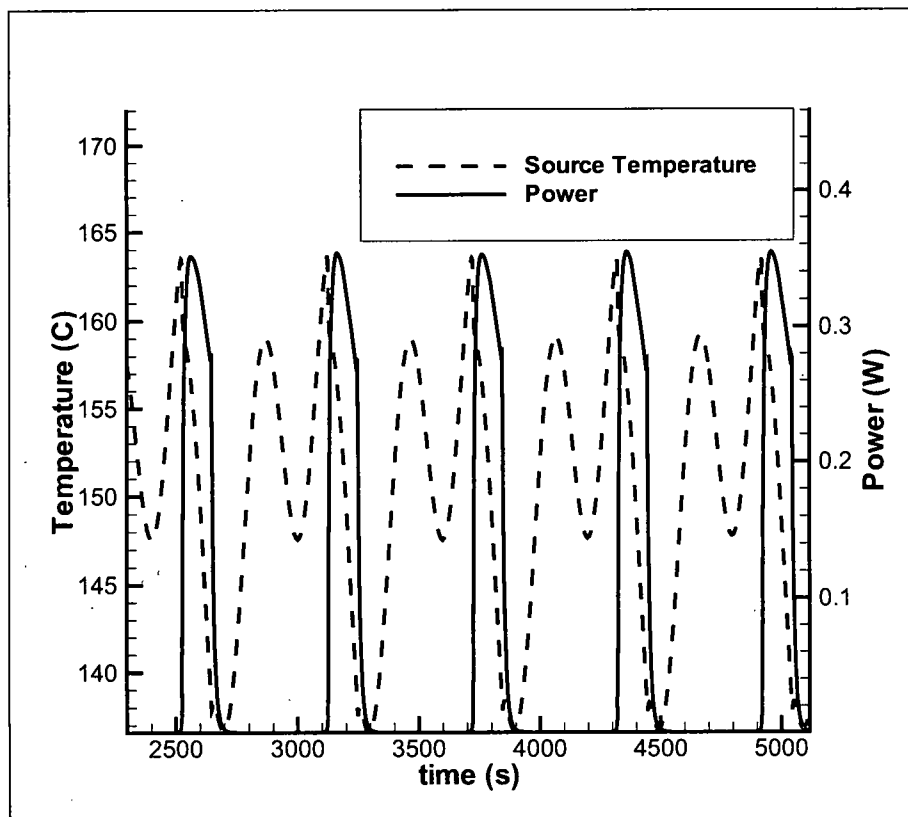


Figure C.5: Source temperature and TE output power with  $C_s = 100\text{J/K}$ ,  $\Delta T_s = 20^\circ\text{C}$ , and  $f = 0.00333\text{Hz}$ .

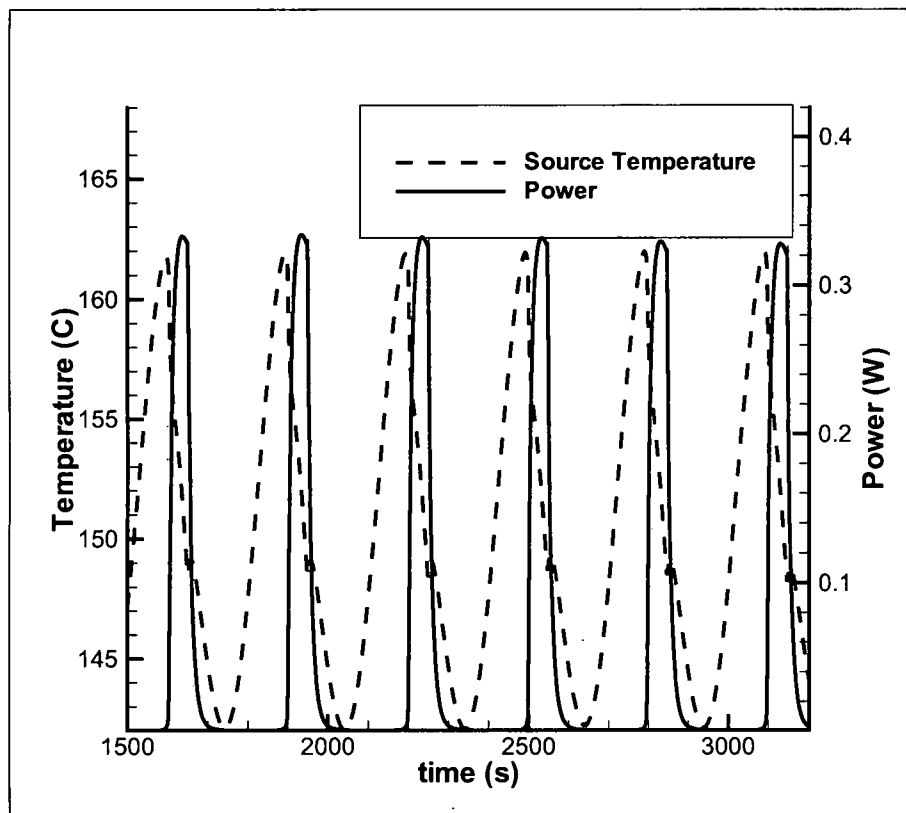


Figure C.6: Source temperature and TE output power with  $C_s = 100\text{J/K}$ ,  $\Delta T_s = 10^\circ\text{C}$ , and  $f = 0.00333\text{Hz}$ .

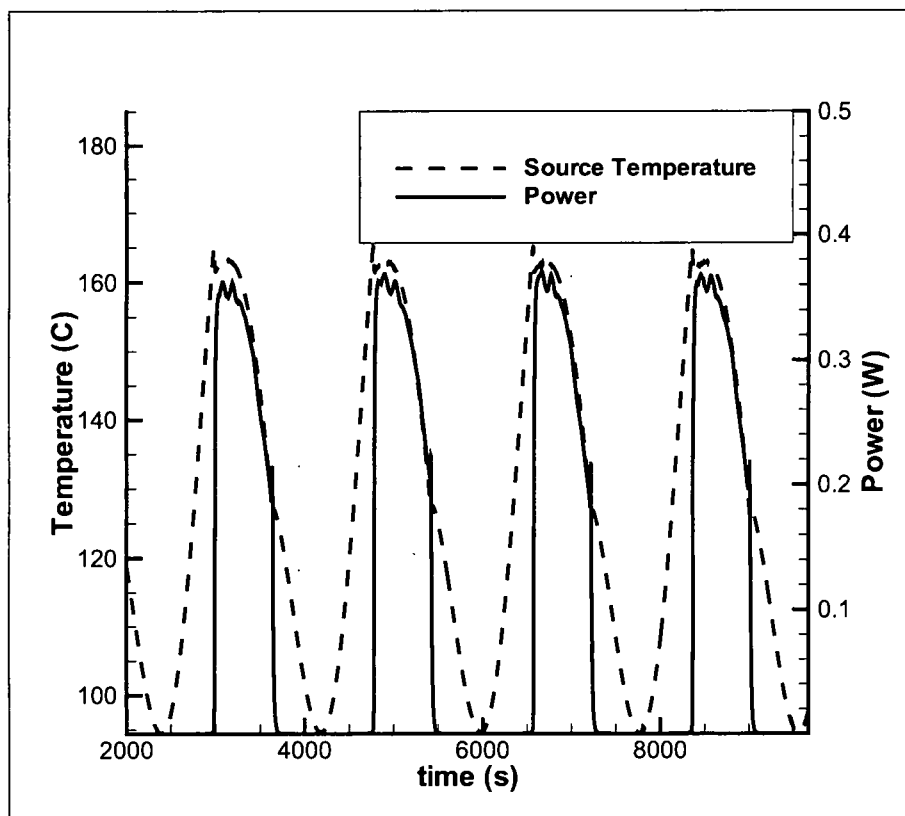


Figure C.7: Source temperature and TE output power with  $C_s = 100\text{J/K}$ ,  $\Delta T_s = 30^\circ\text{C}$ , and  $f = 0.000556\text{Hz}$ .

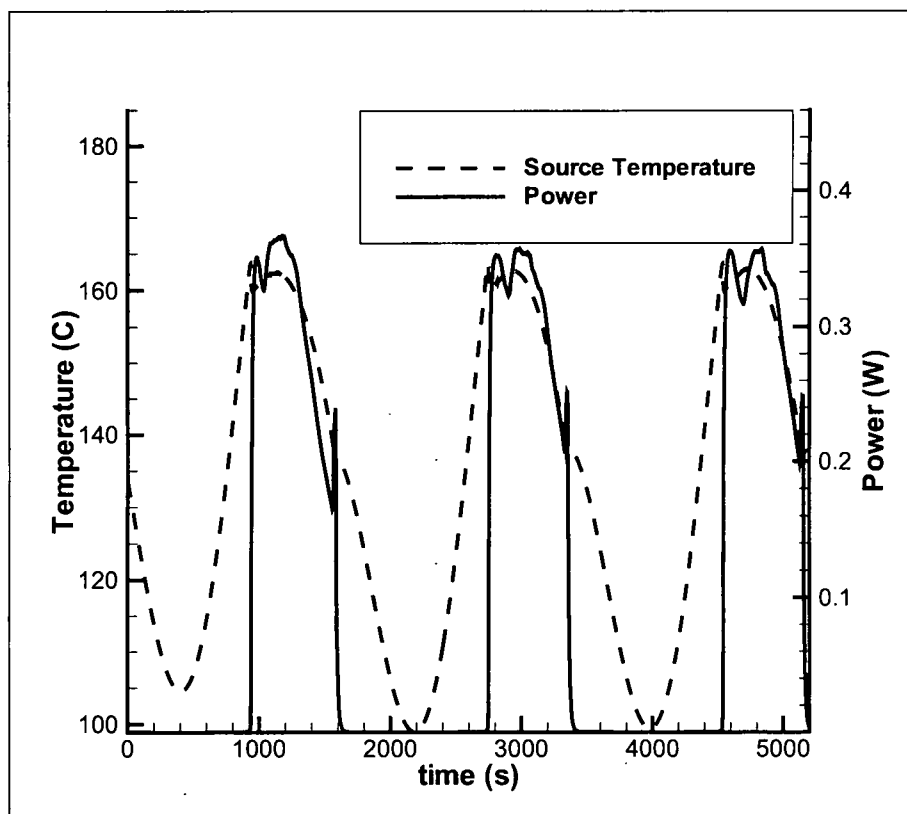


Figure C.8: Source temperature and TE output power with  $C_s = 100\text{J/K}$ ,  $\Delta T_s = 20^\circ\text{C}$ , and  $f = 0.000556\text{Hz}$ .

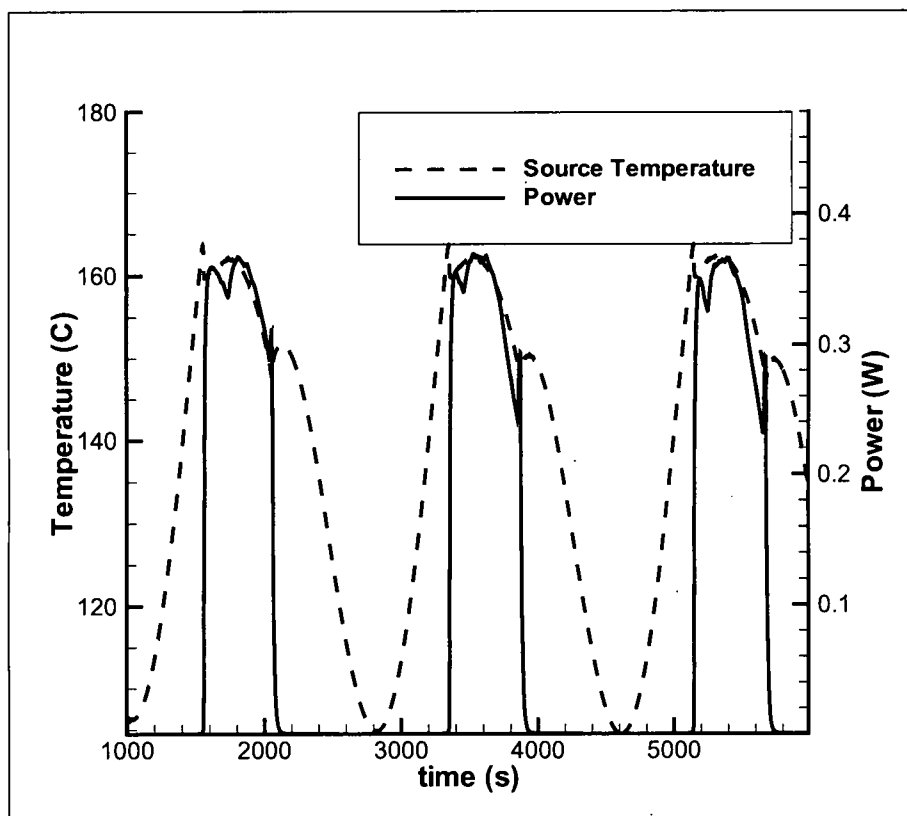


Figure C.9: Source temperature and TE output power with  $C_s = 100\text{J/K}$ ,  $\Delta T_s = 10^\circ\text{C}$ , and  $f = 0.000556\text{Hz}$ .

## Bibliography

- [1] Adler, J., "The Greening of America," <http://msnbc.msn.com/id/14206933/>, August 14 2006.
- [2] Birur, G. and O'Donnel, T., "Advanced Thermal Control Technologies for Space Science Missions at Jet Propulsion Laboratory," AIP Conference Proceedings, Vol. 552, February 2 2001, pp. 263–270.
- [3] Birur, G., Sur, T. W., Paris, A., Shakkottai, P., Green, A., and Haapanen, S., "Micro/nano Spacecraft Thermal Control Using a MEMS-Based Pumped Liquid Cooling System," Proceedings of SPIE, Microfluidics and BioMEMS, Vol. 4560, September 2001, pp. 196–206.
- [4] Janson, S. W., "Micro/Nanotechnology for the Satellite World," Proceedings of SPIE, MEMS Components and Applications for Industry, Automobiles, Aerospace, and Communication II, Vol. 4981, January 2003, pp. 95–106.
- [5] Novak, K., Phillips, C., Birur, G., Sunada, E., and Pauken, M., "Development of a Thermal Control Architecture for the Mars Exploration Rovers," AIP Conference Proceedings, Space Technology and Applications International Forum, edited by M. S. El-Genk, Vol. 654, 2003, pp. 194–205.
- [6] de Aragon, A. M., "Space Applications of Micro/Nano-Technologies," Journal of Micromechanics and Microengineering, Vol. 8, 1998, pp. 54–56.
- [7] Mahefkey, T., Yerks, K., and Donovan, B., "Thermal Management Challenges for Future Military Aircraft Power Systems," SAE Transactions, Journal of Aerospace, Vol. 113, No. 1, 2004, pp. 1965–1973.
- [8] Mudawar, I., "Assessment of High-Heat-Flux Thermal Management Schemes," IEEE Transactions on Components and Packaging Technologies, Vol. 24, No. 2, June 2001, pp. 122–141.
- [9] Sample, J., Rebello, K., Saffarian, H., and Osiander, R., "Carbon Nanotube Coatings for Thermal Control," The 9th Intersociety Conference on Thermal and Thermomechanical Phenomena in Electronic Systems, Vol. 1, June 1-4 2004, pp. 297–301.

- [10] Choi, J., Yamauchi, J., Morales, S., Horowitz, R., Zhao, Y., and Majumdar, A., "Design and Control of a Thermal Stabilizing System for a MEMS Optomechanical Un-cooled Infrared Imaging Camera," Sensor and Actuators A, Vol. 104, 2003, pp. 132–142.
- [11] Gilmore, D., Satellite Thermal Control Handbook, The Aerospace Corporation, El Segundo CA, 1994.
- [12] Amon, C. H., "MEMS-Based Thermal Management of High Heat Flux Devices EDIFICE: Embedded Droplet Impingement for Integrated Cooling of Electronics," Rohsenow Symposium on Future Trends in Heat Transfer, 2003, pp. 1–22.
- [13] Bogнар, G., Horvath, G., Kohari, Z., Pang, A., Desmulliez, M., Poppe, A., Rencz, M., and Szekely, V., "Thermal Characterization of a Radial Micro-Channel Cooling Plate," Semiconductor Thermal Measurement and Management Symposium, March 15-17 2005, pp. 135–140.
- [14] Edwards, T., "USAF Supercritical Hydrocarbon Fuels Interests," 31st Aerospace Sciences Meeting & Exhibit, AIAA 93-0807, Reno, NV, January 11-14 1993, pp. 1–11.
- [15] Cengel, Y. A. and Boles, M. A., Thermodynamics: An Engineering Approach, McGraw-Hill Higher Education, Boston, 6th ed., 2006.
- [16] Torres, E. and Rincon-Mora, G., "Harvesting Ambient Energy Will Make Embedded Devices Autonomous," Embedded.Com, August 2005, pp. 1–4.
- [17] Rowe, D., "Thermoelectrics, An Environmentally-Friendly Source of Electrical Power," Renewable Energy, Vol. 16, 1999, pp. 1251–1256.
- [18] Sales, B., "Smaller is Cooler," Science, Vol. 295, February 2002, pp. 1248–1249.
- [19] Eger, C. W., Kocoloski, M., McCarty, R., Kissock, J. K., and Hallinan, K. P., "Industrial Energy Harvesting: Potential, Mechanisms, and Examples," submitted to ACEEE Summer Study in Energy Efficiency in Industry, White Plains, New York, July 24-27 2007.
- [20] Kocoloski, M., A Review of Energy Harvesting Potential, Honors thesis project, University of Dayton, Dayton, Ohio, May 2006.
- [21] Rowe, D. and Min, G., "Evaluation of Thermoelectric Modules for Power Generation," Journal of Power Sources, Vol. 73, 1998, pp. 193–198.
- [22] Jovanovic, V., Ghamaty, S., and Bass, J., "Design and Fabrication of Quantum Well Thermoelectric Energy-Harvesting Power Supply for Navy Wireless Sensors," ASME Technical Conference on Packaging of MEMS, NEMS and Electric Systems, San Fransisco, CA, July 17-22 2005, pp. 1–6.
- [23] Jovanovic, V. and Ghamaty, S., "Design, Fabrication and Testing of Energy-Harvesting Thermoelectric Generator for Wireless Sensors," Presented at the SPIE Smart Structures and Material Conference.

- [24] Min, G. and Rowe, D. M., "Recent Concepts in Thermoelectric Power Generation," 21st International Conference on Thermoelectrics, IEEE, 2002, pp. 365–374.
- [25] Darrin, M., Osiander, R., Lehtonen, J., and Farrar, D., "Novel Micro Electro Mechanical Systems (MEMS) Packaging for the Skin of the Satellite," IEEE Aerospace Conference, Vol. 4, March 6-13 2004, pp. 2486–2494.
- [26] Sodano, H. A., Simmers, G. E., Dereux, R., and Inman, D. J., "Recharging Batteries using Energy Harvested from Thermal Gradients," Journal of Intelligent Material Systems and Structures, Vol. 18, January 2007, pp. 1–10.
- [27] Wesley M. Rohrer, J., Energy Management Handbook, chap. Chapter 8, Waste-Heat Recovery, The Fairmont Press Inc., Lilburn, GA, 2001, pp. 187–213.
- [28] Riffat, S. B. and Ma, X., "Thermoelectrics: A Review of Present and Potential Applications," Applied Thermal Engineering, Vol. 23, 2003, pp. 913–935.
- [29] Hallinan, K. P., Sanders, B., Somphone, T., and Ephrem, G., "Entropy Generation Metric for Evaluating and Forecasting Aircraft Energy Management Systems," International Journal of Exergy, Vol. 2, No. 2, 2005, pp. 120–145.
- [30] Fleurial, J.-P. and et al., "New Materials and Devices for Thermoelectric Applications," Proceedings of 32nd Intersociety Energy Conversion Energy Conference, Honolulu, Hawaii, August 1 1997, pp. 1080–1086.
- [31] Goldsmid, H. J., CRC Handbook of Thermoelectrics, chap. Conversion Efficiency and Figure-of-Merit, CRC Press, Inc., Boca Raton, 1995, pp. 19–25.
- [32] Rowe, D., Thermoelectrics Handbook Macro to Nano, CRC Taylor & Francis, Boca Raton, 2006.
- [33] Nolas, G., Sharp, J., and Goldsmid, H., Thermoelectrics Basic Principles and New Materials Development, Springer, New York, 2001.
- [34] Chen, M., Lu, S.-S., and Liao, B., "On the Figure of Merit of Thermoelectric Generators," Journal of Energy Resources Technology, Vol. 127, March 2005, pp. 37–41.
- [35] Chen, G., Nanoscale Energy Transport and Conversion, Oxford University Press, New York, 2005.
- [36] Zhang, Y., Zeng, G., Singh, R., Christofferson, J., Croke, E., Bowers, J. E., and Shakouri, A., "Measurement of Seebeck Coefficient Perpendicular to SiGe Superlattice," 21st International Conference on Thermoelectrics, IEEE, August 25-29 2002, pp. 329–332.
- [37] Taylor, P. J., Jesser, W. A., Rosi, F. D., and Derzko, Z., "A Model for the Non-steady-state Temperature Behavior of Thermoelectric Cooling Semiconductor Devices," Semicond. Sci. Technol., Vol. 12, 1997, pp. 443–447.



- [38] ElGenk, M., Seo, J., and Buksa, J., "Load Following Characteristics of Si Ge GaP Thermoelectric Generators and their Response to External Heating," Journal of Applied Physics, Vol. 61, No. 5, March 1987.
- [39] Hoyos, G. E. and K. R. Rao, a. D. J., "Fast Transient Response of Novel Peltier Junctions," Energy Conversion, Vol. 17, 1977, pp. 45–54.
- [40] Stilbans, L. and Fedorovich, N., "The Operation of Refrigeration Thermoelectric Elements in Nonstationary Conditions," Sov. Phys. Tech. Phys., Vol. 3, 1958, pp. 460–463.
- [41] Landecker, K. and Findlay, A. W., "Study of the Fast Transient Behavior of Peltier Junctions," Solid-State Electronics, Vol. 3, 1961, pp. 239–260.
- [42] Idnurm, M. and Landecker, K., "Experiments with Peltier Junctions Pulsed with High Transient Currents," Journal of Applied Physics, Vol. 34, No. 6, 2004, pp. 1806–1810.
- [43] Gray, P. E., "Approximate Dynamic Response Calculations for Thermoelectric Peltier-Effect Devices," Solid-State Electronics, Vol. 6, 1963, pp. 339–348.
- [44] Idnurm, M. and Landecker, K., "Experiments with Peltier Junctions with High Transient Currents," Journal of Applied Physics, Vol. 34, No. 6, June 1963, pp. 1806–1810.
- [45] Miner, A. and Majumdar, A., "Thermo-electro-mechanical Refrigeration Based on Transient Thermoelectric Effects," 18th International Conference on Thermoelectrics, August 25-29 1999, pp. 27–30.
- [46] Snyder, G., "Application of the Compatibility Factor to the Design of Segmented and Cascaded Thermoelectric Generators," Applied Physics Letter, Vol. 84, No. 13, 2004, pp. 2436–2438.
- [47] Snyder, G. J. and Ursell, T. S., "Thermoelectric Efficiency and Compatibility," Physcial Review Letters, Vol. 91, No. 14, October 2003, pp. 1–4.
- [48] Yang, J., Aizawa, T., Yamamoto, A., and Ohta, T., "Effects of Interface Layer on Thermoelectric Properties of a pn Junction Prepared Via the BMA-HP Method," Materials Science and Engineering B, Vol. 85, 2001, pp. 34–37.
- [49] Fleurial, J.-P., Borshchevsky, A., Caillat, T., and Ewell, R., "New Material and Devices for Thermoelectric Applications," Energy Conversion Engineering Conference, IEEE, Honolulu, HI, July 27 - August 1 1997, pp. 1080–1085.
- [50] Zou, H., Rowe, D. M., and Min, G., "Preparation and Characterization of p-type Sb<sub>2</sub>Te<sub>3</sub> and n-type Bi<sub>2</sub>Te<sub>3</sub> Thin Films Grown by Coevaporization," J. Vac. Sci. Technol. A, Vol. 19, No. 3, May-June 2001, pp. 899–903.
- [51] Inc., H.-Z. T., "HZ-20 Thermoelectric Module," <http://www.hi-z.com/websit04.htm>, February 2007.

- [52] Krommenhoek, D., Ghamaty, S., Bass, J., Elsner, N., and Jovanovic, V., "Predicted Performance of Quantum Well Thermoelectrics for Waste Heat Recovery Power Generation," .
- [53] Mayer, P. and Ram, R. J., "Thin-film Thermoelectric Generator Element Characterization," IEEE International Conference on Thermoelectrics, June 19-23 2005, pp. 265-268.
- [54] Bottner, H., Nurnus, J., and Gavrikov, A., "New Thermoelectric Components Using Microsystem Technologies," Journal of Microelectricalmechanical Systems, Vol. 13, No. 3, June 2004, pp. 414-420.
- [55] Bottner, H., "Micropelt Miniaturized Thermoelectric Devices: Small Size, High Cooling Power Densities, Short Response Time," 24th International Conference on Thermoelectrics, IEEE, June 19-23 2005, pp. 1-8.
- [56] Bottner, H., "Thermoelectric Micro Devices: Current State, Recent Developments and Future Aspects for Technological Progress and Application," 21st International Conference on Thermoelectrics, IEEE, August 25-29 2002, pp. 511-518.
- [57] Hillhouse, H. and Tuominen, M., "Modeling the Thermoelectric Transport Properties of Nanowires Embedded in Oriented Microporous and Mesoporous Films," Microporous and Mesoporous Materials, Vol. 47, 2001, pp. 39-50.
- [58] Akbari, P., Chui, B.-K., Oravecz-Simpkins, L., and Lloyd, J., "A Discussion of Nano-Length Scale Heat Conduction by Comparing the Ballistic-Diffusive Equation and Molecular Dynamics Simulation," ASME International Mechanical Engineering Congress and Exposition, New Orleans, Louisiana, November 17-22 2002, pp. 1-3.
- [59] Chen, G., "Ballistic-Diffusive Equations for Transient Heat Conduction from Nano to Macroscales," Transactions of the ASME, Vol. 124, 2002, pp. 320-328.
- [60] Lyeo, H.-K., Shi, L., and Shih, C., "Thermoelectric Mapping of p-n Junctions and Superlattices," 21st International Conference on Thermoelectrics, August 25-29 2002, pp. 349-352.
- [61] Ghamaty, S. and Elsner, N., "Quantum Well Thermoelectric Devices," ASME Technical Conference on Packaging of MEMS, NEMS and Electric Systems, San Francisco, CA, July 17-22 2005, pp. 1-6.
- [62] Wautelet, M., "Scaling Laws in the Macro-, Micro- and Nanoworlds," European Journal of Physics, Vol. 22, 2001, pp. 601-611.
- [63] Dresselhaus, M. S., Lin, Y. M., Black, M. R., Rabin, O., and Dresselhaus, G., "New Directions for Low Dimensional Thermoelectricity," Materials Research Society Symposium Proceedings, Vol. 793, 2003, pp. 419-430.
- [64] Venkatasubramanian, R., "Thin-film Superlattice Thermoelectric Devices for Power Conversion and Cooling," [http://www.its.org/ict2002/Abstracts/Rama\\_Venkatasubramanian.htm](http://www.its.org/ict2002/Abstracts/Rama_Venkatasubramanian.htm), 2003.

- [65] Venkatasubramanian, R., Viivola, E., Calpitts, T., and O'Quinn, B., "Thin Film Thermoelectric Devices with High Room Temperature Figure of Merit," Nature, Vol. 413, No. 6856, October 2001, pp. 597-602.
- [66] Martin, P. M. and Olsen, L. C., "Recent Progress in Scale Up of Multilayer Thermoelectric Films," DOE/EPRI High Efficiency Thermoelectric Workshop, San Diego, CA, 17-20 February 2004.
- [67] Bell, L., "Thermoelectric Technology Readiness for Large Scale Commercialization," DOE/EPRI High Efficiency Thermoelectric Workshop, San Diego, CA, 17-20 February 2004.
- [68] Fairbanks, J., "Chair's Overview of High Efficiency Thermoelectrics and Potential," DOE/EPRI High Efficiency Thermoelectric Workshop, San Diego, CA, 17-20 February 2004.
- [69] Elder, A., Bertram, M., and Liebl, J., "Visions of Possible Thermoelectrics for Vehicle Applications," DOE/EPRI High Efficiency Thermoelectric Workshop, San Diego, CA, 17-20 February 2004.
- [70] Chua, H. T., NG, K. C., Xuan, X. C., Yap, C., and Gordon, J., "Temperature-Entropy Formulation of Thermoelectric Thermodynamic Cycles," Physical Review E, Vol. 65, No. 056111, 2002, pp. 1-6.
- [71] Hilbert, C., Nelson, R., Reed, J., Lunceford, B., Somadder, A., and Hu, K., "Thermoelectric MEMS Coolers," 18th International Conference on Thermoelectrics, Baltimore, MD, August 29 - September 2 1999, pp. 117-122.
- [72] Chang, H.-M. and Kim, H.-J., "Development of a Thermal Switch for Faster Cool-Down by Two-Stage Cryocooler," Cryogenics, Vol. 40, 2000, pp. 769-777.
- [73] Nast, T., Bell, G., and Barnes, C., "Development of Gas Gap Cryogenic Thermal Switch," Proceedings of the Cryogenic Engineering Conference, Vol. 27, San Diego, CA, August 11-14 1981, pp. 1117-1124.
- [74] Marland, B., Bugby, D., and Stouffer, C., "Development and Testing of Advanced Cryogenic Thermal Switch Concepts," Space Technology and Applications International Forum, edited by M. S. El-Genk, Vol. 504, Albuquerque, NM, January 2000, pp. 837-846.
- [75] Yamamoto, J., "Precooling of a Superconducting Magnet Using a Cryocooler and Thermal Switches," The Review of Scientific Instruments, Vol. 50, No. 11, November 1979, pp. 1382-1385.
- [76] Bluzer, N. and Bahl, S., "A Mechanical Thermal Switch fir Using a Cryostat Between 4 and 650 K," The Review of Scientific Instruments, Vol. 43, No. 12, December 1972, pp. 1841-1842.

- [77] Paulsen, B., Batty, J., and Agren, J., "Cryogenic Thermal Diodes," AIP Conference Proceedings, Space Technology and Applications International Forum, Vol. 504, January 19 2000, pp. 785–790.
- [78] Slater, T., VanGerwen, P., Masure, E., Preud'homme, F., and Baert, K., "Thermo-Mechanical Characteristics of a Thermal Switch," Sensors and Actuators A, Vol. 53, No. 1, May 1996, pp. 341–344.
- [79] Yao, D.-J., Kim, C.-J., and Chen, G., "MEMS Thermoelectric Microcooler," International Conference on Thermoelectrics, Beijing, China, June 8-11 2001, pp. 401–424.
- [80] Snyder, G. J., Lim, J., Huang, C.-K., and Fleurial, J.-P., "Thermoelectric Microdevice Fabricated by a MEMS-like Electrochemical Process," Nature Materials, Vol. 2, August 2003, pp. 528–531.
- [81] Ghoshal, U. S., "Thermoelectric Cooling with Plural Dynamic Switching to Isolate Heat Transport Mechanisms," U.S. Patent 5,867,990, February 9 1999.
- [82] Ghoshal, U. S., "Thermoelectric Cooling with Dynamic Switching to Isolate Heat Transport Mechanisms," U.S. Patent 5,966,941, October 19 1999.
- [83] Swanson, T. D. and Chen, P. T., MEMS and Microstructures in Aerospace Applications, chap. Microsystems in Spacecraft Thermal Control, CRC Taylor and Francis, Boca Raton, 2006, pp. 183–202.
- [84] Osiander, R., Firebaugh, S., Champion, J., Farrar, D., and Darrin, M. G., "Microelectromechanical Devices for Satellite Thermal Control," IEEE Sensors Journal, Vol. 4, No. 4, August 2004, pp. 525–531.
- [85] Beasley, M., Firebaugh, S., Edwards, R., Keeney, A., and Osiander, R., "MEMS Thermal Switch for Spacecraft Thermal Control," Proceedings of SPIE, edited by S. W. Janson, Vol. 5344, 2004, pp. 98–105.
- [86] Beasley, M., Firebaugh, S., Edwards, R., Keeney, A., and Osiander, R., "Microfabricated Thermal Switches for Emittance Control," AIP Conference Proceedings, Space Technology and Applications International Forum, Vol. 699, February 4 2004, pp. 119–125.
- [87] Christensen, A. O., Jacob, J. P., Richards, C. D., Bahr, D. F., and Richards, R. F., "Fabrication and Characterization of a Liquid-Metal Micro-Droplet Array for use as a Thermal Switch," Proceedings of ASME Summer Heat Transfer Conference, Las Vegas, NV, July 21-23 2003, pp. 97–100.
- [88] Sunada, E., Lankford, K., Pauken, M., Novak, K., and Birur, G., "Wax-Actuated Heat Switch for Mars Surface Application," AIP Conference Proceedings, Space Technology and Applications International Forum, edited by M. S. El-Genk, Vol. 608, 2002, pp. 211–213.

- [89] Cho, J. H., Richards, C. D., Jiao, J., Bahr, D. F., and Richards, R. F., "Design and Characterization of a MEMS Thermal Switch," Solid-State Sensors, Actuators, and Microsystems Workshop, Hilton Head Islands, South Carolina, June 4-8 2006, pp. 272-275.
- [90] Riordan, H. E., "Device for Controlling Temperature by Heat Conduction," U.S. Patent 3,225,820, December 1965.
- [91] Kopf, L., "A Low Temperature Heat Pipe Used as a Thermal Switch," The Review of Scientific Instruments, Vol. 42, No. 12, December 1971, pp. 1764-1765.
- [92] Peterson, G., An Introduction to Heat Pipes, John Wiley & Sons, Inc., New York, 1994.
- [93] Take, K. and Webb, R., "Thermal Performance of Integrated Plate Heat Pipe with a Heat Spreader," Journal of Electronic Packaging, Vol. 123, 2001, pp. 189-195.
- [94] Cao, Y. and Gao, M., "Experiments and Analyses of Flat Miniature Heat Pipes," Journal of Thermophysics and Heat Transfer, Vol. 11, No. 2, April-June 1997, pp. 158-164.
- [95] Faghri, A., Heat Pipe Science and Technology, Taylor and Francis, Washington D.C., 1995.
- [96] Kim, I. Y. and Peter Wayner, J., "Shape of and Evaporating Completely Wetting Extended Meniscus," Journal of Thermophysics and Heat Transfer, Vol. 10, No. 2, April-June 1996, pp. 320-325.
- [97] Swanson, L. W. and Peterson, G. P., "The Interfacial Thermodynamics of Micro Heat Pipes," Journal of Heat Transfer, Vol. 117, February 1995, pp. 195-201.
- [98] Berre, M. L., Launay, S., Sartre, V., and Lallemand, M., "Fabrication and Experimental Investigation of Silicon Micro Heat Pipes for Cooling Electronics," Journal of Micromechanics and Microengineering, Vol. 13, 2003, pp. 436-441.
- [99] Cytryowicz, D., Hamdan, M., Medis, P., Shuja, A., and Henderson, H. T., "MEMS Loop Heat Pipe Based on Coherent Porous Silicon Technology," Space Technology and Applications International Forum, 2002, pp. 1-13.
- [100] Wu, D. and Peterson, G. P., "Investigation of the Transient Characteristics of a Micro Heat Pipe," Journal of Thermophysics, Vol. 5, No. 2, April-June 1991, pp. 129-134.
- [101] Mallik, A. K., Peterson, G. P., and Weichold, M. H., "On the Use of Micro Heat Pipes as an Integral Part of Semiconductor Devices," Journal of Electronic Packaging, Vol. 114, No. 4, December 1992, pp. 436-442.
- [102] Mallik, A. K., Peterson, G. P., and Weichold, M. H., "Fabrication of Vapor-Deposited Micro Heat Pipes Arrays as an Integral Part of Semiconductor Devices," Journal of Microelectromechanical Systems, Vol. 4, No. 3, September 1995, pp. 119-131.

- [103] Tzanova, S., Ivanova, M., Avenas, Y., and Schaeffer, C., "Analytical Investigation of Flat Silicon Micro Heat Spreader," 39th IAS Annual Meeting, Industry Applications Conference, October 3-7 2004, pp. 2296-2302.
- [104] Xuan, X. C., "Optimum Design of a Thermoelectric Device," Semicond. Sci. Technol., Vol. 17, 2002, pp. 114-119.
- [105] Yamanashi, M., "A New Approach to Optimum Design in the Thermoelectric Cooling Systems," Journal of Applied Physics, Vol. 80, No. 9, November 1996, pp. 5494-5502.
- [106] Stevens, J., "Optimized Thermal Design of Small  $\Delta T$  Thermoelectric Generators," Society of Automotive Engineers, Vol. 2564, 1999, pp. 1-6.
- [107] Esarte, J., Min, G., and Rowe, D. M., "Modeling Heat Exchangers for Thermoelectric Generators," Journal of Power Science, Vol. 93, 2001, pp. 72-76.
- [108] Marz, M. and Nance, P., "Thermal Modeling of Power-Electronic System," <http://www.infineon.com/products/36/36.htm>, 2004.
- [109] Wang, T.-Y. and Chung-Ping Chen, C., "SPICE-Compatible Thermal Simulation with Lumped Circuit Modeling for Thermal Reliability Analysis based on Modeling Order Reduction," 5th International Symposium of Quality Electronics Design, San Jose, CA, March 22-24 2004, pp. 357-362.
- [110] Kokkas, A. G., "Thermal Analysis of Multiple-Layer Structures," IEEE Transactions on Electron Devices, Vol. 21, No. 11, 1974, pp. 674-681.
- [111] Szekely, V., "Identification of RC Networks by Deconvolution: Chances and Limits," IEEE Transactions on Circuits and Systems-I: Fundamental Theory and Application, Vol. 45, No. 3, March 1998, pp. 244-258.
- [112] Yun, C.-S., Malberti, P., Ciappà, M., and Fichtner, W., "Thermal Component Model for Electrothermal Analysis of IGBT Module System," IEEE Transactions on Advanced Packaging, Vol. 24, No. 3, August 2001, pp. 401-406.
- [113] Lineykin, S. and Ben-Yaakov, S., "Modeling and Analysis of Thermoelectric Modules," Applied Power Electronics Conference and Exposition, 2005, pp. 2019-2023.
- [114] Bagnoli, P. E., Casarosa, C., Ciampi, M., and Dallago, E., "Thermal Resistance Analysis by Induced Transient (TRAIT) Method for Power Electronic Devices Thermal Characterization - Part I: Fundamentals and Theory," IEEE Transactions on Power Electronics, Vol. 13, November 1998.
- [115] Bagnoli, P. E., Casarosa, C., Dallago, E., and Nardoni, M., "Thermal Resistance Analysis by Induced Transient (TRAIT) Method for Power Electronic Devices Thermal Characterization - Part II: Practice and Experiments," IEEE Transactions on Power Electronics, Vol. 13, November 1998, pp. 1220-1228.
- [116] Ozisik, M. N., Heat Conduction, John Wiley and Sons, Inc., New York, 2nd ed., 1993.

- [117] Szekely, V., "A New Evaluation Method of Thermal Transient Measurement," Microelectronics Journal, Vol. 28, 1997, pp. 277–292.
- [118] Chen, J. and Wu, C., "Analysis on the Performance of a Thermoelectric Generator," Journal of Energy Resource Technology, Vol. 122, 2000, pp. 61–63.
- [119] Hodes, M., "On One-Dimensional Analysis of Thermoelectric Modules (TEMs)," IEEE Transactions on Components and Packaging Technologies, Vol. 28, June 2005, pp. 218–229.
- [120] Mitrani, D., Tome, J. A., and Salazar, J., "Methodology for Extracting Thermoelectric Module Parameters," IEEE Transactions on Instrumentation and Measurement, Vol. 54, August 2005, pp. 1548–1552.
- [121] Nilsson, J. W. and Riedel, S. A., Electric Circuits, Addison-Wesley Publishing Company, Reading, Massachusetts, fifth edition ed., 1996.
- [122] McCarty, R., Hallinan, K. P., Sanders, B., and Somphone, T., "Enhancing Thermoelectric Energy Recovery via Modulations of Source Temperature for Cyclical Heat Loadings," Proceedings of ASME InterPack, San Francisco, California, July 17-22 2005, pp. 1–14.
- [123] McCarty, R., Hallinan, K. P., Sanders, B., and Somphone, T., "Enhancing Thermoelectric Energy Recovery via Modulations of Source Temperature for Cyclical Heat Loadings," to appear in Journal of Heat Transfer, June 2007.
- [124] Lampinen, M., "Thermodynamic Analysis of Thermoelectric Generator," Journal of Applied Physics, Vol. 69, No. 8, April 1991, pp. 4318–4323.
- [125] MathWorks, I., Learning Simulink 6, The MathWorks, Inc., 2004.
- [126] Somphone, T. and Hallinan, K. P., "The Experimental Work for the Thermal Energy Transport and Harvesting System," Tech. rep., WPAFB/AFRL/VASA, 2004.
- [127] McCarty, R., Monaghan, D., Hallinan, K. P., and Sanders, B., "Experimental Verification of Source Temperature Modulation via a Thermal Switch in Thermoelectric Energy Harvesting," submitted to Journal of Thermophysics and Heat Transfer, 2006.
- [128] Kovacs, G. T., Micromachined Transducers Sourcebook, McGraw-Hill, 1998.
- [129] MEMSCAP.com, "PolyMumps," <http://memsrus.com/nc-mumps.poly.html>, 2005.
- [130] Chen, W.-H. and et al., "Analysis of Tip Deflection and Force of a Bimetallic Cantilever Microactuator," Journal of Micromechanics and Microengineering, Vol. 3, 1993, pp. 4–7.
- [131] Incropera, F. P., Fundamentals of Heat and Mass Transfer, John Wiley and Sons, New York, 4th ed., 1996.

- [132] Vargaftik, N. B., Vinogradov, Y. K., and Yargin, V. S., Handbook of Physical Properties of Liquids and Gases: Pure Substances and Mixtures, Begell House, New York, 3rd ed., 1996.
- [133] Carey, V. P., Liquid-Vapor Phase-Change Phenomena, Taylor and Francis, New York, 1992.
- [134] Ma, H. B. and Peterson, G. P., "The Minimum Meniscus Radius and Capillary Heat Transport Limit in Micro Heat Pipes," Journal of Heat Transfer, Vol. 120, February 1998, pp. 227–233.
- [135] MicroChem, "NANO SU-8 2000," [www.microchem.com](http://www.microchem.com), 2006.
- [136] Spiegel, M. R., Schiller, J., and Srinivasan, R. A., Theory and Problems of Probability and Statistics, McGraw-Hill, New York, 2nd ed., 2000.
- [137] Kays, W. M. and Crawford, M. E., Convective Heat and Mass Transfer, McGraw-Hill, Inc., New York, 3rd ed., 1993.
- [138] Tsai, J.-H. and Lin, L., "Transient Thermal Bubble Formation on Polysilicon Micro-Resistors," Journal of Heat Transfer, Vol. 124, April 2002, pp. 375–382.
- [139] Vargaftik, N. B., Tables on the Thermophysical Properties of Liquids and Gases, Hemisphere Publishing Corp., Washington, 2nd ed., 1975.



R702033887